



SAPIENZA
UNIVERSITÀ DI ROMA

Dipartimento di Meccanica e Aeronautica

Theoretical and Applied Mechanics

Ph.D. thesis

**Modelling of particle wall-deposition in two
phase gas-solid flows**

Candidate: Paolo Venturini

Supervisor:
Prof. Kemal Hanjalić

Tutor:
Prof. Carlo Massimo Casciola

Contents

| | | |
|----------|---|-----------|
| 1 | TWO-PHASE FLOWS AND DEPOSIT FORMATION: THE PROBLEM ACTUALITY AND NEEDS FOR MODELLING | 1 |
| 1.1 | INTRODUCTION | 1 |
| 1.2 | DEPOSIT FORMATION WITHIN A SOLID FUEL-FED BOILER..... | 2 |
| 1.3 | MECHANISMS OF PARTICLE DEPOSITION | 2 |
| 1.3.1. | <i>Inertial impact</i> | 3 |
| 1.3.2. | <i>Thermophoresis</i> | 4 |
| 1.4 | SIZE DISTRIBUTION OF PARTICLES IN BIOMASS-FED BOILERS..... | 4 |
| 1.5 | TWO-PHASE FLOWS CLASSIFICATION AND MODELLING | 5 |
| 1.6 | PARTICLE EQUATION OF MOTION..... | 7 |
| 1.7 | TURBULENT DISPERSION OF PARTICLES: DIFFERENT APPROACHES TO MODELLING | 8 |
| 1.7.1 | <i>The Stochastic Separated Flow (SSF) approach</i> | 9 |
| 1.7.2 | <i>The Particle Cloud Tracking (PCT) approach</i> | 9 |
| 1.7.3 | <i>The Single Particle Tracking (SPT) approach</i> | 10 |
| 1.7.4 | <i>Particle Number Density (PND) approach</i> | 10 |
| 1.8 | TURBULENT DISPERSION OF PARTICLES: THE PCT MODEL | 10 |
| 2 | PARTICLE TRACKING AND DISPERSION ALGORITHMS | 18 |
| 2.1 | OUTLINE OF THE CODE FOR DEPOSIT PREDICTION..... | 30 |
| 2.2 | ALGORITHM FOR PARTICLE TRACKING | 16 |
| 2.3 | ALGORITHM FOR CLOUD SEARCH | 20 |
| 2.4 | EVALUATION OF THE PARTICLE LOCAL VELOCITY IN THE PCT MODEL | 22 |
| 3 | PRELIMINARY TEST OF CONVENTIONAL APPROACHES TO AN INDUSTRIAL FLOW | 24 |
| 3.1 | DEPOSIT IN A BIOMASS-FED BOILER..... | 24 |
| 3.4.1 | <i>Results</i> | 28 |
| 4 | PARTICLE IMPACT AND ADHESION | 42 |
| 4.1 | NORMAL IMPACT | 42 |
| 4.1.1 | <i>Elastic impact</i> | 37 |
| 4.1.2 | <i>Elastic-plastic impact</i> | 38 |
| 4.1.3 | <i>Adhesion energy</i> | 39 |
| 4.2 | COEFFICIENT OF RESTITUTION (COR) AND ADHESION | 42 |
| 4.2.1 | <i>Van Beek model</i> | 43 |
| 4.2.2 | <i>Thornton and Ning model</i> | 46 |
| 4.2.3 | <i>Feng et al. model</i> | 48 |
| 4.2.4 | <i>Comparison of models</i> | 49 |

| | | |
|-----------|---|------------|
| 4.3 | OBLIQUE IMPACT..... | 51 |
| 4.3.1 | <i>Effect of the impact angle</i> | 52 |
| 4.3.2 | <i>Konstandopoulos's model</i> | 56 |
| 4.4 | ALGORITHM FOR ADHESION/REBOUND OF PARTICLES | 58 |
| 4.5 | TEMPERATURE EFFECT ON ASH STICKING PROPENSITY | 59 |
| 5 | PARTICLE RE-SUSPENSION MODELLING | 79 |
| 5.1 | PARTICLE RE-SUSPENSION | 64 |
| 5.1.1 | <i>Zhang et al. model</i> | 65 |
| 5.1.2 | <i>Ziskind et al. model</i> | 66 |
| 5.2 | PARTICLE REMOVAL..... | 68 |
| 6 | DEPOSIT GROWTH..... | 88 |
| 6.1 | DEPOSIT GROWTH: THE PARTICLE PACKING APPROACH..... | 88 |
| 6.2 | DEPOSIT GROWTH: AN ENGINEERING APPROACH | 74 |
| 6.3 | STICKING VELOCITY IN PRESENCE OF A DEPOSIT LAYER..... | 74 |
| 6.4 | RE-SUSPENSION FROM A BED OF PARTICLES | 78 |
| 7 | SIMULATIONS: CASES AND MODELS CONSIDERED | 101 |
| 7.1 | SUMMARY OF PERFORMED SIMULATIONS..... | 101 |
| 8 | VALIDATION OF MODELS AND ALGORITHMS..... | 104 |
| 8.1 | VALIDATION OF THE CODE FOR DEPOSIT FORMATION..... | 104 |
| 8.1.1 | <i>Results</i> | 86 |
| 8.2 | EFFECT OF THE IMPACT ANGLE | 92 |
| 9 | MODEL APPLICATION TO A SIMPLE PROBLEM OF INDUSTRIAL RELEVANCE..... | 118 |
| 9.1 | DEPOSIT ON A WALL BOUNDED SHORT CYLINDER | 118 |
| 9.1.1 | <i>Results</i> | 119 |
| 10 | CONCLUSIONS | 126 |
| | REFERENCES..... | 132 |
| | SUMMARY | 141 |
| | SOMMARIO | 145 |
| | AKNOWLEDGEMENTS | 149 |
| | LIST OF PUBLICATIONS..... | 150 |
| | ABOUT THE AUTHOR..... | 151 |

Nomenclature

Latin letters

| | | | |
|------------|--|-------------|---|
| a | contact radius [m] | F_{BA} | Basset force [N] |
| A | Hamaker constant [-] constant [-] | F_{BU} | buoyancy force [N] |
| a_H | contact radius in Hertzian theory [m] | F_d | force due to deformation [N] |
| a_{JKR} | contact radius in Johnson-Kendall- Roberts theory [m] | f_{def} | deformation factor [-] |
| a_{SB} | contact radius in Savkoor and Briggs theory [m] | F_D | drag force [N] |
| a_0 | contact radius at equilibrium [m] | F_G | gravity [N] |
| B | constant [-] | F_L | lift force [N] |
| C_{cell} | particle concentration in an element [kg/m ³] | f_{dep} | fraction of impacting particles which satisfied the sticking condition [-] |
| C_D | drag coefficient [-] | F_{EL} | contact force at the elastic limit case [N] |
| C_m | mass coefficient [-] | f_{pack} | correction factor [-] |
| c_t | element containing the cloud centre at time t [-] | F_{PG} | pressure gradient force [N] |
| c_t^{ad} | element adjacent to c_t [-] | f_s | static coefficient of friction [-] |
| d_{nod} | distance between an element node and a cloud centre [m] | F_S | other forces [N] |
| d_p | particle diameter [m] | f_s^* | effective static coefficient of friction [-] |
| e | coefficient of restitution [-] | F_0 | force due to the adhesion of a non deformable sphere [N] |
| E_n | normal impact energy [J] | G | shear modulus [Pa] |
| E_t | tangential impact energy [J] | G^* | effective shear modulus [Pa] |
| E_0 | element containing the cloud centre [-] | H | relative approach due to plastic de- formation [m] |
| e_A | coefficient of restitution due to ad- hesive rupture [-] | | hardness of the deformed body [-] |
| e_p | coefficient of restitution due to plas- tic deformation [-] | h_{dep} | deposit thickness [m] |
| E^* | effective Yong modulus in contact of bodies [Pa] | $h_{dep,1}$ | thickness of the first deposit layer [m] |
| F | contact force [N] | $h_{dep,2}$ | thickness of the first two deposit lay- ers [m] |
| F_A | adhesion force [N] | $h_{dep,l}$ | thickness of the first l deposit layers [m] |
| F_{AM} | added mass force [N] | h_{EL} | relative approach at the limiting elastic case [m] |
| F_B | body forces [N] | | |

| | | | |
|---------------|---|-----------|--|
| I_p | moment of inertia of a particle [kg·m ²] | $Q_{A,r}$ | adhesion energy developed during the restitution phase [J] |
| k_e | erosion coefficient [-] | Q_{brk} | energy required to break the contact between two bodies [J] |
| K | elastic constant [Pa] | Q_E | total energy [J] |
| l_0 | characteristic length [m] | Q_{EL} | elastic energy [J] |
| m_{dep} | deposited mass [kg] | Q_K | kinetic energy [J] |
| m_p | particle mass [kg] | Q_P | energy of plastic deformations [J] |
| m_1 | mass of body 1 [kg] | Q_{PE} | elastic energy during plastic deformation [J] |
| m_2 | mass of body 2 [kg] | r | cloud radius [m] |
| m^* | effective mass of bodies in contact [kg] | R | particle radius [m] |
| N | number of nodes in each element [-] | R_c | contact radius [m] |
| | normal contact force [N] | r_{EL} | radius of elastically deformed area [m] |
| n_i | number of particles in the size fraction i [-] | r_p | radius of plastically deformed area [m] |
| n_l | number of deposit layers [-] | r_T | radius of total deformed area [m] |
| n_p | number of particles [-] | R_1 | radius of body 1 [m] |
| N_p | total number of particles in a cloud [-] | R_2 | radius of body 2 [m] |
| $n_{p,dep}$ | number of deposited particles [-] | R^L | Lagrangian autocorrelation function [-] |
| $n_{p,2D}$ | number of particles which cover a given surface [-] | R^* | effective radius of bodies in contact [m] |
| N_0 | pull-off force [N] | R'_1 | radius of the plastically deformed zone of a given body [m] |
| $N_{1,JKR}$ | equivalent Hertzian force in Johnson-Kendall-Roberts theory [N] | R^{*} | effective radius of bodies in contact after plastic deformations [m] |
| $N_{1,SB}$ | equivalent Hertzian force in Savkoor and Briggs theory [N] | Re | Reynolds number [-] |
| N^* | dimensionless contact force [N] | Re_p | particle Reynolds number [-] |
| $N_{1,JKR}^*$ | dimensionless equivalent Hertzian force in Johnson-Kendall-Roberts theory [N] | RM | moment ratio (rolling moment) [-] |
| $N_{1,SB}^*$ | dimensionless equivalent Hertzian force in Savkoor and Briggs theory [N] | RM_{2c} | moment ratio (rolling moment) in the case of a double contact [-] |
| p | sticking probability [-] | RS | sliding ratio [-] |
| \wp | generic point within a cloud [-] | S | surface [m ²] |
| $Q_{A,a}$ | adhesion energy developed during the approach phase [J] | Stk | Stokes number |
| | | t | time [s] |
| | | T | torque [N·m] |
| | | | tangential contact force [N] |
| | | | temperature [K] |

| | | | |
|----------------|--|----------------------|---|
| T_{cv} | temperature of critical viscosity [K] | x_p | particle position [m] |
| t_{max} | maximum simulated time [s] | y | elastic yield limit [Pa] |
| u | fluid velocity [m/s] | Z | generic quantity [accordingly] |
| u_{CC} | fluid velocity at the cloud centre [m/s] | z_0 | separation distance between two bodies [m] |
| u_{cell} | mean fluid velocity in a given element [m/s] | Greek letters | |
| u_t | fluid velocity at time t [m/s] | α_p | volume fraction of the dispersed phase [-] |
| u_0 | characteristic velocity [m/s] | β | exchange coefficient [s ⁻¹] |
| v | particle velocity [m/s] | | fraction of contact radius [-] |
| v_{CC} | particle velocity at the cloud centre [m/s] | γ | free surface energy [J/m ²] |
| v_{cell} | particle velocity in a given element [m/s] | Γ | work of adhesion (surface energy) [J/m ²] |
| $v_{i,n}$ | normal component of the particle impact velocity [m/s] | δ | relative approach [m] |
| $v_{i,n,cell}$ | normal component of the particle velocity to the impact surface of a given element [m/s] | δ_G | relative approach at the separation point [m] |
| $v_{i,t}$ | tangential component of the particle impact velocity [m/s] | η | particle viscosity [Pa·s] |
| $v_{r,n}$ | normal component of the rebounding velocity of a particle [m/s] | η_{ref} | reference viscosity [Pa·s] |
| $v_{s,n}$ | normal component of the sticking velocity [m/s] | θ | impact angle [°] |
| $v_{slip,CC}$ | slip velocity at the cloud centre [m/s] | θ_{cr} | critical impact angle [°] |
| v_t | particle velocity at time t [m/s] | κ_t | tangential stiffness [Pa] |
| $v_{y,n}$ | normal component of the particle yield velocity [m/s] | μ_f | dynamic viscosity [Pa·s] |
| V | control volume [m ³] | ρ_{dep} | deposit bulk density [kg/m ³] |
| V_{cell} | cell volume [m ³] | ρ_f | fluid density [kg/m ³] |
| V_{cloud} | cloud volume [m ³] | ρ_p | particle density [kg/m ³] |
| $V_{p,i}$ | volume of particles in the size fraction i [m ³] | ρ_{2D} | surface packing density [-] |
| W_{cell} | weighting factor [-] | ρ_{3D} | volume packing density [-] |
| x_i | particle position in coordinate direction i [m] | σ_s | standard deviation in coordinate direction s [m] |
| x_t | particle position at time t [m] | τ | time difference [s] |
| | | τ_c | average time between inter-particle collisions [s] |
| | | τ_f | characteristic time of the flow field [s] |
| | | τ_L | Lagrangian time scale [s] |
| | | τ_p | particle response time [s] |
| | | ν_1 | Poisson coefficient of body 1 [-] |
| | | ν_2 | Poisson coefficient of body 2 [-] |

$\vec{\omega}_p$ angular velocity of a particle [rad/s]

Subscripts

1 body 1
2 body 2
f fluid
sur surface

Abbreviations

CFD Computational Fluid Dynamic
COR Coefficient of Restitution
CVM Critical Viscosity Model
EL Eddy Lifetime
FA Feng et al.
FEM Finite Element Method
JKR Johnson-Kendall-Roberts
LES Large-Eddy Simulation
PCT Particle Cloud Tracking
pdf Probability Density Function
PND Particle Number Density
RANS Reynolds Averaged Navier-Stokes
SB Savkoor and Briggs
SPT Single Particle Tracking
SSF Stochastic Separated Flow
TN Thornton and Ning
U-RANS Unsteady Reynolds Averaged Navier-Stokes
vB van Beek

Symbols

$\vec{\quad}$ vector quantity
 $\bar{\quad}$ mean value of a quantity
 \prime fluctuating value of a quantity
 $\langle \quad \rangle$ ensemble averaging operation

CHAPTER 1

Two-phase flows and deposit formation: the problem actuality and needs for modelling

1.1 Introduction

Deposit formation in combustion devices (i.e., boilers, furnaces) is a phenomenon mainly encountered when using solid fuels. The lighter fraction of ash formed during fuel combustion, as well as unburnt residuals and fuel impurities, can be entrained by the gas flow into subsequent device. Depending on operational conditions, fuel characteristics and flow field within the boiler, those entrained particles can impact and adhere to device surfaces (i.e. heat exchangers tubes, superheater, etc.) forming a deposit layer which acts as a thermal insulation. Thus the reduction of heat exchange affects the global efficiency of the device. This problem, which is present even in most fossil fuel combustion devices, can become particularly serious in some biomass-fed boilers. Because of the composition, size, and other factors, fly ashes produced by biomass combustion seem to deposit faster or in a larger amount than those from fossil fuel combustion. Besides the reduced heat exchange rate between flow and heat exchanger makes the flow temperature increase up to critical values which could undermine mechanical strength of some boiler components. Another problem which can occur due to the deposit formation is the reduction of the cross section available to the flow, in some cases reduced to zero because of bridge formation between tubes [1], [2].

In the last decade biomass have been increasingly used as fuel in combustion devices especially in those of small-medium size. Often the configuration of biomass-fed boilers is the same used for coal combustion, thus not optimized for biomass and connected problems. Therefore it is important to study this phenomenon and try to develop a simulation code which can predict where deposit forms and how different boiler geometries respond to deposit formation, so helping the sizing of the device and the scheduling of its maintenance.

1.2 Deposit formation within a solid fuel-fed boiler

Deposit formation within a solid fuel fired boiler is named in two different ways depending on the part of the boiler which is involved. When deposition occurs in radiative zone, i.e, where heat is mainly exchanged by radiation, it is called slagging; on the other hand when deposition occurs in convective zone, i.e, where heat is exchanged mainly by convection, it is called fouling. By definition slagging occurs mainly all around the combustion bed and where flames develop, that is in the zone often called furnace. Since it depends on several factors (i.e., surface temperature, flame temperature, amount and characteristics of entrained particles, etc.), rate and composition of slagging can significantly vary within the furnace. Due to high temperature reached within the furnace, deposits in this zone often melt and slowly slip downward to the boiler bottom, in the ash hopper. In contrast fouling typically involves superheaters, economizer, etc. (Figure 1.1 [3]).

Fouling deposits are almost powdery, with a slow sintering effect due to increasing temperature. In the formation of such a deposit the mechanics of impact, adhesion and rebound play a paramount role.



Figure 1.1 – Deposits accumulated on heat exchanger tubes [3].

1.3 Mechanisms of particle deposition

Deposits form mainly by four different mechanisms (i.e., condensation, chemical reaction, inertia, and thermophoresis) but those involving particles are just inertia and thermophoresis [1]. A brief description of both the mechanisms is given below.

1.3.1. Inertial impact

A fluid flow evolving within a boiler encounters and adapts to several obstacles during its travel (i.e., walls, tube bundles, curves, etc.). Particles dispersed by the flow respond to the changes of flow field according to their mass and flow velocity. Lighter particles respond fastly and follow the streamlines, whilst heavier take more time to respond, thus they can impact on the obstacle surfaces and then rebound or adhere to it depending on the impact conditions (Figure 1.2 [4]).

An important parameter used to identify the behaviour of particles is the *particle response* (or relaxation) *time* τ_p (also called *momentum response time* [5]), defined by:

$$\tau_p = \frac{\rho_p d_p^2}{18\mu_f} \quad (1.1)$$

where ρ_p and d_p are respectively density and diameter of the particle, and μ_f is the dynamic viscosity of fluid. If the particle response time is small in respect to the characteristic time scale of the flow, particle responds quickly to flow changes, otherwise its response lags behind the fluid flow.

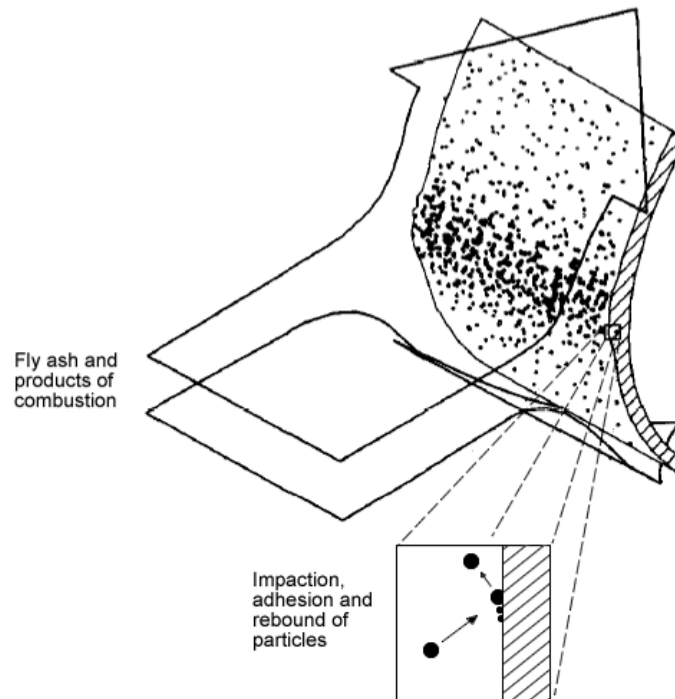


Figure 1.2 – Inertial impact of particles [4].

However τ_p alone is not sufficient to determine the rapidity of a given group of particles to respond to flow changes, because it has to be compared with characteristic time scale of the flow field. A non-dimensional quantity, i.e., Stokes number, can be used at this aim. Stokes number is defined as the ratio between particle response time τ_p and characteristic time of the flow field $\tau_f = l_0/u_0$:

$$Stk = \frac{\tau_p}{\tau_f} = \frac{\rho_p d_p^2 u_0}{18 \mu_f l_0} \quad (1.2)$$

with u_0 and l_0 respectively characteristic velocity and length of the flow field. If $Stk \ll 1$ the response time of the particles is much smaller than the characteristic time of the flow field. In this case the particles will have ample time to respond to changes in flow velocity, and the particle and fluid velocities will be nearly equal (velocity equilibrium). On the other hand, if $Stk \gg 1$, then the particle will have essentially no time to respond to the fluid velocity changes and the particle velocity will be little affected by fluid velocity change.

Inertia is the dominant mechanism of deposit formation when particle size is greater than 3-5 μm [6], thus it is very important in solid-fuel combustion devices (see section 1.4).

1.3.2. Thermophoresis

When particles are present in a flow field and also experience a transverse temperature gradient, they are subjected to a force, the thermophoretic force, which is due to the molecular vibrations of the carrier fluid. Molecules at the high-temperature side of the particle have, on the average, higher kinetic energies. Hence through molecular collisions with the particle, molecules impart to it a high rate of momentum. On the contrary at the low-temperature side the momentum transferred to the particle is low. The net effect of these collisions is a net force in the direction opposite to that of the temperature gradient.

Thermophoretic force becomes significant with submicron and nanoparticles, and may be used for the control of the motion of such particles and their settling or their collection. In the case of tiny particles, the gravitational force, which is proportional to d_p^3 , is extremely small. With a sufficiently high temperature gradient, the thermophoretic force becomes significant enough to control the motion of nanoparticles and to affect their deposition on a cold surface. On the contrary this force has a decreasing effect with increasing deposit height because of the reduction of temperature gradient. An expression of thermophoretic force can be found in [6]-[8].

Since as reported below (section 1.4) most of the particles emitted during the combustion of biomass is in the supermicron range, thermophoretic force is neglected in this study, but can be easily enclosed.

1.4 Size distribution of particles in biomass-fed boilers

Size distribution of fly ash produced during biomass combustion depends on fuel composition, operative conditions of the device, fuel original size, and other factors. Therefore identifying a particle size distribution which characterises fly ash from bio-

mass combustion is an hard task. Experimental studies are available in literature for different biomass (see for example [7], [9]-[11]).

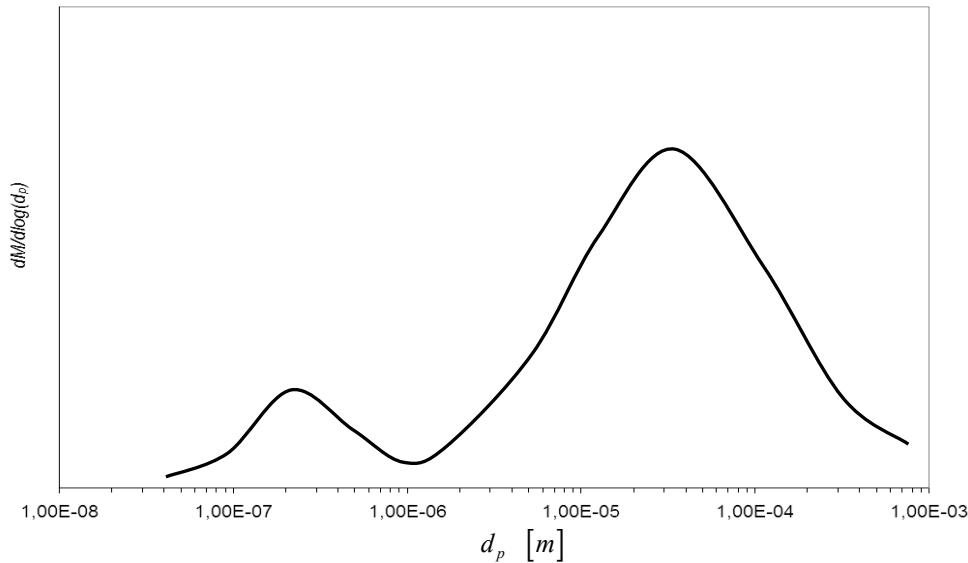


Figure 1.3 – Typical size distribution of fly ash from biomass combustion.

Limiting the observation field to combustion of woody biomass in commercial power end/or heat plants, the task becomes a bit easier. Figure 1.3 illustrates a general trend elaborated averaging data reported in the cited studies. The curve in figure is characterised by two zones: a super-micron zone and a sub-micron one. Mass load of sub-micron particles is usually smaller than that of supermicron ones. Moreover, considering that very small particles usually respond quickly to flow changes (see section 1.3), they follow quite closely the streamlines of the flow not producing a large amount of deposit on a surface. On the other hand larger particles are subjected to bigger forces (i.e., inertia, drag, etc.) therefore they easily left the streamlines and impact an obstacle.

1.5 Two-phase flows classification and modelling

Considering that the term *phase* refers to liquid, solid or vapour state of matter, a multiphase flow is a flow where different phases are mixed together. Multiphase flows can be found in several practical applications, such as transient flows with a transition from liquid to vapour, separated flows (i.e., stratified flows), and dispersed two-phase flows where a continuous carrier phase transports a dispersed one which is present in form of particles, droplets, or bubbles. Since different multiphase flows are subjected to different transport mechanisms, different models have to be adopted. Focusing the attention on dispersed two-phase flows they can be classified according to the different phases being present: continuous/dispersed phase, gas-solid flows, liquid-solid flows, gas-droplets flows, liquid-droplets flows, liquid-gas flows. Dispersed two-phase flows are commonly divided into two flow regimes: the *dilute* and the *dense* one. In dilute

dispersed systems spacing between carried particles is so large that particle interaction is very rare and fluid dynamic forces (i.e, drag and lift) govern particle motion. On the contrary in dense dispersed systems inter-particle spacing is relatively small (i.e. less then 10 particle diameter) and particle motion and transport is governed by collision besides fluid dynamic forces. Calling τ_c the average time between inter-particle collisions, a qualitative estimate of the disperse or dense nature of the flow can be done comparing τ_p with τ_c [5]. The flow can be considered dilute if

$$\frac{\tau_p}{\tau_c} < 1 \quad (1.3)$$

because the particles have sufficient time to respond to fluid dynamic forces before the next collision. On the other hand if

$$\frac{\tau_p}{\tau_c} > 1 \quad (1.4)$$

particles do not have enough time to respond to fluid dynamic forces before the next collision, which means that the flow is dense (Figure 1.4).

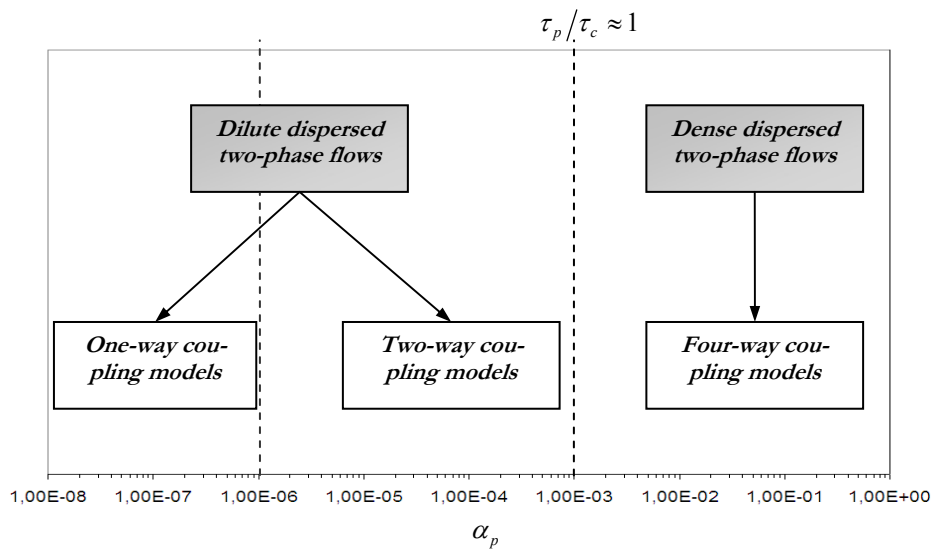


Figure 1.4 – Regimes of dispersed two-phase flows as a function of volume fraction and particle response time.

Another quantity that can be used to identifies the dense or dilute nature of a flow, but mainly to individuate the right modelling approach, is α_p the volume fraction of the dispersed phase [12]. It is defined as the volume occupied by the particles in a unit volume of fluid:

$$\alpha_p = \frac{\sum_i n_i V_{p,i}}{V} \quad (1.5)$$

where n_i is the number of particles in the size fraction i , having the volume $V_{p,i}$, and V is the control volume. If $\alpha_p < 10^{-3}$ the two-phase system can be regarded as dilute. Within this regime, if $\alpha_p < 10^{-6}$ the influence of particles on the fluid flow is negligible, thus a one-way coupling modelling approach can be adopted. Increasing volume fraction, particle interactions with the flow are not negligible, thus in this case at least two-way coupling models should be used. In the dense regime a four way coupling is the model that should be adopted, thus considering the particle-flow interactions as well as the inter-particle interactions (Figure 1.4).

For the applications considered in this work, the order of magnitude of α_p usually is less than 10^{-6} , seldom reaching 10^{-5} . Therefore a one-way coupling approach is used in this work.

1.6 Particle equation of motion

The motion of a solid particle in a fluid is described, using a Lagrangian approach, by an ordinary differential equation which allows the computation of its position and velocity at each time step. This equation, which is called the Basset-Boussinesque-Oseen (BBO) equation, is the translation of the second Newton law. The general form of the BBO equation can be written as follows.

$$m_p \frac{d\vec{v}}{dt} = \vec{F}_D + \vec{F}_{AM} + \vec{F}_B + \vec{F}_{PG} + \vec{F}_{BA} + \vec{F}_S \quad (1.6)$$

m_p is the particle mass, \vec{v} the particle velocity, and t is the time. The right side of equation (1.6) is a sum of six terms, that is respectively the drag force, the added mass force, the body (gravity and buoyancy) forces, the pressure gradient force, the Basset force, and other forces acting on particle. The contribution to particle motion of the different forces is studied by several authors (i.e. [12]-[15]) and depends on the particular application. For high values of density ratio (the ratio between the particle density and the fluid density) forces other than the drag do not give relevant contributions to the particle motion, thus they can be neglected [16], [17]. Assuming this, equation (1.6) rewrites

$$m_p \frac{d\vec{v}}{dt} = \vec{F}_D = -\frac{1}{8} \pi d_p^2 \rho_f C_D (\vec{u} - \vec{v}) |\vec{u} - \vec{v}| \quad (1.7)$$

ρ_f is the fluid density, C_D the drag coefficient, and \vec{u} and \vec{v} are the fluid and particle velocities respectively. C_D is expressed according to the Shiller and Naumann (1933) relation [12]

$$C_D = \frac{24}{\text{Re}_p} (1 + 0.15 \text{Re}_p^{0.687}) \quad (1.8)$$

which is valid for particle Reynolds number (Re_p) up to 1000.

To completely compute the motion of a particle, besides equation (1.7) it has to be considered the differential equation for calculating the particle location and the angular velocity, so giving the complete equations system (1.9),

$$\begin{cases} \frac{d\vec{x}_p}{dt} = \vec{v} \\ m_p \frac{d\vec{v}}{dt} = \vec{F}_D \\ I_p \frac{d\vec{\omega}_p}{dt} = \vec{T} \end{cases} \quad (1.9)$$

where x_p is the particle position, I_p is its moment of inertia, $\vec{\omega}_p$ the angular velocity of particle. \vec{T} is the torque acting on rotating particles due to the viscous interaction with the fluid. Assuming that particle is a non-rotating sphere, the third equation in (1.9) is neglected, and the motion of a particle in time is described just by the first two equations, as in (1.10).

$$\begin{cases} \frac{d\vec{x}_p}{dt} = \vec{v} \\ m_p \frac{d\vec{v}}{dt} = \vec{F}_D \end{cases} \quad (1.10)$$

1.7 Turbulent dispersion of particles: different approaches to modelling

Applications of two-phase flows usually involve turbulent flows, such in the case of the exhausts evolving within a boiler, or the flow crossing a heat exchanger. Turbulence has a direct effect on the particle motion thus it has to be taken into account. Due to the fluctuating character of turbulent velocity field, a dispersion of particle released nominally at the same position is observed, that is particles released from the same position at different time follow different trajectories. This phenomenon is called *turbulent dispersion*.

The trajectory of a particle is computed by solving its equation of motion, the BBO equation (1.7), hence the instantaneous turbulent velocity field should be known. However this information is not provided by all the turbulence models. RANS models, for instance, provide a time-averaged velocity field, on the contrary LES models compute the instantaneous velocity. Therefore depending on the turbulence model adopted also turbulent dispersion has to be modelled.

Besides the problem of evaluating the instantaneous velocity field, it has to be taken into account also the number of trajectories to simulate. In order to obtain statistically

independent results a huge number of trajectories should be tracked, thus requiring a huge computational time. To avoid this limit a model is needed.

Therefore turbulent dispersion models have to accomplish two different tasks: to estimate the instantaneous flow velocity in the position of the particle (if not available, i.e., in RANS simulations), and to reduce the number of particle trajectories which has to be tracked.

In this work a Lagrangian approach is adopted for solid phase tracking, hence a brief review of the possible turbulent dispersion models, available for this approach, is given in the following.

1.7.1 The Stochastic Separated Flow (SSF) approach

There are several versions of this approach (see for instance [14], [16], [18]-[20]), but one of the most commonly used is that called *Eddy Lifetime* (EL) model by Shuen et al. [19]. The instantaneous fluid velocity experienced by the particles is given by summing two terms: the mean velocity predicted by the Eulerian frame (a RANS simulation for instance), and a velocity fluctuation drawn from a Gaussian probability density function. Velocity fluctuations are related to turbulent eddies. Particles interact with a turbulent eddy for the minimum between the eddy lifetime and that the particle takes to cross the eddy. Once a particle crosses an eddy it enters another one, and then a third one and so on, so that the particle trajectory is given by a continuous interaction between the particle and a series of eddies. The eddy lifetime and characteristic length are computed according to the local turbulent properties.

As reported in [7] the main shortcoming of this approach is the large number of particle which have to be simulated. Indeed due to the stochastic nature of EL approach a huge number of particle trajectories is needed in order to obtain a statistically independent results.

1.7.2 The Particle Cloud Tracking (PCT) approach

The PCT approach was first introduced by Baxter in 1989 [21], and then developed and applied by other authors (e.g., [7], [16], [18]), and also implemented in one of the commonly used CFD commercial code. The basic concept is simple: a computed trajectory is not related to a real particle but rather to a virtual one, which represents the mean position in time of a cloud of particles having same characteristics and starting position. Cloud size is evaluated on the basis of the flow and turbulence characteristics. Particle distribution within the cloud is assumed to be Gaussian. Therefore at each time step knowing the mean position, the size, and the particle distribution, a cloud is uniquely individuated. The mean position is computed by solving the ensemble averaged version of the particle equation of motion (1.7).

The PCT approach is used in this work even with LES results (see Chapter 9). Different realizations of a given time interval was extracted from LES and loaded by the code for deposit formation. In this case the flow field between two consecutive realiza-

tions is supposed to remain constant. The PCT model ensemble averages the instantaneous field and then calculates the dispersion of the cloud of particles.

The main advantage of the PCT approach, in respect to the SSF one, is that PCT allows to simulate a large number of particle tracking a small number of trajectories. On the other hand it has some shortcomings. Due to the averaged nature of this model, particle velocity are smoothed and this reflects on the deposit accumulation. Moreover some parameters such as the number of clouds and the initial cloud size, have to be assumed according to the simulated domain, and so far no optimization method is available to this aim. Another important shortcoming is the assumption of a homogeneous turbulence.

A more detailed description of the PCT model is given in section 1.7.

1.7.3 The Single Particle Tracking (SPT) approach

In the last decade computational power is growth rapidly and is still growing day by day. This lets a faster and faster numerical simulation. Thus, besides the two modelling approaches sketched above also the single particle tracking (SPT) approach starts to become applicable, especially for very diluted particle laden flows. In this case no dispersion models have to be introduced, and particle released in the flow are all tracked.

1.7.4 Particle Number Density (PND) approach

Another possible approach to turbulent dispersion is that based on the *particle number density* (see for example [22]). It uses the same concept of the PCT model, that is a parcel of particles is represented by a single trajectory, but here there is a diffusive equation to solve. Particle velocity is decomposed into a convective and a diffusive components. The convective term is computed solving the particle equation of motion, while the diffusive one is computed solving a different equation.

1.8 Turbulent dispersion of particles: the PCT model

As said before in the PCT model a trajectory is related to a cloud of identical particles, not to a single one. The cloud equation of motion is an ensemble averaged version of (1.7) thus it results:

$$\frac{d\langle v_i \rangle}{dt} = -\frac{3}{4d_p} \frac{\rho_f}{\rho_p} C_D (\langle u_i \rangle - \langle v_i \rangle) |\langle \vec{u} \rangle - \langle \vec{v} \rangle| \quad (1.11)$$

where subscript i indicates a coordinate direction, and symbol $\langle \rangle$ the ensemble average of the quantity which encloses.

Since the computational domain is divided into a number of cells, part of which are comprised within a cloud volume, the ensemble average of a generic quantity Z within a cloud at a given time t is computed introducing a weighting factor $W_{cell}(t)$ defined as

$$W_{cell}(t) = \frac{\int_{V_{cell}} pdf(x_i, t) dV}{\int_{V_{cloud}} pdf(x_i, t) dV} \quad (1.12)$$

where V_{cell} and V_{cloud} indicate the volume of a given cell and cloud respectively, and $pdf(x_i, t)$ is the value assumed by the probability density function of particle distribution within the cloud, at point x_i and time t . Hence the ensemble average of quantity Z writes

$$\langle Z \rangle = \sum_{cell=1}^{CL_EL} Z_{cell} W_{cell}(t) \quad (1.13)$$

where CL_EL is the total number of cells comprised within a cloud. For example, the ensemble average flow velocity at time instant t is given by

$$\langle u_i(t) \rangle = \sum_{cell=1}^{CL_EL} \left[u_{i,cell}(t) \frac{\int_{V_{cell}} pdf(x_i, t) dV}{\int_{V_{cloud}} pdf(x_i, t) dV} \right] \quad (i = 1, \dots, 3) \quad (1.14)$$

Time integration of (1.11) provides the ensemble averaged velocity of the cloud; a second time integration gives the ensemble averaged cloud position, that is, in statistical terms, the mean or expected value of the position $\langle x_i(t) \rangle$ at a given time t :

$$\langle x_i(t) \rangle = \int_0^t \langle v_i(t) \rangle dt + \langle x_i(0) \rangle \quad (1.15)$$

To solve (1.14) the pdf has to be known, as well as the cloud size to individuate all the cells of the computational domain comprised in it. Assuming that dispersion of particles in the three coordinate directions (i, j, k) are not correlated, a multivariate Gaussian pdf is considered:

$$pdf(\wp) = pdf_i(\wp) \cdot pdf_j(\wp) \cdot pdf_k(\wp)$$

$$pdf_s(\wp) = \frac{1}{\sqrt{2\pi}\sigma_s} e^{-\left(\frac{x_s - \langle x_s \rangle}{\sigma_s}\right)^2} \quad (s = i, j, k) \quad (1.16)$$

with \wp generic point within the cloud, and σ_s standard deviation from the mean cloud position in coordinate direction s . Decomposing both the position and velocity of a particle into a mean and a fluctuating terms

$$\begin{cases} x_i = \bar{x}_i + x'_i \\ v_i = \bar{v}_i + v'_i \end{cases} \quad (1.17)$$

indicated respectively with $\bar{\quad}$ and \prime , the variance σ_s^2 in particle position in an arbitrary coordinate direction i , writes as

$$\frac{d\langle x_i'^2 \rangle}{dt} \equiv \frac{d\sigma_i^2}{dt} = 2 \int_0^t \langle v'_i(t) v'_i(t_1) \rangle dt_1 \quad (1.18)$$

The product $\langle v'_i(t) v'_i(t_1) \rangle$ expresses the correlation between the velocity fluctuation at two different time instants, which is complicate to evaluate. To overcome this problem Baxter replaces it with more tractable and classical properties of random functions. These are the local rms velocity fluctuations and the Lagrangian autocorrelation function. Both have explicit dependence on time in the general case. The Lagrangian autocorrelation function is defined as

$$R^L(t, t_1) = \frac{\langle v'_i(t) v'_i(t_1) \rangle}{\langle v_i'^2(t) \rangle} \quad (1.19)$$

Substituting (1.19) in (1.18) and time integrating yields

$$\sigma_i^2 = 2 \langle v_i'^2 \rangle \int_0^t (t - \tau) R^L(\tau) d\tau \quad (1.20)$$

An expression of the Lagrangian autocorrelation function can be found if Markovian approximation is assumed. Markovian approximation of stochastic processes assumes that fluctuations of random variables depend on nothing other than their current values. Accepting Markovian approximation, a typical diagonal component of the Lagrangian autocorrelation function for stationary variables becomes

$$R^L(\tau) = e^{-\tau/\tau_L} \quad (1.21)$$

τ is the time difference $t_1 - t$, and τ_L the Lagrangian time constant. The latter quantity can be approximated from turbulence and particle characteristics. In particular it writes

$$\tau_L = \max(\tau_f, \beta^{-1}) \quad (1.22)$$

τ_f is the turbulence time scale defined as

$$\tau_f = \frac{C_\mu^{3/4} k^{3/2}}{\varepsilon \left(\frac{2}{3} k\right)^{1/2}} \quad (1.23)$$

with k turbulent kinetic energy, ε the turbulent energy dissipation rate, an C_μ a constant. β is defined as the exchange coefficient

$$\beta^{-1} = \tau_p \quad (1.24)$$

Substituting the Markovian expression of Lagrangian autocorrelation function (1.21) into (1.16), it results

$$\sigma_i^2 = 2 \langle v_i'^2 \rangle \left[\frac{t}{\tau_L} - \frac{1}{\tau_L^2} (1 - e^{-t\tau_L}) \right] \quad (1.25)$$

with $\langle v_i'^2 \rangle = \langle u_1'^2 \rangle (1 - e^{-\beta\tau_g}) = \frac{2}{3} k (1 - e^{-\beta\tau_g})$. Since $\langle v_i'^2 \rangle$ assumes the same values independently from the coordinate direction, from (1.25) it results $\sigma_i = \sigma_j = \sigma_k$. Cloud radius is assumed to be equal to 3σ .

Time derivative of (1.25) returns the variation of σ as a function of time, thus knowing the cloud radius at a given time instance, the cloud radius at the next time step can be evaluated. Once that new σ is known, *pdf* can be computed from (1.16), and then the new ensemble averaged flow velocity by (1.14). Substituting it into (1.11) and numerically integrating, new cloud velocity is evaluated, and accordingly the new mean position of the cloud from (1.15). The main problem is now how to individuate all the cells within the cloud volume at a given time instant. To this aim the searching subroutine described in Chapter 2 has been developed.

CHAPTER 2

Particle tracking and dispersion algorithms

Dilute dispersed two-phase (gas-solid) flows can be encountered in many forms of industrial practice. For instance in the two cases mentioned in Chapter 3 (a biomass-fed boiler) and Chapter 8 (a tube in cross flow within a combustor), particle concentrations α_p are in the range of 10^{-6} - 10^{-7} . Dilute flows are also encountered in conditioning systems, respiratory apparatus, dispersion of pollutants in air, etc.. Thus in all these cases a one-way coupling model can be adopted.

Assuming this it is possible to separate the numerical simulation of the carrier phase from that of the dispersed phase. The code for deposit prediction developed for the present study can then work with flow field generated by RANS simulations (steady and unsteady), as well as LES. Depending on the approach adopted for the flow field simulation the appropriate particle tracking and dispersion model is chosen. As reported in Chapter 1, for RANS flow fields the PCT approach is available, and others can be easily implemented, whilst for U-RANS or LES also SPT approach can be adopted.

In the following paragraphs the main parts of the code are described.

2.1 Outline of the code for deposit prediction

Figure 2.1 shows a schematic of the deposit formation code.

Since a one-way coupling approach is adopted, the flow field is computed by a separated CFD simulation, thus it is taken as an input from the deposit prediction code. Some first pre-processing operations (e.g. construction of the adjacency matrix, calculation of nodal quantities, etc.) are done. The main program is enclosed into two cycles: the first one is the time cycle, the second is the particle cycle which comprises all the computations repeated for each particle. If a particles is captured by a recirculation zone it could neither deposit nor exit from the domain, thus the program would never finish.

To avoid this problem a maximum in the simulated time (t_{max}) is imposed. At the beginning of each time step and for a given particle, particle velocity and position are known (computed in the previous time step or assigned). If the particle is deposited in a previous time step, at the beginning of the new one the re-suspension (see Chapter 5) condition is checked: in the case that re-suspension occurs particles is re-entrained by the flow, otherwise it remain stuck and the code cycle to the next particle. If the particle is not already stuck to any surface, assuming that its velocity remains constant in the time step under consideration, the new particle position, that is the particle position at the end of the time step, is computed. During the time step the particle might hit the domain boundary which could be a wall or not. In the former case the particle can adhere to the wall or bounce being re-entrained by the flow: if the adhesion condition is satisfied particle adheres to the wall and is removed from the domain. Deposited mass and deposit characteristics are accordingly updated, and the computation continues with other particles. If the adhesion condition is not satisfied the particle bounces and the rebound velocity is evaluated. The new particle velocity is also evaluated in the case that particle does not hit any boundary, that is it simply moves within the domain.

At the end of the time step under consideration, for each particle which is still within the domain the new velocity and position are known, so the time cycle can start again.

Disregarding the pre-processing computations, the main code is divided into several subroutines. In the following sections of this chapter the models and algorithms for particle tracking and dispersion are discussed. Impact and adhesion models are presented in Chapter 4, those for re-suspension in Chapter 5, and deposit growth models are discussed in Chapter 6.

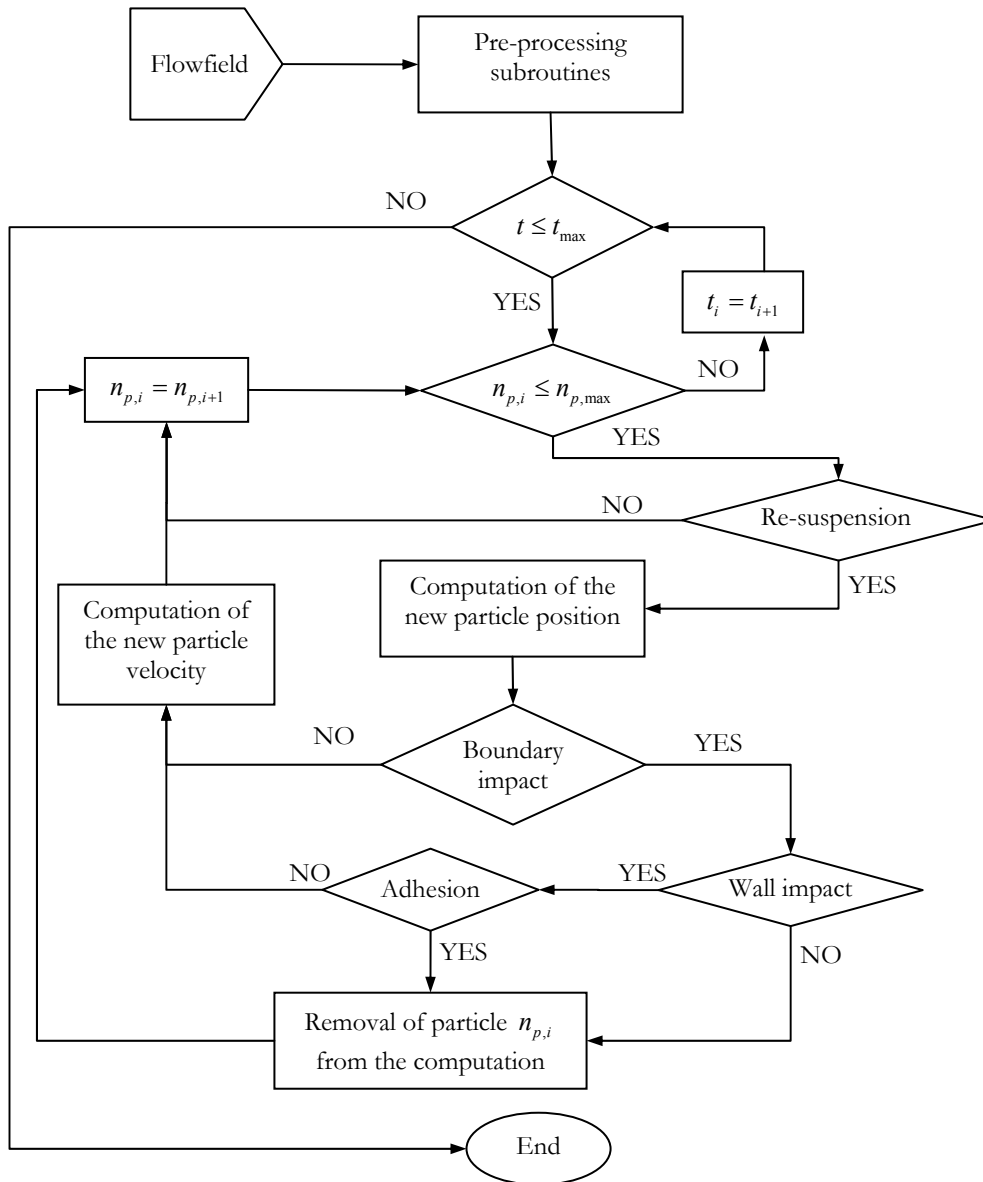


Figure 2.1 – Algorithm of the code for deposit prediction.

2.2 Algorithm for particle tracking

The particle tracking subroutine is divided into two parts: one integrates the first of (1.10) using a finite difference approach, and computes the new particle position within the domain. The second part integrates the second of (1.10) using the Modified Euler predictor-corrector method.

The algorithm for particle tracking is sketched in Figure 2.2.

The domain is divided into (hexahedral) cells and in order to know the fluid velocity at a given time step t , the cell containing the particle has to be identified. At a given time step t particle and fluid velocities (\vec{v}_t, \vec{u}_t) are known, as well as the initial particle position \vec{x}_t and element c_t which contains it. Assuming \vec{v}_t constant during the time interval dt , by integrating the first of (1.10) particle position at time $t+dt$ is computed. The new cell containing the particle, c_{t+dt} in figure, is then individuated starting from the previous one c_t , so the new fluid velocity \vec{u}_{t+dt} can be computed.

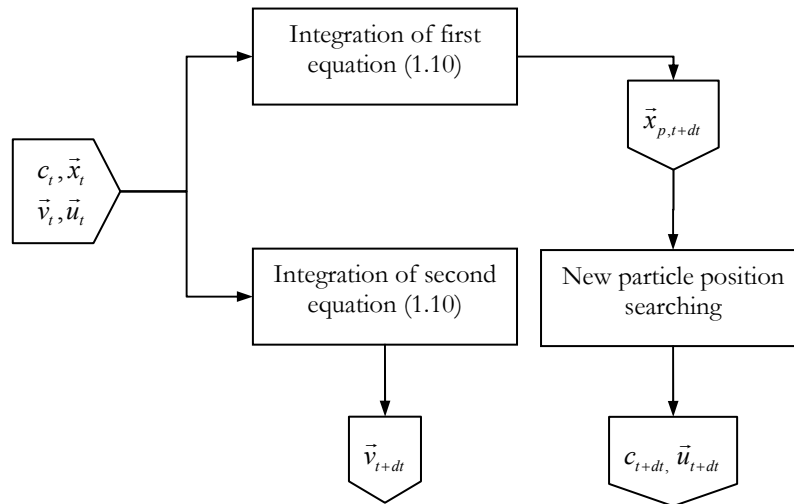


Figure 2.2 – Algorithm for particle tracking.

In the second part of the algorithm, the second of (1.10) is time integrated and the new particle velocity \vec{v}_{t+dt} is then computed. This procedure is repeated at each time step.

The search of the cell containing a particle is done in a local reference. As said before the domain is divided into cells (hexahedral in this work), which in general may be stretched and distorted to better fit the domain geometry. Individuating when a particle exit from an element and enter a new one is complicated in physical domain. To overcome this difficulty the physical domain is connected to a logical one composed by identical cubic cells. Each cell has a local reference system originating in the centre of the cell, in which the cell vertexes have coordinates equal to ± 1 (Figure 2.3). In this reference it is easily individuated whether a particle exit from a cell and enter another. The passage from the global reference to the local one is done using a Finite Element approach, that is using shape functions.

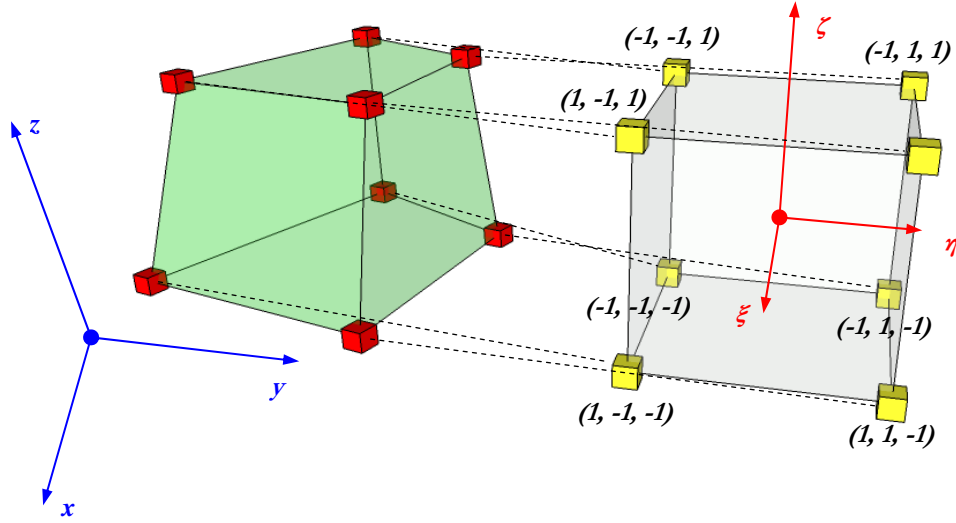


Figure 2.3 – Global (left) and local (right) references.

The algorithm of this search procedure, which was presented in [23], is reported below.

Definitions

- c_t : element which hosts the particle (P) at a given time t ;
- $c_{t+\Delta t'}$: element which hosts the P at a time $t + \Delta t'$
- Δt time step;
- $\Delta t'$ partial time step;
- Δt_{exit} time interval to reach the exit face from the host element;
- $\Delta t_{resid} = \Delta t - \Delta t_{exit}$ residual time step;
- $\xi_{\alpha}^{EL}, (\alpha = 1, \dots, 3)$ local coordinates in the generic finite element EL at a given time t ;
- $\dot{\xi}_{\alpha}^{EL}, (\alpha = 1, \dots, 3)$ local velocity components in the generic finite element EL at a given time t ;
- Condition A: true if $\Delta t_{resid} > 0$ (at the beginning $\Delta t_{resid} = \Delta t > 0$);
- Condition B: true if $c_{t+\Delta t'}$ is $\neq 0$ (at the beginning $c_{t+\Delta t'} = c_t$, thus $c_{t+\Delta t'} \neq 0$; $c_{t+\Delta t'}$ becomes 0 if P position is outside the domain);
- Condition C: true if at least one of the absolute values of the new local coordinate results > 1.0 ;

Algorithm

- 1 – Calculating the new local coordinates of the P referred to the element c_t

$$P_{t+\Delta t} \equiv \left\{ \xi_{\alpha, new}^{c_t} = \xi_{\alpha}^{c_t} + \Delta t \cdot \dot{\xi}_{\alpha}^{c_t} \right\}, \quad (\alpha = 1, \dots, 3)$$

and their absolute values;

- 2 – Evaluating condition C (at the beginning of each time step conditions A and B are always true);
- 3 – **if** condition C is false (i.e. the P does not leave c_t in the time step under consideration) then:

$$\left\{ \xi_{\alpha}^{c_t} \right\} \equiv \left\{ \xi_{\alpha, new}^{c_t} \right\}, \quad (\alpha = 1, \dots, 3);$$

else

A – do while conditions A **and** B **and** C are true;

A1) evaluating the distance $d_{\alpha, j}^1$ between P and each possible exit faces from $c_{t, j}$ (that is the faces having a normal direction corresponding to those coordinates with absolute values > 1.0);

A2) evaluating the time $\Delta t_{exit, \alpha} = d_{\alpha, j} / \dot{\xi}_{\alpha, j}^{c_t}$ that the P takes to reach the exit faces: the smallest one is the exit time $\Delta t_{exit, j}$, and the corresponding possible exit face becomes the actual exit face ($NFACE_j$) from $c_{t, j}$;

A3) evaluating the exit point (intersection between P trajectory and $NFACE_j$) from $c_{t, j}$ at time $t + \Delta t_{exit, j}$:

$$P_{t+\Delta t_{exit, j}} \equiv \left\{ \xi_{\alpha, exit}^{c_{t, j}} = \xi_{\alpha}^{c_{t, j}} + \Delta t_{exit, j} \cdot \dot{\xi}_{\alpha}^{c_{t, j}} \right\}$$

A4) individuating the new host element $c_{t+\Delta t', j}$ (it shares $NFACE_j$ with $c_{t, j}$);

A5) **if** it results $c_{t+\Delta t', j} = 0$ (i.e. the P is out of the domain) then:

A5.1) **if** the *adhesion condition*² is not satisfied the P rebounds on $NFACE_j$, then:

- Imposing $c_{t+\Delta t', j} = c_{t, j}$;
- calculating the rebound velocities consistently with the rebound direction;

else the particle deposits on $NFACE_j$ (going to **4**);

end if

else (i.e. the P does not leave the domain) transporting coordinates and velocity from the exit point in $c_{t, j}$ to the inlet point in $c_{t+\Delta t', j}$:

$$\left\{ \begin{array}{l} \xi_{\alpha}^{c_{t, j}} \\ \dot{\xi}_{\alpha}^{c_{t, j}} \end{array} \right\} \equiv \left\{ \begin{array}{l} \pm \xi_{\alpha, exit}^{c_{t, j}} \\ \pm \dot{\xi}_{\alpha, exit}^{c_{t, j}} \end{array} \right\}, \quad (\alpha = 1, \dots, 3)$$

end if

A6) calculating the residual time interval: $\Delta t_{resid, j} = \Delta t_{resid, j-1} - \Delta t_{exit, j}$;

A7) variables updating: $c_{t, j} = c_{t+\Delta t', j}$;

A8) calculating the new local coordinates of the P referred to the new $c_{t, j}$:

$$P_{t+\Delta t'} \equiv \left\{ \xi_{\alpha, new}^{c_{t, j}} = \xi_{\alpha}^{c_{t, j}} + \Delta t_{resid, j} \cdot \dot{\xi}_{\alpha}^{c_{t, j}} \right\}, \quad (\alpha = 1, \dots, 3);$$

A9) conditions A, B, and C updating;

¹ Index j represents the **A - do while** cycle step. At the first step results $c_{t, j} = c_t$.

² Adhesion criteria are discussed in Chapter 4.

A10) if condition C is false then variable updating:

$$\left\{ \xi_{\alpha}^{c_{t,j}} = \xi_{\alpha, new}^{c_{t,j}} \right\}, \quad (\alpha = 1, \dots, 3)$$

end do

end if

4 – New coordinates and velocity are

$$\left\{ \begin{array}{l} \xi_{\alpha}^{c_{t,j}} \\ \dot{\xi}_{\alpha}^{c_{t,j}} \end{array} \right\}, \quad (\alpha = 1, \dots, 3),$$

and the new host element is $c_{t,j}$.

Knowing particle velocity and position at a given time t and referred to the local reference of element c_t , the new position and the absolute values of its components are computed. If none of these absolute values results greater than 1.0 this means that the particle does not leave c_t in the time step under consideration, so the particle tracking procedure ends. Otherwise the particle leaves c_t and the new element has to be individuated. To this aim, after the calculation of the exit point from c_t , by the evaluation of the minimum distance of the particle from the probable exit faces, and the time to reach them, it is checked whether the exit face is a boundary one. If this is the case the condition for particle adhesion is evaluated and the particle possibly deposits, so being deleted from the particle tracking procedure. In case the adhesion condition is not verified, rebound velocity is evaluated and the particle tracking procedure continues from the rebound point. If the exit face is not a boundary one, the adjacency matrix provides the element c_t^{ad} bordering c_t by the individuated exit face, then the exit point from c_t is converted into the entry point in c_t^{ad} , and the computation restarts from there. This procedure continues until either the new position and element are found, or particle deposits, or particle leaves the domain. A sample situation is sketched in Figure 2.4: during a given time step the trajectory starting from the red point in element A reaches the green point in element B . In a first sub-step (Figure 2.4a) the algorithm computes the distance between the red point and the possible exit faces, and then the exit point (the blue in Figure 2.4b). Exit point from element A becomes the entry point in the new temporary element D . In a second sub-step algorithm finds that trajectory also exits the element D , so the exit face and point (the brown one in Figure 2.4c) are individuated. Exit point from element D becomes entry point in element E . In the last sub-step the algorithm finds that the trajectory does not leave the element E thus the final point is computed (Figure 2.4d).

2.3 Algorithm for cloud search

The problem of individuating all the domain elements which are comprised in a cloud may be easily solved scanning all the domain elements from first to last. Considering that most of these elements are outside the cloud for most of the simulation, this

simple routine results in an unnecessary waste of computation time. An optimized search subroutine has then been developed.

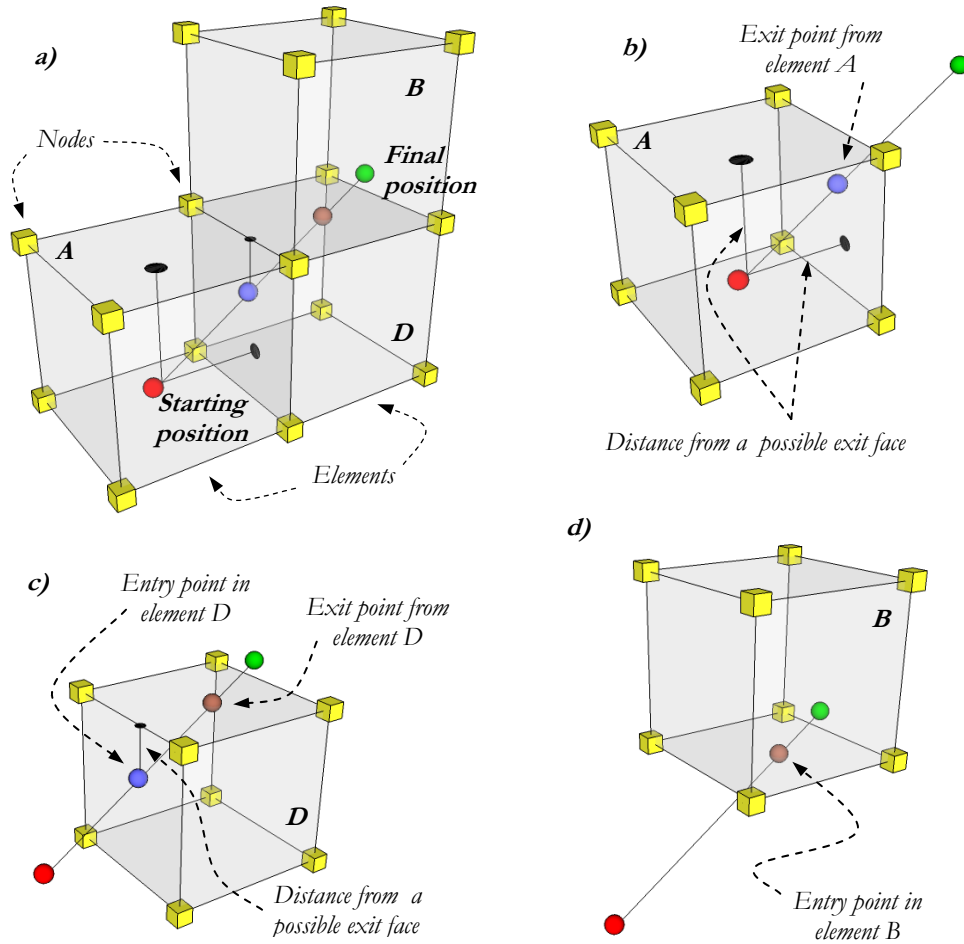


Figure 2.4 – 3D sketch of the algorithm for particle tracking. (a) Starting (red) and ending (green) points. (b) Evaluation of the distance between starting point and possible exit faces, and computation of the exit point (blue) from element A. (c) Evaluation of the distance between the starting point in element D (the blue one) and the exit face, and computation of the exit point (the brown one). (d) Evaluation of the ending point and element B which contains it.

The criterion used to individuate whether an element is enclosed into a cloud having radius r , is the distance d_{nod} of its nodes from the cloud mean position: if $d_{nod} < r$ for at least one node ($nod=1, \dots, N$; N is the number of nodes in each element), the element is considered within the cloud (Figure 2.5).

Recalling that the particle tracking subroutine described in section 2.2 besides the cloud position provides also the domain element which comprises it, the cloud search algorithm starts from that element. Since the number of cells within the cloud is unknown a dynamical structure is used to store them. First element of this list is the cell E_0 which contains the cloud mean position. Then it starts to check all the cells surrounding E_0 . In case that a cell results within the cloud it is added as the last element of the list. Once all the cells surrounding E_0 are checked, the algorithm starts to check cells which

surround the second element in the list, adding a new element to the list every time a cell results within the cloud. The algorithm stops when the cells surrounding each of the element of the list are checked.

Since cloud radius and mean position may vary at each time step, this algorithm is repeated at each time step thus enclosing within the cloud some new cells and excluding some old ones.

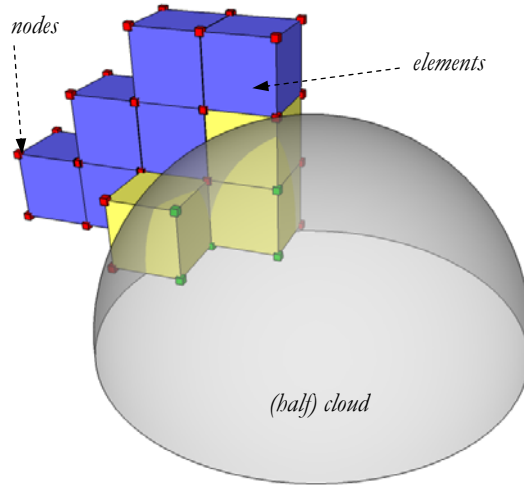


Figure 2.5 – Sketch of a (half) cloud with some domain elements and their nodes. Green nodes and yellow elements are within the cloud; red nodes and blue elements are outside the cloud.

2.4 Evaluation of the particle local velocity in the PCT model

When using a SPT approach the particle deposition criterion is intuitive: once a particle impacts a wall the adhesion model (see Chapter 4) evaluates whether it sticks or bounces. On the other hand using the PCT model is a bit different because information about single particles are lost, as said in Chapter 1. In this case the adhesion model is called by the cloud search subroutine once the cloud approaches a wall, that is when the cloud comprises a boundary (wall) element. Assuming that all the particles within the boundary cell have the same velocity, the number of particles which impacts the wall in a time interval Δt writes

$$n_p = C_{cell} v_{i,n,cell} \Delta t \quad (2.1)$$

where C_{cell} is the particle concentration in the cell, and $v_{i,n,cell}$ is the component of impact velocity normal to the wall of the cell. C_{cell} is given by the *pdf* introduced before (section 1.8)

$$C_{cell} = N_p \cdot W_{cell} \quad (2.2)$$

N_p is the total number of particles in a cloud. Impact velocity has to be evaluated somehow on the basis of the mean velocity of the cloud which is the only available. To this aim in this work is assumed that the ratio between slip $v_{slip,CC}$ and flow u_{CC} velocity at the mean position of the cloud is the same for every cell of the cloud

$$\frac{v_{slip,CC}}{u_{CC}} = \frac{v_{slip,cell}}{u_{cell}} \quad (2.3)$$

Since $v_{slip,CC} = u_{CC} - v_{CC}$ and $v_{slip,cell} = u_{cell} - v_{cell}$, particle velocity in a boundary cell writes

$$v_{cell} = u_{cell} \left(1 - \frac{v_{slip,CC}}{u_{CC}} \right) \quad (2.4)$$

so the component normal to the wall can be computed.

Once all the quantities in (2.1) are known, the number of deposited particle in the time step under consideration is given by

$$n_{p,dep} = f_{dep} C_{cell} v_{i,n,cell} \Delta t \quad (2.5)$$

f_{dep} is the fraction of impacting particles which satisfied the sticking condition and depends on the adhesion model adopted. Multiplying n_{dep} by the particle mass returns the mass deposited during a given time step.

CHAPTER 3

Preliminary test of conventional approaches to an industrial flow

In the following paragraphs some preliminary results for an industrial problem will be presented, primarily as an introduction to the problem and illustration of its challenges. The case considered is a biomass-fed furnace and the numerical simulation performed uses a simplified engineering approach. Particle transport and dispersion is modelled using the PCT model (section 1.8), while the adhesion mechanism is modelled adopting the particle sticking probability approach which will be discussed in section 4.5.

3.1 Deposit in a biomass-fed boiler

In Figure 3.1 a schematic of an actual biomass-fed furnace is shown. This furnace has a fixed-bed and a cochlea feeder which feeds the fuel from the bottom of the grate. The furnace has a cylindrical shape and all around its wall there are tubes where water is transformed into steam. Tubes are protected from direct flame by a refractory wall. Exhaust exit the furnace through a large tube connected to the exhaust extraction system. Bottom ashes are collected just after the grate and extracted by an ash hopper, whilst fly ashes entrained by the flow are transported through the furnace toward the exhaust extraction system and then separated from the gas thanks to a cyclone.

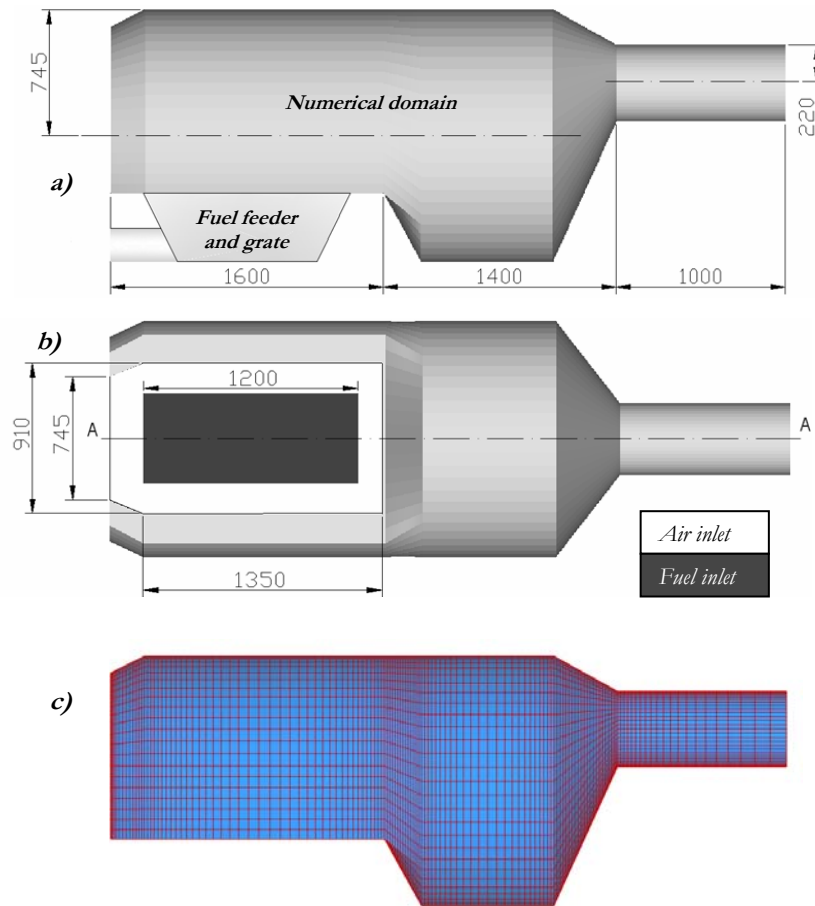


Figure 3.2 – Schematic of a biomass-fed furnace. (a) Numerical domain; (b) secondary air and fuel gas inlet; (c) mesh.

Particle deposition rate depends upon composition and temperature of both the ash and the deposit itself, as well as upon the flow-field. In order to quantitatively evaluate the process of deposit formation on the furnace walls, the fly ash mass size distribution assumed in this work is estimated by averaging the size distribution curves for wood chip and waste wood in [25]. The average size distribution curve is reported in Figure 3.3. Note that in the figure particles smaller than $1 \mu\text{m}$ are neglected. This is because, as said before, this thesis is focused on inertial deposition which becomes relevant for super-micron particles.

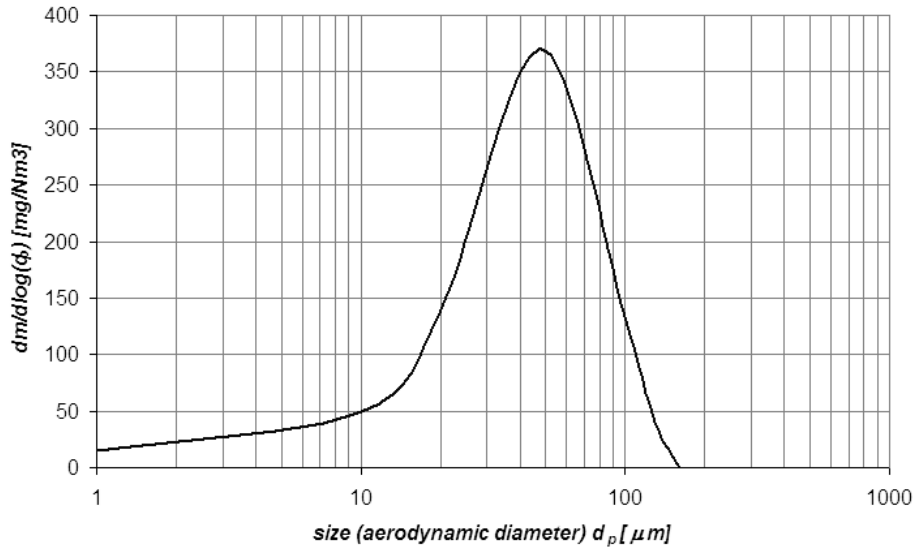


Figure 3.3 – Assumed mass size distribution of coarse fly ash formed during biomass combustion.

For computational purposes, the whole range of particle size is divided into 8 classes, from 1 to about 150 μm , reported in Table 3.1. Each class in turn is subdivided into 12 clouds each containing the same number of particles (indicated in Table 3.1), and starting from the positions shown in Figure 3.4. In order to compute the number of particles in each size class, the particle cloud mass per unit (normal) volume in each class is derived from Figure 3.3 by an appropriate integration over the size range of the class. The result is then multiplied by the (normal) volumetric flow rate so obtaining the particle mass rate for each class, and the relevant number of particles entering the chamber per unit time is simply derived by dividing the latter by the representative mass of the particles of the given class.

| <i>Size Class</i> | <i>Particle mass</i> <i>mg/Nm³</i> | <i>Average Diameter</i> <i>[m]</i> | <i>Particle mass flux</i> <i>kg/h</i> | <i>nr of particles per h</i> |
|-------------------|--|---------------------------------------|--|------------------------------|
| 1 | 145,44 | 1,10E-05 | 0,029263 | 3,4991E+09 |
| 2 | 153,6 | 3,10E-05 | 0,030904 | 1,6510E+08 |
| 3 | 146,24 | 5,10E-05 | 0,029423 | 3,5302E+07 |
| 4 | 100,16 | 7,10E-05 | 0,020152 | 8,9612E+06 |
| 5 | 87,2 | 9,10E-05 | 0,017545 | 3,7054E+06 |
| 6 | 13,28 | 1,11E-04 | 0,002672 | 3,1094E+05 |
| 7 | 5,04 | 1,31E-04 | 0,001014 | 7,1790E+04 |
| 8 | 1,12 | 1,51E-04 | 0,000225 | 1,0417E+04 |
| Total | 652,08 | - | 0,131198 | 3,7125E+09 |

Table 3.1 – Size classes for ash distribution.

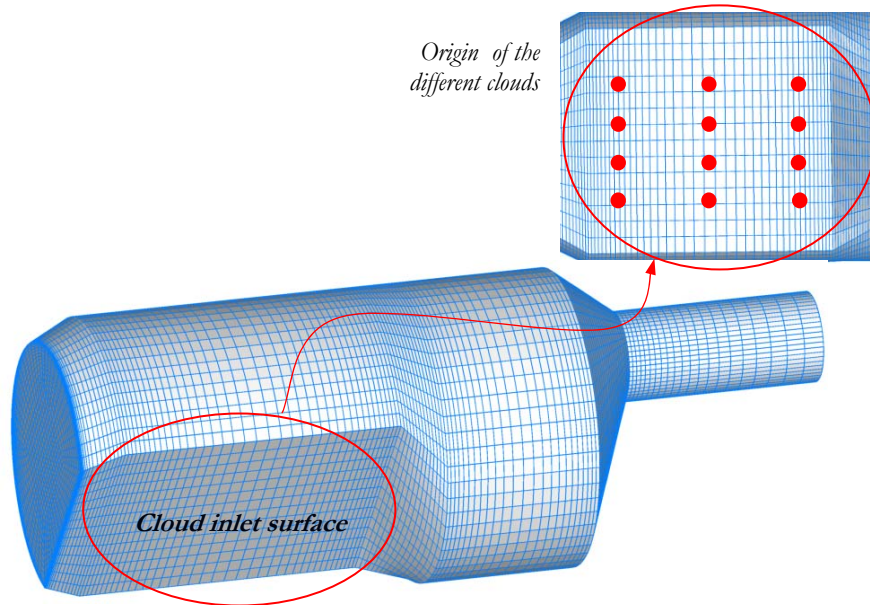


Figure 3.4 – Assumed origins of particle clouds.

The number of particles in each cloud does not satisfy the condition for considering a one-way coupling model (see Chapter 1), but since the flow field is stationary cloud starting from the same origin follows the same trajectory, therefore in the same cloud one can consider the number of particle which are released during whatever time interval one want to study without invalidate the condition for one-way coupling. Simulations are performed changing a bit the initial position of the cloud and then averaging the results.

3.4.1 Results

Figure 3.5 through Figure 3.9 [23] give the predicted deposition rate, expressed as mass per unit surface per h [$\text{kg}/\text{m}^2\text{h}$]. In particular, Figure 3.5 through Figure 3.7 give the mass of the 1st, 2nd, and 3rd size classes respectively, whereas Figure 3.8 and Figure 3.9 show the total mass, in two different views.

As shown in the figures, the location of the zones of preferential deposition depends on the particle size: finest particles (1st size class, 11 μm diameter), which closely follow the flow because of their low inertia, mainly deposit on the upper part of the furnace, and in the region between the furnace and the outlet pipe, as seen in Figure 3.5a: this is due to both the particle inertia and temperature, which in that zone reaches the highest values, see Figure 3.10, thereby increasing the particles stickiness. Deposits also form on the bottom of the furnace, just downstream the inlet plane, but such a contribution is less important, see Figure 3.5b. The gravity force has a greater weight on large particles, thus the preferential deposition zone shifts, as seen by comparing Figure 3.6, showing the deposit formed by 2nd size class particles (31 μm), and Figure 3.5. For such particles, deposit accumulation preferentially occurs in the region connecting the fur-

nace and the outlet pipe, whereas the upper wall is less exposed to deposit formation. The gravity effect is even more pronounced for the 3rd size class particles (51 μm), as shown in Figure 3.7: such deposits mainly accumulate on the bottom surface of the furnace. Larger size particles (size classes from 4th to 8th), do not leave the combustion bed at all, because the flow inlet velocity is not sufficient to drag them. Hence, the total deposit, shown in Figure 3.8 and Figure 3.9, is computed by considering only the contribution of the first three size classes.

On the whole, the zone most exposed to deposit formation is the bottom of the furnace, where a large recirculation bubble (as reported in Figure 3.11 and Figure 3.12 [23]) forces particles with a large inertia to deposit over the walls. This bubble is also responsible for the deposits accumulated in the zone between the furnace and the outlet pipe.

It is interesting to notice the presence of a small amount of deposit on surfaces close to the inlet: as shown by the deposit isocontours in Figure 3.9 and Figure 3.12, elongated vortices there foster the preferential deposition of the heaviest particles.

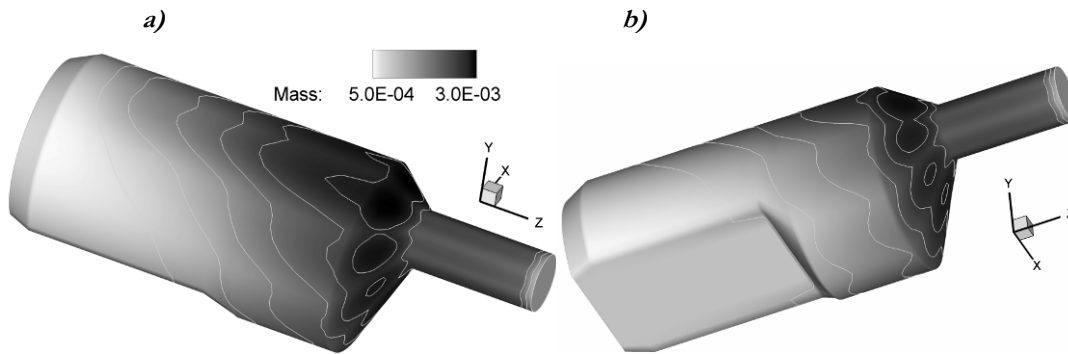


Figure 3.5 – Deposit rate [kg/m²h] formed by 1st size class particles [23].

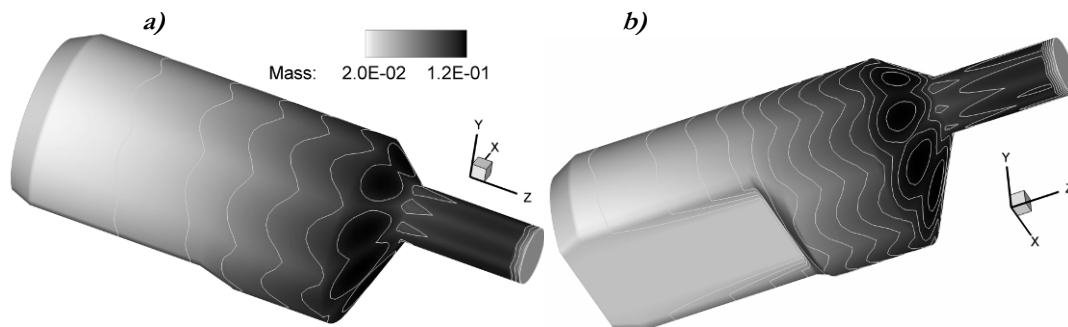


Figure 3.6 – Deposit rate [kg/m²h] formed by 2st size class particles [23].

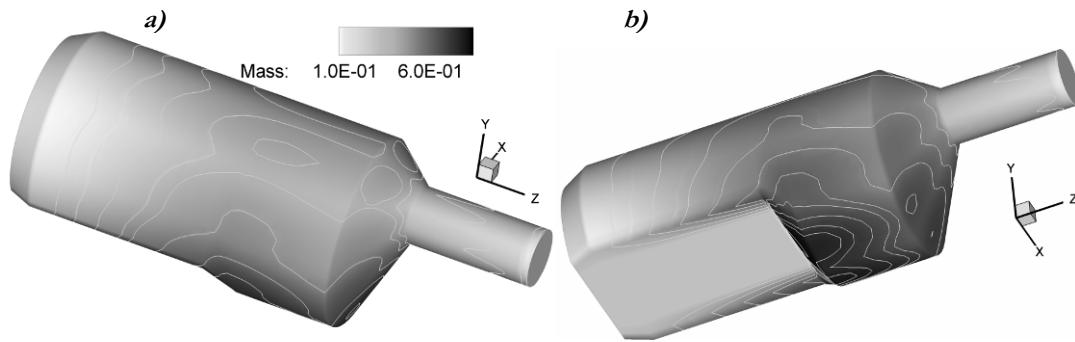


Figure 3.7 – Deposit rate [kg/m²h] formed by 3rd size class particles [23].

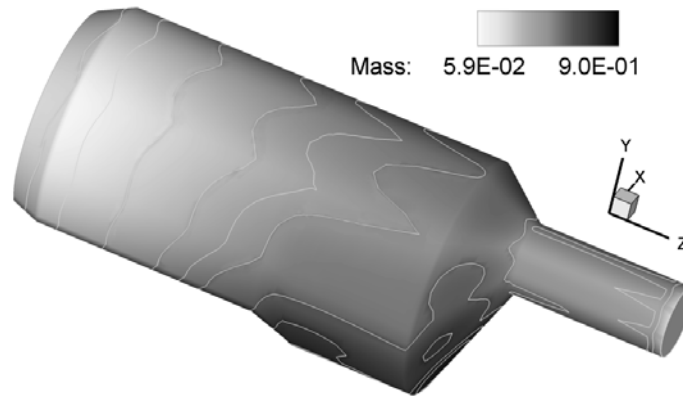


Figure 3.8 – Total deposit rate [kg/m²h] (top view) [23].

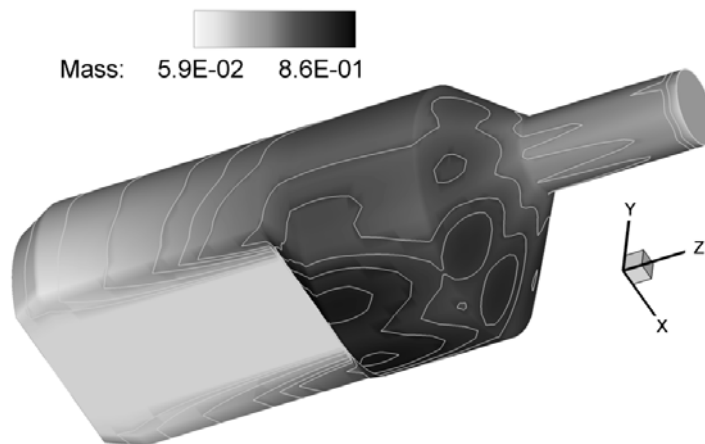


Figure 3.9 – Total deposit rate [kg/m²h] (bottom view) [23].

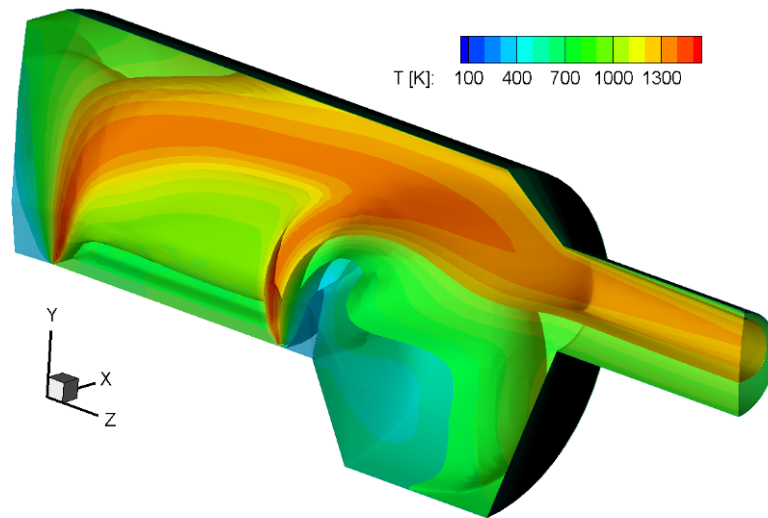


Figure 3.10 – Temperature inside the furnace.

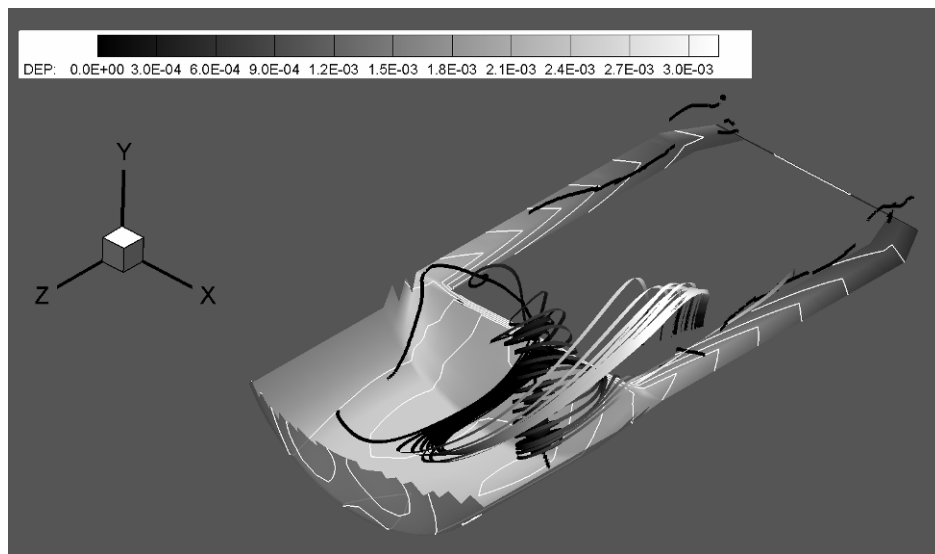


Figure 3.11 – Streamtraces (ribbons), vortex cores (black lines), and deposit rate isocontours (white lines) [kg/m²h] close to the bottom furnace wall [23].

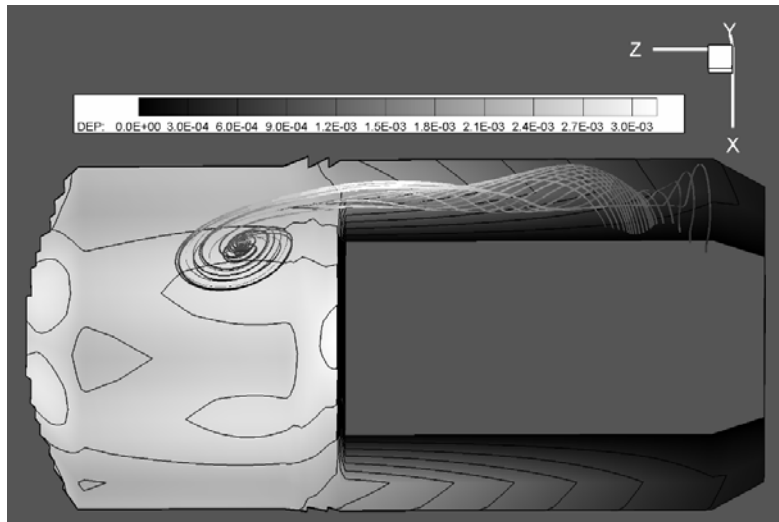


Figure 3.12 – Streamtraces and deposit rate isocontours [kg/m²h] near the inlet zone (section at the inlet surface height; top view) [23].

Cloud trajectories are reported in Figure 3.13: red, blue and green lines represent the trajectories of 1st, 2nd and 3rd size class of particle respectively. Once the cloud mean position hits a wall trajectory goes on until it exits from the outlet surface or all the particles which it contains are deposited. The analysis of trajectories shows that the latter case is never verified, thus clouds continues their motion until the exit face is reached.

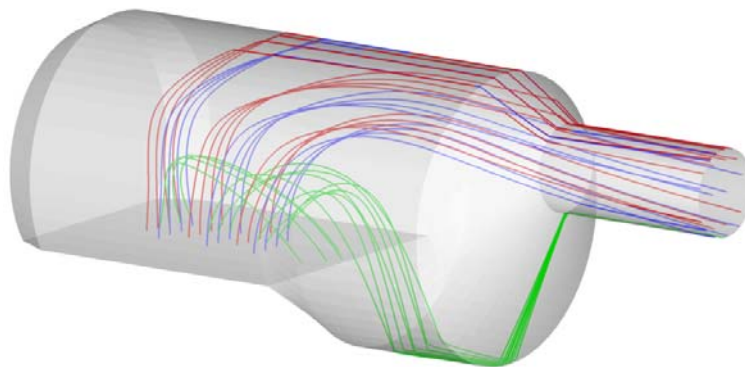


Figure 3.13 – Cloud trajectories. Red, blue and green lines represent the trajectories of the 1st, 2nd and 3rd class size, respectively.

One of the aims of the prediction of deposits within a boiler is helping the sizing. In this case simulation reveals that most of the particles are collected at the bottom of the furnace, just where the ash hopper is placed. Thus can be concluded that this position of ash hopper, chosen to better extract the bottom (heavy) ash, is a good choice even to extract a part of flying ashes deposited within the furnace.

As far the modelling the simulation shows that the PCT approach has high potentialities, but smoothing the effect of local particle and flow velocities provides predictions

which can be unreal or too coarse. In order to avoid this problem a modification of the model has to be proposed (section 2.4), or a different model should be adopted. Although better dispersion models can be implemented into the code, since this is not the focus of the present work, this aspect is not further discussed.

CHAPTER 4

Particle impact and adhesion

Once a particle hits a surface in order to predict deposition rate the impact/adhesion phenomenon has to be modelled determining whether the particle sticks or bounces. Thus it is important to analyse the mechanics of impact. Classical studies on the contact/impact problem can be divided into three chronological stages [26]. In the first one models were restricted to rigid bodies. The main idea was based on the Newton's third law and Coulomb's friction law. In the second stage local elasticity over the contact area was included. Application of Hertz's work on the static contact problem was taken as reference. In the last stage the contact/impact problem is studied using numerical simulations.

In the following paragraphs the physics of two bodies impact is analysed.

4.1 Normal impact

The impact of microparticles with a surface has been a long-standing issue of extensive interest due to its importance in several industrial applications. The point is understanding the physical mechanisms associated with particle impact in order to extrapolate a criterion for particle adhesion/rebound.

At the end of the 19th century Hertz was one of the first scientists who introduced the elasticity in impact problems. Consider two spheres of mass m_1 and m_2 , and radii R_1 and R_2 respectively. Define the effective mass m^* and radius R^* as

$$\begin{cases} \frac{1}{m^*} = \frac{1}{m_1} + \frac{1}{m_2} \\ \frac{1}{R^*} = \frac{1}{R_1} + \frac{1}{R_2} \end{cases} \quad (4.1)$$

Hertz demonstrated that the shape and size of the zone of contact is directly connected to the elastic deformations of the bodies. The shape is a circle and its radius is computed by (4.2).

$$a_H^3 = \frac{3}{4} \frac{FR^*}{E^*} \quad (4.2)$$

where F is the contact load, and E^* is

$$\frac{1}{E^*} = \frac{1-\nu_1^2}{E_1} + \frac{1-\nu_2^2}{E_2} \quad (4.3)$$

with E_1 and E_2 Young modulus of the two bodies, and ν_1 and ν_2 Poisson coefficients. Due to the local compression in the contact zone distant points in the two bodies approach each other by a distance δ (also called *relative approach*) given by (4.4)

$$\delta^3 = \frac{9}{16} \frac{F^2}{R^* E^{*2}} \quad (4.4)$$

δ gives the measure of deformation occurred in the two bodies (Figure 4.1).

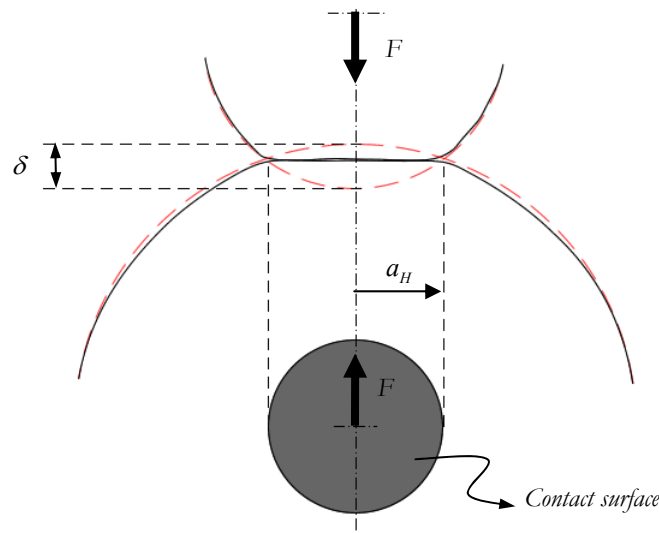


Figure 4.1 – Hertz theory: contact between spheres.

Hertz theory is correct for high values of contact load but not for low ones. The problem is that Hertz did not take into account the adhesion forces which develop at contact. As also reported in Johnson et al. [27], some experimental works by Roberts (1968) [28] and Kendall (1969) [29] demonstrate that at low loads contact areas between two smooth rubber spheres were considerably larger than those predicted by Hertz (see sketch in Figure 4.2). On the contrary they closely fitted the Hertz theory at high loads. These experiments suggested that during contact attractive surface forces act, and although these forces are negligible at high load, they become relevant as load reduces towards zero. Johnson et al. [27] modified the Hertz theory considering the surface force and obtaining

$$a_{JKR}^3 = \frac{R^*}{\left(\frac{4}{3}E^*\right)} \left(F + \frac{3}{2}\Gamma\pi R^* + \sqrt{2\frac{3\Gamma}{2}\pi R^*F + \left(\frac{3}{2}\Gamma\pi R^*\right)^2} \right) \quad (4.5)$$

Γ is the surface energy (also called work of adhesion). The Johnson-Kendall-Roberts (JKR) theory became a milestone in contact/impact of elastic bodies. Several authors (i.e. [26], [30]-[35]) started from Hertz and JKR theories in order to study impact or extend it to elastic-plastic case. The work of Rogers and Reed [30] is one of the most cited and clear. They extended the energy analysis of JKR to elastic-plastic impact of a particle with a (stationary) surface, but their analysis can be readily extended to the case of impact between two spherical bodies.

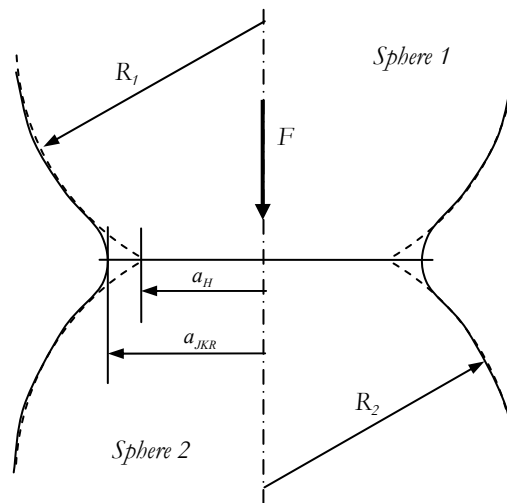


Figure 4.2 – Difference between Hertz and JKR theories.

When two bodies collide first they undergo elastic deformations. A contact surface develops and part of the kinetic energy of the two bodies is stored as elastic energy. An elastic repulsive force rises and the particle gradually decelerates. Contemporarily some irreversible effects take place (i.e. acoustic and elastic waves, internal friction) thus a part of the energy is dissipated. In the case that the stress within the particle exceeds the elastic limit plastic deformations occur, and an additional part of the energy is lost. De-

formations increase until the particle velocity becomes zero. Now elastic energy stored starts to be returned and the impacting particle moves away from that impacted one. Accordingly elastic deformations start to be released. If the initial energy content of particle is high enough to overcome the adhesion energy particle bounces otherwise it sticks.

Elastic and elastic-plastic phase are separately analysed below, and an adhesion criterion is given. It is useful dividing the impact process into two phases: the approach phase starts as soon as the bodies come into contact and finishes when the velocity of the impacting body becomes zero; the restitution phase starts from there and continues until contact is broken.

4.1.1 Elastic impact

For simplicity consider a sphere with mass m_1 and radius R_1 approaching a stationary flat surface with mass $m_2 \gg m_1$ ($R^* \approx R_1$ and $m^* \approx m_1$). Generally speaking the sphere has a kinetic energy Q_K and as it approaches the surface it gains an additional energy due to the attractive force, which develops at the contact surface and depends on the surface itself. While the impact process continues gradually the kinetic energy transforms into elastic energy and the particle decelerates until its velocity becomes zero. Since the contact surface increases as the approach proceeds, the adhesion energy increases too. This produces a pressure distribution on the contact zone which, according to Hertz theory, shows a peak at the centre of the contact zone (Figure 4.3 a).

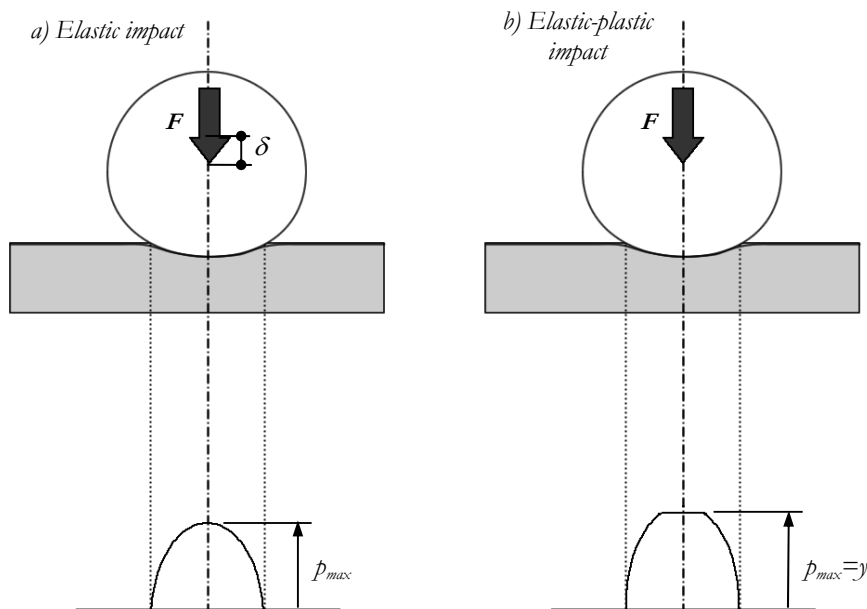


Figure 4.3 – Contact between a sphere and a flat surface. Elastic (left) and elastic-plastic (right) deformations and pressure distribution.

As said before dissipative effects, i.e., acoustic and elastic waves, internal friction, etc., are always present even in an elastic impact. However their contributions are very

small thus they can be neglected considering a pure elastic impact. Total energy Q_E involved in the impact is then

$$Q_E = Q_K + Q_{A,a} \quad (4.6)$$

$Q_{A,a}$ being the adhesion energy developed during the approach phase.

In the restitution phase the stored elastic energy is returned to the sphere being converted again into kinetic energy, and also the adhesion energy $Q_{A,a}$ is returned. However in order to break the contact between the sphere and the surface an additional adhesion energy has to be provided, so the adhesion energy $Q_{A,r}$ developed during the restitution phase differs from that in the approach phase. Rebound/sticking criterion can thus be written

$$\begin{cases} Q_E = Q_K + Q_{A,a} > Q_{A,r} & \text{rebound} \\ Q_E = Q_K + Q_{A,a} \leq Q_{A,r} & \text{sticking} \end{cases} \quad (4.7)$$

If the total stored energy Q_E is greater than $Q_{A,r}$ sphere bounces, otherwise it sticks.

The difference $Q_{A,r} - Q_{A,a}$ is the net adhesion energy and represents the energy needed to break the contact between the two bodies.

4.1.2 Elastic-plastic impact

During the approach phase pressure acting on the contact surface may exceed the elastic limit thus also plastic deformations occur. It is commonly assumed the approximation which considers that pressure distribution in the zone of plastic deformations stays constant (Figure 4.3b and Figure 4.4). With this assumption plastic deformation starts around the centre of the contact surface and is surrounded by an annulus of only elastic deformation.

Due to the irreversible nature of this deformation a part Q_P of the particle energy is lost. In this case equations (4.7) reads

$$\begin{cases} Q_E = Q_K + Q_{A,a} - Q_P > Q_{A,r} & \text{rebound} \\ Q_E = Q_K + Q_{A,a} - Q_P \leq Q_{A,r} & \text{sticking} \end{cases} \quad (4.8)$$

which means that in order to bounce the particle has to have an initial kinetic energy greater than that in the elastic impact.

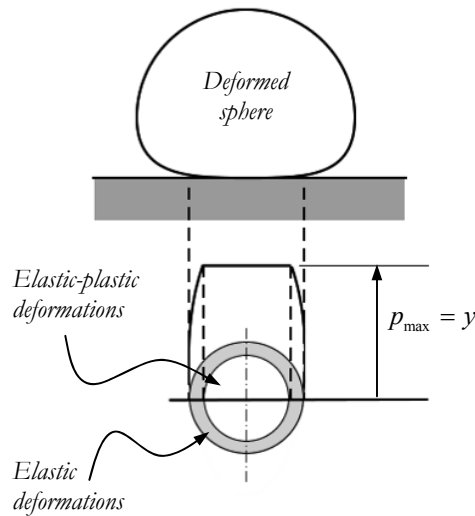


Figure 4.4 – Elastic-plastic impact: zones of elastic and elastic-plastic deformations.

4.1.3 Adhesion energy

In section 4.1.1 it is said that $Q_{A,a}$ and $Q_{A,r}$ are different. To better understand the meaning of the net adhesion energy consider a sphere impacting a stationary flat surface. As reported in [36], [37], and according to JKR theory, Figure 4.5 shows the relation between contact force and relative approach during the contact. As soon as the sphere impacts the surface, that is $\delta = 0$ (Figure 4.5, point A), immediately an attractive force develops due to Van der Waals forces (point B). By virtue of this attractive force the contact area, which theoretically would be a point, grows with δ remaining zero. As the approach phase continues the contact surface becomes larger and accordingly the adhesion energy increases (B-D curve). At a certain point the repulsive elastic force, which rises within the particle as it deforms, equals the attractive one (point C) and then overcomes it reaching a maximum at the end of the approach phase (point D). Accordingly also δ reaches its maximum at this point. The adhesion energy developed so far is $Q_{A,a}$. Now the restitution phase starts. The stored elastic energy is gradually released and converted into kinetic energy, thus particle starts to move away from the surface. Deformation and contact surface decrease as well as the repulsive force, following the same curve as in the approach phase (from point D to B). The adhesion energy is released accordingly to the contact surface reduction. When δ is returned zero, all the adhesion energy developed during the approach phase is released. However the sphere still adheres to the surface and further energy is required to break the contact. Separation occurs at point G in Figure 4.5 ($\delta = -\delta_G$). The adhesion energy $Q_{A,r}$ developed during the restitution phase thus differs from $Q_{A,a}$ by this energy, that is the net adhesion energy (coloured area in figure).

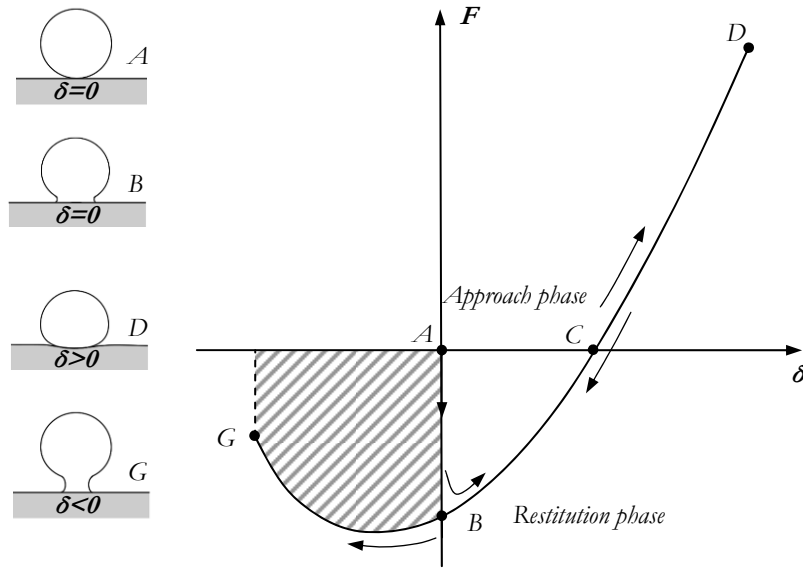


Figure 4.5 – Contact between two bodies: relative approach as a function of contact force.

As reported in [36] this area is computed by integrating the force displacement relation as given in Johnson et al. [27] between zero and $-\delta_G$:

$$Q_{brk} = Q_{A,r} - Q_{A,a} = \int_0^{-\delta_G} F d\delta' = 7.09 \left(\frac{R_c^4 \Gamma^5}{E^{*2}} \right)^{\frac{1}{3}} \quad (4.9)$$

where R_c is the appropriate radius. R_c depends on the kind of impact (i.e., elastic, elastic-plastic), and thus the net adhesion energy varies accordingly. In elastic impact R_c equals R^* while in elastic-plastic one it depends on the deformation of the sphere.

Figure 4.6 shows the net adhesion energy as a function of the contact force, computed assuming a particle which characteristics are summarized in Table 4.1. The brown dashed-dotted line in figure represents the net adhesion energy in case that elastic impact occurs. In this case $R_c \equiv R^*$ thus equation (4.9) provides a constant value. On the other hand, the blue dashed-line represents the net adhesion energy in the case of an elastic-plastic impact, when R_c depends on the plastic deformation of the particle. The part of the curve which falls into the elastic impact zone (left side of the graph) has no physical meaning, hence just the right part of the curve has to be considered. The red solid line represents the (global) net adhesion energy as a function of dimensionless contact force. As shown in figure the net adhesion energy increases with the contact force. This is due to plastic deformation. As well explained by Johnson in [38], after a sphere has undergone plastic deformation, the deformed zone shows a radius $R1'$ larger than the real sphere radius $R1$, as reported in Figure 4.7. As a consequence $R_c = R'^* > R^*$ and then from equation (4.9) the net adhesion energy results larger than in elastic impact.

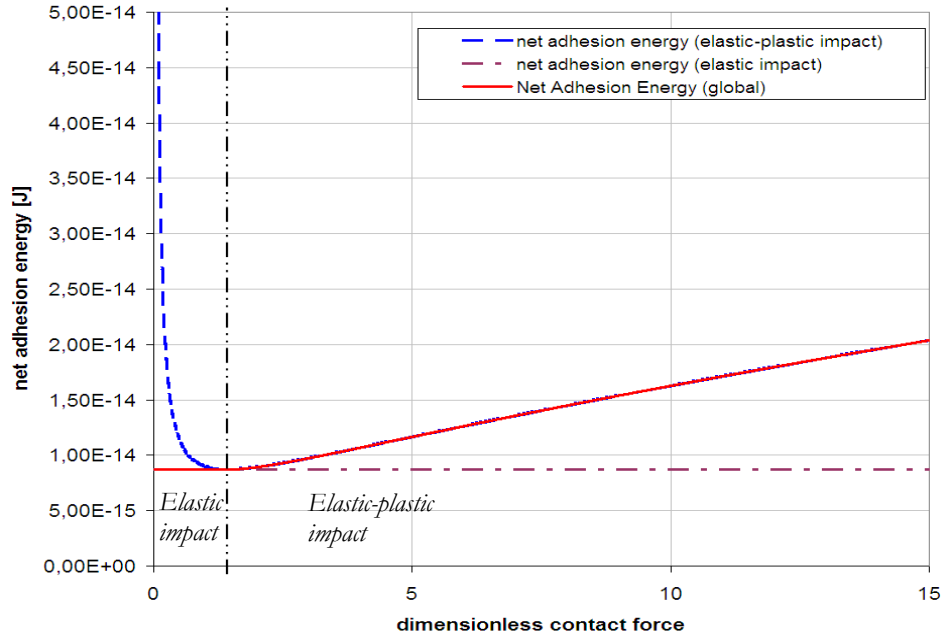


Figure 4.6 – Net adhesion energy as a function of the dimensionless contact force.

| | | |
|--|-------------|----------------------|
| Density (bronze) | 8960 | [kg/m ³] |
| Radius | 1E-6÷100E-6 | [M] |
| Surface energy Γ (bronze-bronze) | 0,12 | [J/m ²] |
| Young modulus E_1 | 1,29E+11 | [N/m ²] |
| Poisson coefficient of particle | 0,33 | [-] |

Table 4.1 – Characteristics of the impacting particle.

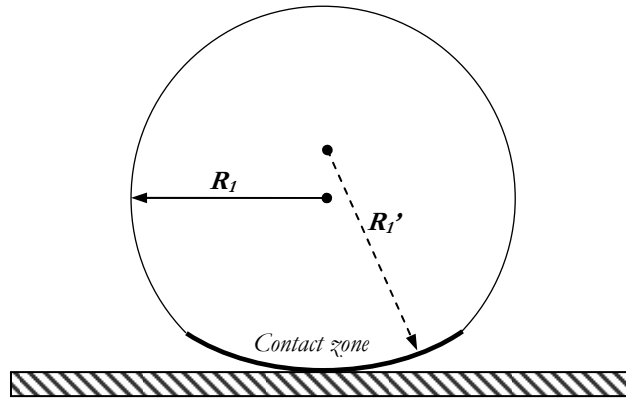


Figure 4.7 – Result of an elastic-plastic impact.

4.2 Coefficient of restitution (COR) and adhesion

Particle impact/rebound/adhesion of a sphere with another sphere or a flat surface can be described by the coefficient of restitution (COR), e , defined as the ratio between the rebound and the incident (normal) velocities.

$$e = \frac{v_{r,n}}{v_{i,n}} \quad (4.10)$$

COR takes into account the dissipation of energy during the impact, thus its expression derives from energy analyses of the impact phase. In case of elastic impact there is no energy dissipation ($e = 1$) and the particle bounces with a velocity equal to that of impact but in the opposite direction. However in real impacts energy dissipations always take place (i.e. wave propagation, plastic deformations, friction, adhesion, etc.) hence usually COR is lower than unity.

COR can also be used to predict whether an impacting body sticks or bounces. Consider the normal impact of a particle, having velocity $v_{i,n}$ with a stationary flat surface (or sphere), and rebounding with a velocity $v_{r,n}$. During the impact particle undergoes a variation of kinetic energy ΔQ , given by

$$\Delta Q = \frac{1}{2} m^* v_{r,n}^2 - \frac{1}{2} m^* v_{i,n}^2 \quad (4.11)$$

which equals the energy loss due to adhesion, plastic deformations, and other irreversible effects. Then it writes

$$\Delta Q = \frac{1}{2} m^* (1 - e^2) v_{i,n}^2 \quad (4.12)$$

and COR becomes

$$e^2 = 1 - \frac{\Delta Q}{\frac{1}{2} m^* v_{i,n}^2} \quad (4.13)$$

Since ΔQ represent the energy loss in the impact assuming that sphere bounces with a velocity $v_{r,n}$, it implies $e > 0$. When $v_{r,n} = 0$, that is the sphere sticks to the surface, the initial kinetic energy of the particle is just equal to ΔQ , thus $e = 0$. In this case it is possible to compute the so called *sticking velocity*, that is the maximum velocity under which impacting body adheres to the impacted one.

Note that COR might mathematically assume negative values: if the initial kinetic energy of the particle is lower than ΔQ from (4.13) e becomes negative. This means that particle energy is not sufficient to break the contact thus it sticks to the surface.

In the following of this section some models for COR evaluation are reported.

4.2.1 Van Beek model

Starting from the energy analysis given in [30] van Beek [36] provides an expression for ΔQ (4.13).

Consider again two impacting spheres, with radius R_1 and R_2 , and mass m_1 and m_2 respectively. Consider also that sphere 2 is stationary, therefore velocities and energy are both referred to sphere 1. For elastic impact the only energy loss is that required to break the contact ($Q_{A,r} - Q_{A,a}$), which is given by (4.9) [38]:

$$\Delta Q = Q_{A,r} - Q_{A,a} = 7.09 \left(\frac{R_c^4 \Gamma^5}{E^*{}^2} \right)^{\frac{1}{3}} \quad (4.14)$$

The adhesion energy Γ can be evaluated following Fowkes (1968) as reported in Rogers and Reed [30]. The interaction energy in an interface is given by the geometric mean of the dispersive energy components. Hence the adhesive energy of the interface, also called *work of adhesion*, is

$$\Gamma = 2\sqrt{\gamma_1 \gamma_2} \quad (4.15)$$

with γ_1 and γ_2 the surface free energy of the two bodies.

In elastic-plastic impacts besides the net adhesion energy ($Q_{A,r} - Q_{A,a}$), energy loss ΔQ also comprises energy dissipated in plastic deformation Q_P :

$$\Delta Q = Q_P + (Q_{A,r} - Q_{A,a}) \quad (4.16)$$

where both Q_P and $Q_{A,a}$ depends on the contact load F acting on particle. Therefore the COR writes:

$$e^2 = 1 - \frac{Q_P + (Q_{A,r} - Q_{A,a})}{\frac{1}{2}mv_{i,n}^2} \quad (4.17)$$

The net adhesion energy ($Q_{A,r} - Q_{A,a}$) is evaluated again using (4.14) but now $R_c = R^*$ because of plastic deformations. Applying the Hertz theory for the conditions at the end of the approach phase, it results

$$R_c = \frac{\frac{4}{3}E^*r_T^3}{F} \quad (4.18)$$

with r_T the radius of total deformed area. This radius is given by the contribution of two terms as in (4.19): the radius of elastically deformed area r_{EL} , and the radius of plastically deformed one, which has to be computed.

$$r_T^2 = r_{EL}^2 + r_P^2 \quad (4.19)$$

Plastic deformations develop around the centre of the contact area, being surrounded by an annulus of only elastic deformations (Figure 4.4). Following Bitter [39], it is assumed that plastic deformations take place in only one of the two bodies in contact (the softer one), whilst elastic deformation occur in both of them. Also assuming that no work-hardening effects occur, the elastic limit remains constant during plastic phase. If the total area of deformation is small compared to the cross-section of the sphere, it can be approximated by

$$\pi r_T^2 \approx 2\pi R^* (H + h_{EL}) \quad (4.20)$$

h_{EL} is the relative approach at the limiting elastic case, that is when the contact load equals the elastic limit F_{EL} ; $H = \delta - h_{EL}$ is the remnant deformation.

Accepting the Bitter assumptions and the approximation in (4.20), it is demonstrated that the area of only elastic deformation remains constant during plastic phase and equal to the area of elastic deformation in limiting case (radius r_{EL}). r_{EL} is given by [31]

$$r_{EL} = \frac{\pi R^*}{2E^*} y \quad (4.21)$$

y is the elastic yield limit. Radius of plastically deformed zone r_P depends on the load and is given by

$$r_P^2 = \frac{F - F_{EL}}{\pi y} \quad (4.22)$$

Thus knowing F , from equations (4.22), (4.21) and (4.19), the contact radius R_c can be computed.

As far as the energy loss in plastic deformations Q_P is concerned, it is computed by integrating the contact load F between 0 and H (the approach distance during plastic phase), and can be approximated by:

$$Q_P = \int_0^H F dH' \approx \frac{(F - F_{EL})^2}{4\pi R^* y} \quad (4.23)$$

In order to solve equation (4.16) and compute the COR by (4.17), as well as to compute R_c (4.18), contact load F has to be evaluated. To this aim the energy balance at the end of the approach phase can be used. At the end of the approach phase, particle velocity is zero then its kinetic energy, added with the adhesion energy developed during the approach phase $Q_{A,a}(F)$, is splitted into a stored elastic energy in the only elastic deformations zone Q_{EL} , a stored elastic energy in the plastic deformations zone $Q_{PE}(F)$, and an energy loss for plastic deformation Q_{PE} :

$$Q_K + Q_{A,a}(F) = Q_{EL} + Q_{PE}(F) + Q_P(F) \quad (4.24)$$

Once the expression of each term is known, equation (4.24) can be solved to find the contact load, thus equations (4.16) and (4.17) can be computed.

In elastic-plastic impact elastic energy is stored in the annulus Q_{EL} of only elastic deformation, but also in the zone of plastic deformation Q_{PE} . These elastic energy are computed following Bitter [39] again. Besides the aforementioned assumptions, the author assumes also that the pressure distribution remains the same; by this assumption it results that the elastic energy stored in the annulus is constant. Therefore Q_{EL} can be evaluated by integrating the contact load $F = F_{EL}$ between 0 and δ_{EL} [31]:

$$Q_{EL} = \int_0^{\delta_{EL}} F_{EL} d\delta' = \frac{2}{5} \frac{F_{EL}^{5/3}}{\left(\frac{4}{3} E^*\right)^{2/3} R^{1/3}} \quad (4.25)$$

then assuming from the Hertz theory

$$F_{EL} = \left(\frac{2}{3} \pi\right)^3 \frac{R^{*2}}{\left(\frac{4}{3} E^*\right)^2} y^3 \quad (4.26)$$

(4.25) reads

$$Q_{EL} = \frac{2}{5} \left(\frac{2}{3}\right)^5 \frac{\pi^5 R^{*3}}{\left(\frac{4}{3} E^*\right)^4} y^5 \quad (4.27)$$

which results independent from the contact load.

The elastic energy stored in the plastically deformed area is expressed by

$$Q_{PE} = \frac{1}{2} h_{EL} (F - F_{EL}) \quad (4.28)$$

In the left side of equation (4.24) the only energy unknown is now $Q_{A,a}$. Its expression for elastic-plastic impact is a function of the contact load:

$$Q_{A,a} = \Gamma \pi \left(r_{EL}^2 + \frac{F - F_{EL}}{\pi y} \right) \quad (4.29)$$

Now that all term of (4.24) are known it can be solved to find the load F . Once that F is known, equations (4.18) to (4.23) can be solved and finally COR is evaluated by (4.17).

4.2.2 Thornton and Ning model

Following Hertz and JKR theories Thornton and co-workers [37], [40] proposed a model which is a bit different from the van Beek one.

The authors first study the impact/rebound of non adhesive spheres obtaining the following expression for COR:

$$e = \left(\frac{6\sqrt{3}}{5} \right)^{1/2} \left[1 - \frac{1}{6} \left(\frac{v_{y,n}}{v_{i,n}} \right)^2 \right]^{1/2} \left[\frac{\left(\frac{v_{y,n}}{v_{i,n}} \right)}{\left(\frac{v_{y,n}}{v_{i,n}} \right) + 2\sqrt{\frac{6}{5} - \frac{1}{5} \left(\frac{v_{y,n}}{v_{i,n}} \right)^2}} \right]^{1/4} \quad (4.30)$$

$v_{y,n}$ is the yield velocity, that is the velocity below which impact is assumed to be elastic. $v_{y,n}$ for a sphere impacting a flat surface assumes the form

$$v_{y,n} = \left(\frac{\pi}{2E^*} \right)^2 \left(\frac{2}{5\rho_p} \right)^{1/2} y^{5/2} \quad (4.31)$$

also obtained by van Beek [36].

For adhesive spheres, considering an elastic impact and neglecting all the energy losses but the work needed to break the contact, energy balance reads [38]:

$$\frac{1}{2} m^* v_{i,n}^2 - \frac{1}{2} m^* v_{r,n}^2 = 7.09 \left(\frac{\Gamma^5 R^{*4}}{E^{*2}} \right)^{1/3} \quad (4.32)$$

Imposing $v_{r,n} = 0$, that is the impacting body sticks to the stationary one, impact velocity equals the sticking velocity, which can be written as

$$v_{s,n} = \left(\frac{14.18}{m^*} \right)^{1/2} \left(\frac{\Gamma^5 R^{*4}}{E^{*2}} \right)^{1/6} \quad (4.33)$$

If a sphere impacts a flat surface it results $R^* = R$, $m^* = m = (4/3)\pi R^3 \rho_p$, then (4.33) reads

$$v_{s,n} = 1.84 \left[\frac{(\Gamma/R)^5}{\rho^3 E^{*2}} \right]^{1/6} \quad (4.34)$$

If $v_{i,n} = v_{s,n}$ then bounce occurs and (4.32) rewrites

$$1 - \left(\frac{v_{r,n}}{v_{i,n}} \right)^2 = \left(\frac{v_{s,n}}{v_{i,n}} \right)^2 \quad (4.35)$$

From which COR is defined

$$e = \left[1 - \left(\frac{v_{s,n}}{v_{i,n}} \right)^2 \right]^{1/2} \quad (4.36)$$

In elastic-plastic impact Thornton [40] referred to the work of Hardy et al. [41] who showed that pressure distribution on the contact surface changes from the elastic elliptical shape to an essentially uniform distribution as the load increases. Thus the assumption of a plastically deformed zone surrounded by an annulus of only elastically deformed zone is not strictly correct.

As Thornton and Ning say, equations which describe the behaviour of elastic-plastic sphere are very complicate and an analytical solution for them is not available. However an analytical solution is possible assuming that the work loss due to plastic deformation and the work loss due to break the contact are additive. In this case it results:

$$(1 - e^2) = (1 - e_p^2) + (1 - e_A^2) \quad (4.37)$$

e_p is the COR due to plastic deformation, and e_A is the COR due to adhesive rupture and is given by (4.36). e_p instead is given by (4.30). Substituting (4.36) and (4.30) into (4.37) leads to

$$e = 0 \quad \text{for } v_{i,n} \leq v_{s,n}$$

$$e = \left[1 - \left(\frac{v_{s,n}}{v_{i,n}} \right)^2 \right]^{1/2} \quad \text{for } v_{s,n} < v_{i,n} \leq v_{y,n}$$

$$e = \left\{ \left(\frac{6\sqrt{3}}{5} \right) \left[1 - \frac{1}{6} \left(\frac{v_{y,n}}{v_{i,n}} \right)^2 \right] \left[\frac{\left(\frac{v_{y,n}}{v_{i,n}} \right)}{\left(\frac{v_{y,n}}{v_{i,n}} \right) + 2\sqrt{\frac{6}{5} - \frac{1}{5} \left(\frac{v_{y,n}}{v_{i,n}} \right)^2}} \right]^{1/2} - \left(\frac{v_{s,n}}{v_{i,n}} \right)^2 \right\}^{1/2} \quad (4.38)$$

$$\text{for } v_{i,n} > v_{y,n}$$

4.2.3 Feng et al. model

Feng et al. [42] developed a Finite Element model to simulate the normal impact of adhesive microparticles with a rigid surface, and compared results from numerical simulation with those from an analytical solution briefly described below.

The authors assume that $Q_{A,a}$ is much smaller than $Q_{A,r}$ thus they neglect the contribution of the first one. Assuming this, the incident kinetic energy is completely transformed into elastic energy during impact

$$Q_E = Q_K = \frac{1}{2} m v_{i,n}^2 \quad (4.39)$$

Note that in this case, since the authors consider the impact of a particle on a flat surface, in (4.39) m is the mass of the particle. According to Hertz theory contact radius a is related to Q_E by

$$Q_E = Q_K = \frac{2}{5} \frac{K}{R^2} a^5 \quad (4.40)$$

where K is an elastic constant defined as

$$K = \frac{4}{3} \frac{E}{(1-\nu^2)} \quad (4.41)$$

E and ν are respectively the Young modulus and Poisson coefficient of particle. Substituting (4.41) into (4.40) and recalling that particle mass is $m = (4/3)\pi R^3 \rho_p$, it writes

$$a = \left(\frac{5}{3} \frac{\pi \rho_p}{K} v_{i,n}^2 R^5 \right)^{1/5} \quad (4.42)$$

Considering that the work of adhesion is approximately equal to $\pi a^2 \Gamma$, the conservation of energy requires that

$$\frac{1}{2} m v_{i,n}^2 = \frac{1}{2} m v_{r,n}^2 + \pi a^2 \Gamma \quad (4.43)$$

This equation is formally identical to (4.32) in Thornton and Ning's model, but the way of computing the adhesion energy is different. From (4.43) assuming $v_{r,n} = 0$ the sticking velocity can be calculated:

$$v_{s,n} = \frac{1}{\sqrt{\rho_p}} \left(\frac{5}{3} \frac{\pi}{K} \right)^{1/3} \left(\frac{3}{2} \frac{\Gamma}{R} \right)^{5/6} \quad (4.44)$$

If $v_{i,n} > v_{s,n}$ than the COR is obtained by (4.43)

$$e = \sqrt{1 - \left(\frac{5\pi}{3K}\right)^{2/5} \frac{3\Gamma}{2Rv_{i,n}^{6/5}\rho_p^{3/5}}} \quad (4.45)$$

Feng et al. actually do not propose an adhesion model but use the above sketched one as analytical solution to compare with their FEM simulation, that is implicitly they assume this model as true.

4.2.4 Comparison of models

Although the three models presented above are all derived assuming the Hertz and JKR theories, results are not exactly the same. In order to compare the van Beek, Thornton and Ning, and Feng models, the sticking velocity and COR are used.

Consider the impact between a sphere with radius R and a flat surface. Van Beek does not explicitly calculate the sticking velocity $v_{s,n}^{vB}$, but it can be easily done through equations (4.13) and (4.14) imposing $e = 0$ so obtaining equation (4.46). Sticking velocity in Thornton and Ning's model, $v_{s,n}^{TN}$, given in (4.34) is rearranged as in equation (4.47) to make the comparison easier. It results $v_{s,n}^{TN} \equiv v_{s,n}^{vB}$ because the authors use the same expression for net adhesion energy, that is the one given by Johnson [38].

Sticking velocity in Feng's model $v_{s,n}^{FA}$ is given by equation (4.44). Substituting (4.41) into (4.44) and rearranging, $v_{s,n}^{FA}$ rewrites as in equation (4.48).

$$v_{s,n}^{vB} = \frac{1.84}{\sqrt{\rho}} \left(\frac{1}{E^*}\right)^{1/3} \left(\frac{\Gamma}{R}\right)^{5/6} \quad (4.46)$$

$$v_{s,n}^{TN} = \frac{1.84}{\sqrt{\rho}} \left(\frac{1}{E^*}\right)^{1/3} \left(\frac{\Gamma}{R}\right)^{5/6} \quad (4.47)$$

$$v_{s,n}^{FA} = \frac{2.21}{\sqrt{\rho}} \left(\frac{1-v^2}{E}\right)^{1/3} \left(\frac{\Gamma}{R}\right)^{5/6} \quad (4.48)$$

Note that equations (4.46) and (4.47) contains E^* , as defined in (4.3)

$$\frac{1}{E^*} = \frac{1-v_1^2}{E_1} + \frac{1-v_2^2}{E_2} \quad (4.49)$$

whereas equation (4.48) contain E and v . This is due to the fact that Feng et al. [42] study the impact of a spherical particle with a flat and rigid surface, whereas both van Beek [36] and Thornton and Ning [37] assume that elastic deformation can occur in

both the bodies. Considering in (4.49) $E_2 = \infty$ (second body is rigid), and assuming $E_1 = E$ and $v_1 = v$, it rewrites

$$\frac{1}{E^*} = \frac{1-v^2}{E} \quad (4.50)$$

thus comparison can be done on equal terms.

Considering particle with characteristics reported in Table 4.1, curves of the different sticking velocity as a function of particle radius are shown in Figure 4.8. As expected considering that equations (4.46)-(4.48) are exactly the same, apart from value of constants (1.81 in van Beek and Thornton & Ning, and 2.21 in Feng et al.), the trend is the same but sticking velocity in Feng's model is about 20% greater than the others. Constants are different because the authors evaluate the net adhesion energy in a different way: van Beek and Thornton & Ning use the approach given in Johnson [27] (equation (4.9)); on the contrary assuming that the influence of the adhesion energy during the approach phase is negligible, Feng approximates the net adhesion energy by $\pi a^2 \Gamma$ which is quite different from equation (4.9).

As direct consequence of the difference in the sticking velocity, COR computed by Feng et al. is different from that computed by both van Beek and Thornton & Ning. Figure 4.9 shows that for a given particle radius, since the sticking velocity is higher in Feng et al. than in the other models, the latter ones predict that rebound starts at a lower impact velocity and COR is always smaller. For the same reason also in Figure 4.10 COR is smaller in Feng et al. for a given particle radius than in the other models.

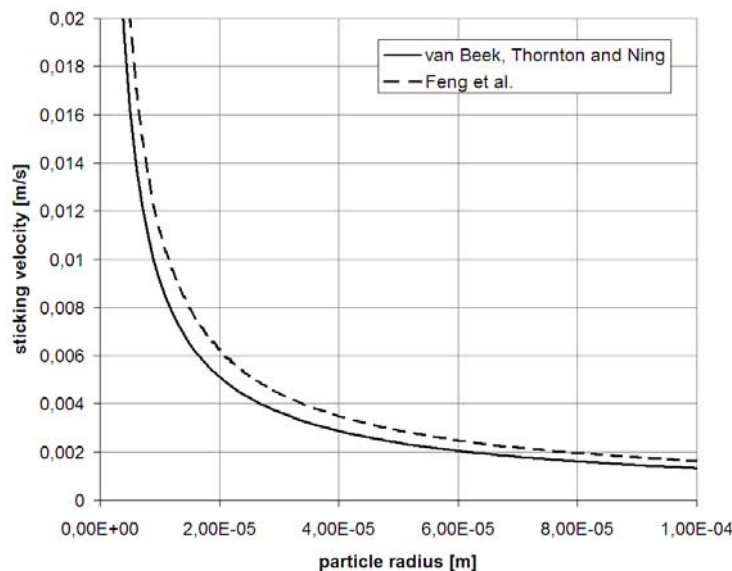


Figure 4.8 – Sticking velocity as a function of particle radius.

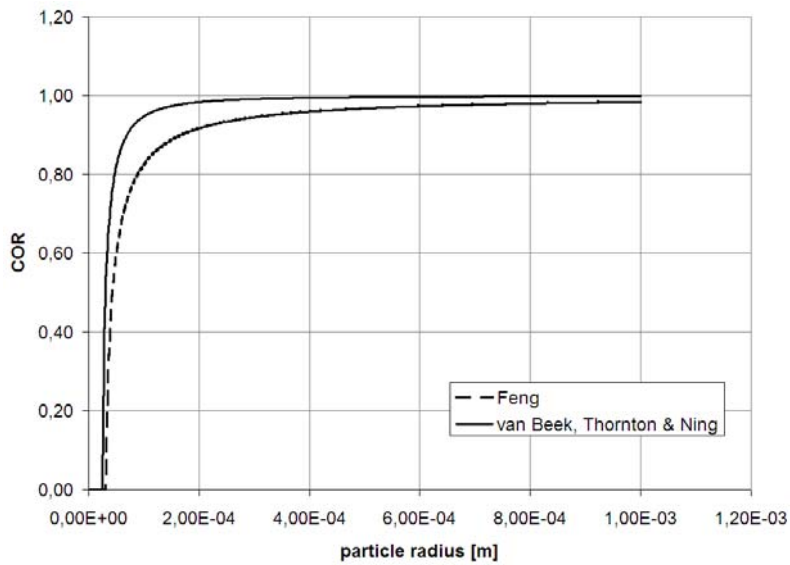


Figure 4.9 – COR as a function of impact velocity in the analysed models.

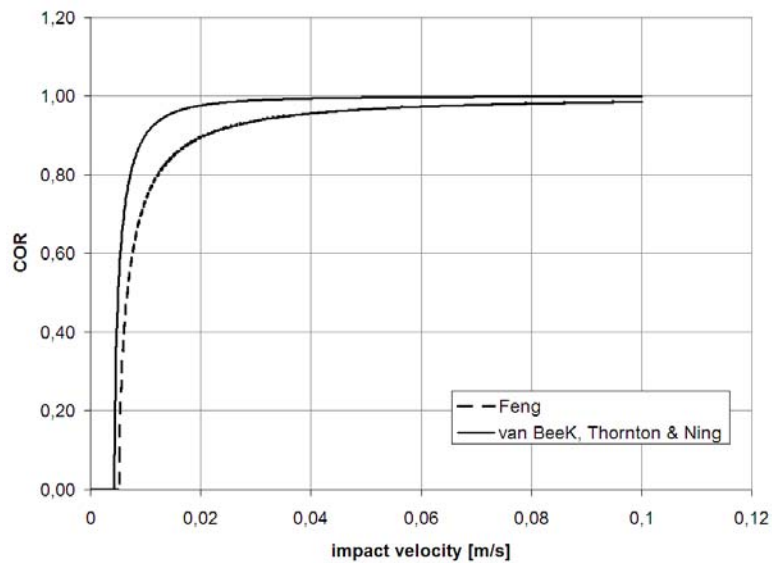


Figure 4.10 – COR as a function of particle radius in the analysed models.

4.3 Oblique impact

Studies on particle impact are most focused on normal impact. Pioneers in oblique impact mechanics studies in 50's-70's are, i.e., Mindlin and Deresiewicz [43], Maw et al. [34], Savkoor and Briggs [44], but most of the studies on this subject are more recent

(i.e. [26], [35], [45]-[48]). The majority is focused on the calculation of tangential component of rebound velocity and does not take into account adhesion in oblique contact, which is still computed only considering the normal impact velocity component. This means that adhesion and friction is uncoupled, and models developed so far follow this approach. However there are some experimental evidences that this is not the case. Broom in 1979 [49] used the impact of glass spheres onto aluminium substrate to study the adhesion of particles in filters. He found that the sticking velocity was smaller for oblique impact than that for normal impact. Similar results are obtained by Li et al. [50] during their experimental and numerical study of oblique impact. They developed a numerical model but then they tested it using an impact velocity greater than the sticking velocity (computed for normal impact), thus the model is not verified for adhesion problems. Brach and Dunn in 1995 [51] in their study of macrodynamics of microparticles proposed two models for oblique impact, but in both of them adhesion is not clearly treated and however models are focused on the computation of normal and tangential CORs. The same authors few years after [52] proposed a simplified empirical model to simulate oblique impacts, based on the use of some constants derived from experiments. However as they say in their own work, the question of capture for oblique impact is not directly analysed and need further investigations. Van Beek [36] studies oblique impact using the two-body collision model which computes normal and tangential CORs but uses only the normal one to evaluate the adhesion condition.

Therefore at the moment, how the impact angle affects adhesion and rebound is not completely clear. In the following section an analysis of this effect is provided aiming at better understanding the physics and choosing/developing an appropriate model.

4.3.1 Effect of the impact angle

Savkoor and Briggs [44] studied the effect of a tangential force acting together with a normal one on the contact between a particle and a plane. They pointed out that the presence of a tangential force results in a reduction of the contact radius. Following the JKR theory, the contact radius can be expressed as in equation (4.14). In the following indicate with N the normal force, and with T the tangential one (Figure 4.11). Adopting this nomenclature, equation (4.14) rewrites:

$$a_{JKR}^3 = \frac{R^*}{\left(\frac{4}{3}E^*\right)} N_{1,JKR} = \frac{R^*}{\left(\frac{4}{3}E^*\right)} \left(N + N_0 + \sqrt{2N_0N + N_0^2} \right) \quad (4.51)$$

$N_{1,JKR} = N + N_0 + \sqrt{2N_0N + N_0^2}$ is the equivalent Hertzian force, that is the force which in the Hertz theory (no adhesion effect) would produce the same contact radius as N . G^* is the effective shear modulus of the particle-surface pair:

$$\frac{1}{G^*} = \frac{2-\nu_1}{G_1} + \frac{2-\nu_2}{G_2} \quad (4.52)$$

G_1 and G_2 are the shear modulus of the two bodies. $N_0 = (3/2)\pi\Gamma R^*$ is the pull-off force [27].

Introducing a tangential force $T = Ntg\theta$ Savkoor and Briggs [44] demonstrated that the contact radius becomes

$$a_{SB}^3 = \frac{R^*}{\left(\frac{4}{3}E^*\right)} N_{1,SB} = \frac{R^*}{\left(\frac{4}{3}E^*\right)} \left(N + N_0 + \sqrt{2N_0N + N_0^2 - \frac{E^*}{4G^*}T^2} \right) \quad (4.53)$$

Where, accordingly, $N_{1,SB} = \left(N + N_0 + \sqrt{2N_0N + N_0^2 - \left(\frac{E^*}{4G^*}\right)T^2} \right)$ is the equivalent Hertzian force.

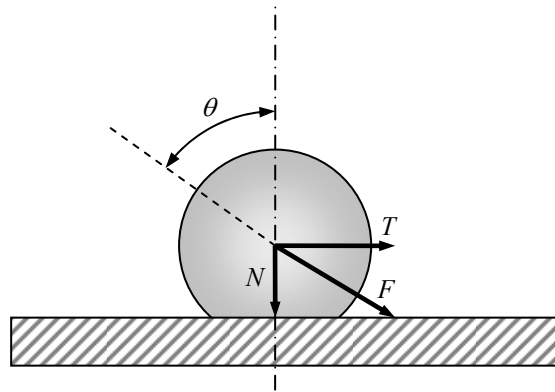


Figure 4.11 – Forces acting in oblique impact.

Equations (4.51) and (4.53) can be used to see the differences between normal and oblique impact. Dividing both the Hertzian forces by N_0 , dimensionless equivalent forces are:

$$N_{1,JKR}^* = N^* + 1 + \sqrt{2N^* + 1} \quad (4.54)$$

$$N_{1,SB}^* = \left(N^* + 1 + \sqrt{2N^* + 1 - \frac{E^*}{4G^*} N^{*2} tg\theta} \right) \quad (4.55)$$

| | |
|----------------------------|--------------------------------|
| r_p | 25.0 μm |
| ρ | 8960 kg/m^3 |
| Young modulus, E | 1,29E+11 N/m^2 |
| Poisson coefficient, ν | 3,30E-01 - |
| Pull-off force, N_0 | 1,41E-05 N |
| Surface energy, Γ | 0,12 J/m^2 |

Table 4.2 – Particle data used in the analysis.

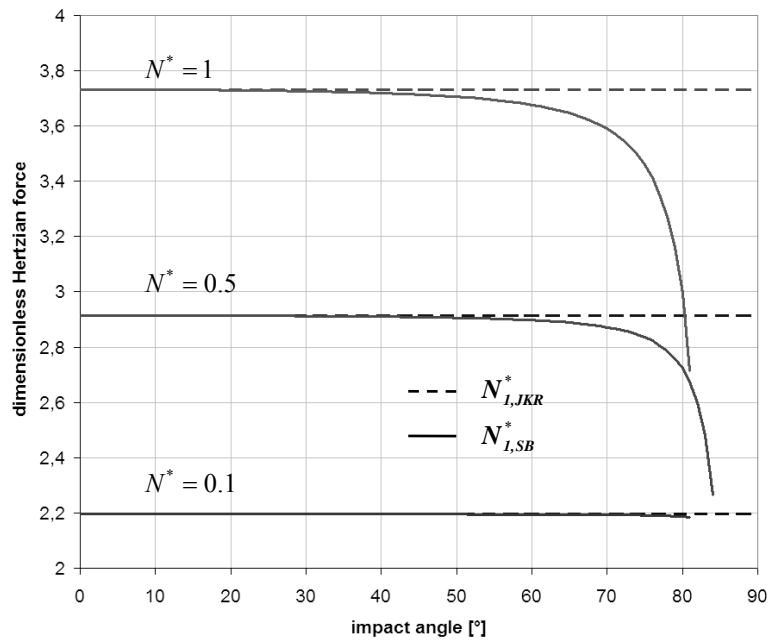


Figure 4.12 – Dimensionless equivalent Hertzian forces, at different values of N^* , as a function of the impact angle.

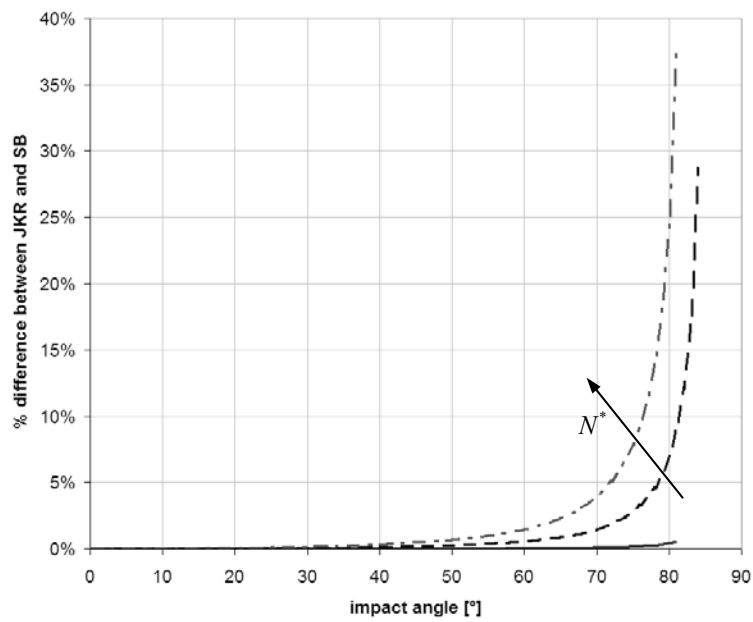


Figure 4.13 – % difference between $N_{I,JKR}^*$ and $N_{I,SB}^*$.

Assuming three different value of N^* (i.e., 0.1, 0.5 and 1.0), assuming also particle characteristics given in Table 4.2, and varying impact angle from 0° (normal impact) to 90° (tangential impact), values of $N_{I,JKR}^*$ and $N_{I,SB}^*$ are plotted in Figure 4.14. $N_{I,JKR}^*$ does not take into account the tangential force, while $N_{I,SB}^*$ does. Figure 4.15 shows that the effect of impact angle is more evident at higher loads. Thought this, considering also Figure 4.13, which shows the difference between $N_{I,JKR}^*$ and $N_{I,SB}^*$, it is pointed out that the tangential force is not so important (difference $< 5\%$) until impact angle is smaller than $60-70^\circ$.

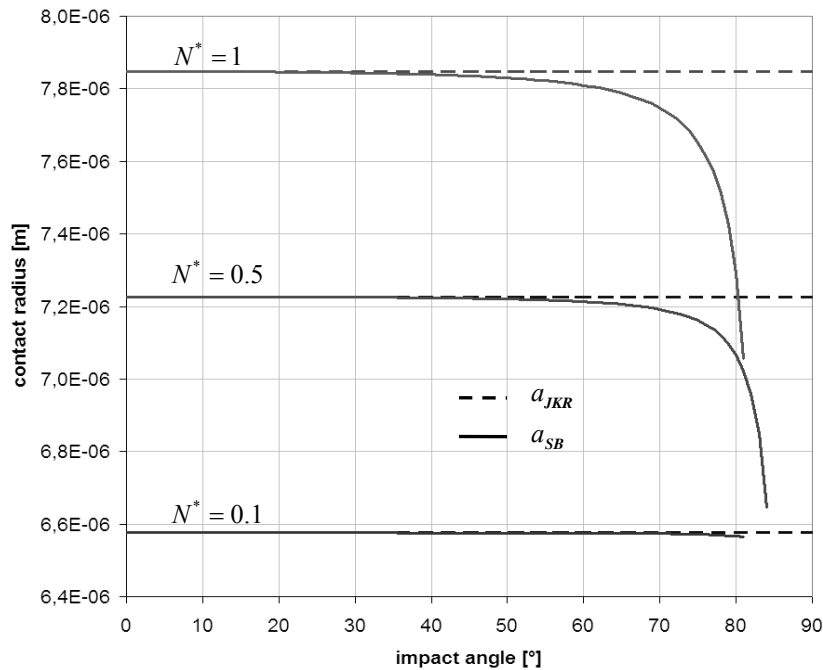


Figure 4.14 – Contact radius, at different values of N^* , as a function of the impact angle.

The contact radius shows similar trends as illustrated in Figure 4.14 and Figure 4.15, but now it can be seen that the effect of a tangential force is even less evident in comparison with the JKR force. As a matter of fact Figure 4.15 shows that the difference between the contact radius computed as JKR or SB is less than 2% for impact angles up to 70° .

From this analysis is evident that the impact angle, which indeed affects the impact/rebound phenomenon, is negligible for angles up to about 70° . After this value its importance increases rapidly. On the basis of this analysis in this work the oblique impact model proposed by Konstandopoulos [48] is adopted. Konstandopoulos introduces a threshold angle above which impacting particle does not stick, even if the COR satisfies the adhesion condition.

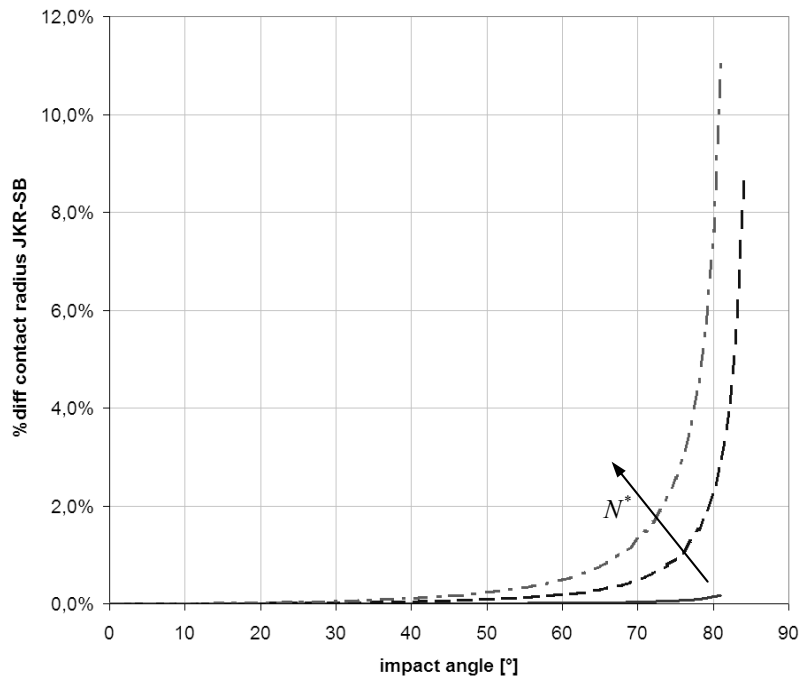


Figure 4.15 – % difference between JKR and SB contact radius.

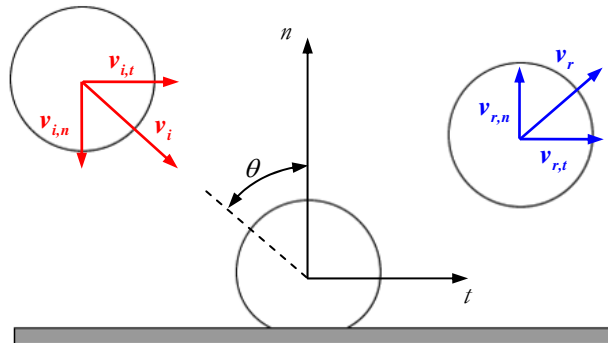


Figure 4.16 – Configuration and coordinate system for oblique impact.

4.3.2 Konstandopoulos's model

Figure 4.16 illustrates the configuration and coordinate system in oblique impact. Konstandopoulos [48] bases his model on the concept of critical angle of incidence θ_{cr} , similar to that of critical (or sticking) velocity used in normal impacts. A critical angle of incidence was found by Wessel and Righi [53] in their study about inertia dominated

impact and deposition on a cylinder, but any adhesion force was considered. They found that there is a critical angle, function of impact velocity, impact angle, particle size, and other quantities, which delimitates the zone of the cylinder where particles deposit. In Konstandopoulos θ_{cr} has the same meaning: it is the impact angle beyond which a particle cannot stick on a surface, even though its normal impact velocity satisfies the sticking criterion $v_{i,n} > v_{s,n}$. The sticking condition in oblique adhesive impact then is:

$$\frac{v_{i,t}}{v_{i,n}} = \tan \theta \leq \tan \theta_{cr} \quad (4.56)$$

The author indicated two peeling criteria and both of them are connected to a minimum tangential force to make an adhered particle slide. It occurs when the contact force in normal direction equals the so-called ‘pull-off’ force F_{ad} as defined in the JKR theory. Therefore tangential force T writes:

$$T \geq f_s^* F_{ad} = f_s^* 3\pi R\gamma \quad (4.57)$$

f_s^* is the effective friction coefficient which can be equal to either f_s (the friction coefficient) or $(1/3)^{3/2} f_s$ depending on what peeling criterion is chosen; γ is the surface free energy of the particle (Konstandopoulos considers the surface as a rigid body). Tangential force can be expressed through the tangential stiffness κ_t :

$$T = \kappa_t (v_{i,t} \Delta t) \geq f_s^* 3\pi R\gamma \quad (4.58)$$

The tangential impact energy at the moment of contact break is given by

$$E_t = \frac{1}{2} \kappa_t (v_{i,t} \Delta t)^2 = \frac{1}{2} \frac{f_s^{*2} F_{ad}^2}{\kappa_t} \quad (4.59)$$

The adhesion energy which has to be overcome at the moment of contact break can be expressed in terms of Γ :

$$E_n = \pi a^2 \Gamma \quad (4.60)$$

where a is the contact radius when the contact breaks. Assuming $\kappa_t \approx 8G^*$, where G^* is the effective shear modulus of the particle-surface pair, it results:

$$\frac{E_t}{E_n} = \frac{9}{64} \pi \frac{f_s^{*2} R^2 \Gamma}{G^* a^3} \quad (4.61)$$

The contact radius at equilibrium a_0 , that is when the force acting on the particle is zero, writes:

$$a_0 = \frac{18\pi R^2 \Gamma}{E^*} \quad (4.62)$$

The contact radius a at the moment of contact break can be expressed as a fraction β of a_0 i.e., $a = \beta a_0$, then substituting in (4.61) and rearranging

$$\frac{E_t}{E_n} = \left(\frac{v_{i,t}}{v_{i,n}} \right)^2 = \frac{f_s^{*2}}{32\beta^3} \frac{E^*}{G^*} \quad (4.63)$$

which leads to

$$\frac{v_{i,t}}{v_{i,n}} = \text{tg}\theta_{cr} = \frac{f_s^*}{(32\beta^3)^{1/2}} \sqrt{\frac{E^*}{G^*}} \quad (4.64)$$

Assuming the second body (the surface) as rigid (i.e, $E_2 = \infty$, $G_2 = \infty$), $E_l = E$ and $G_l = G$, the ration E^*/G^* in (4.64) writes

$$\frac{E^*}{G^*} = \frac{E}{1-\nu^2} \frac{2-\nu}{G} \quad (4.65)$$

Moreover being $G = E/2(1+\nu)$, substituting (4.65) into (4.64) and rearranging, it rewrites

$$\frac{v_{i,t}}{v_{i,n}} = \text{tg}\theta_{cr} = \frac{f_s^*}{(32\beta^3)^{1/2}} \sqrt{\frac{2(2-\nu)}{(1-\nu)}} \quad (4.66)$$

Then if the ratio between tangential and normal components of the impacting velocity results

$$\frac{v_{i,t}}{v_{i,n}} \geq \frac{f_s^*}{(32\beta^3)^{1/2}} \sqrt{\frac{2(2-\nu)}{(1-\nu)}} \quad (4.67)$$

particle does not stick even if the condition $v_{i,n} < v_{s,n}$ is satisfied.

This model does not simulate adhesion in oblique impacts, because it does not give an expression of COR dependent on the impact angle. It just try to model the existence of a limiting angle beyond which particle does not stick anyhow. Therefore this model is not an alternative to those analysed for normal impacts, it has to be added to them.

4.4 Algorithm for adhesion/rebound of particles

Particle tracking algorithm tracks the position of a given particle as a function of time. Once a particle impacts a domain wall, control passes to algorithm for adhesion/rebound, which is sketched in Figure 4.17.

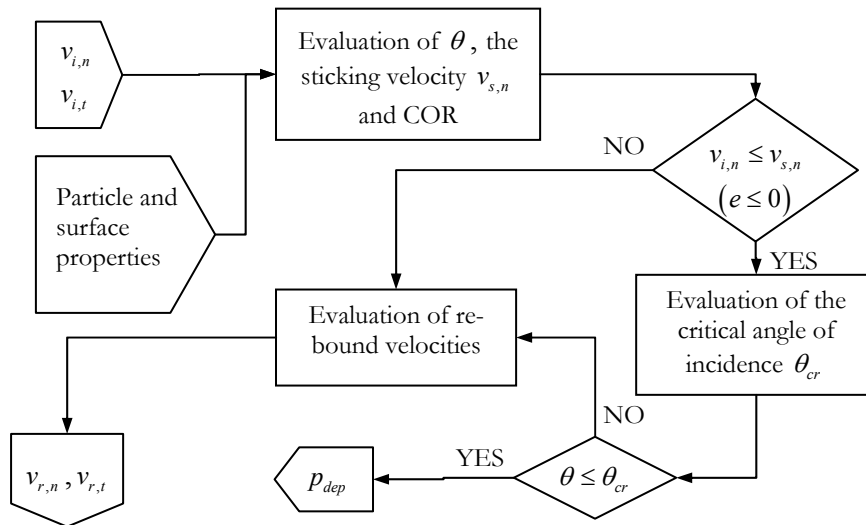


Figure 4.17 – Sketch of the algorithm for adhesion /rebound of particles.

Material properties of impacting particle and impacted surface are given as input to the subroutine, as well as the impacting velocity. First of all impact angle, normal impact COR, and sticking velocity are computed depending on the model assumed. Then condition $v_{i,n} \leq v_{s,n}$ (or $e \leq 0$) is evaluated. If this relation is not satisfied then rebound velocity are calculated and particle continues its path. On the contrary the critical angle of incidence is computed and then condition $\theta \leq \theta_{cr}$ is evaluated: if it is satisfied then particle adheres to surface and is removed from particle tracking computation, otherwise rebound velocity is computed and particle continues its path.

4.5 Temperature effect on ash sticking propensity

Particle entrained by the flow within a boiler are mainly fly ashes, contaminants, and unburnt particles, with the fly ashes being the most part. In biomass-fed boilers ash composition is very important in deposit formation. Substances such as potassium and calcium are prone to form oxides which have softening temperature about 650-700 °C. Since these oxides are collected in the ashes they make the ashes sticky even at relatively low temperature.

In order to take into account this aspect usually a quantity named sticking probability [54] is introduced. This quantity is the fraction of impacting particles which stick to the surface. Factors affecting this parameter are hardness and roughness of the surfaces involved, particle shape, viscosity of the liquid coating on the particle surface, impact velocity and angle, and fraction of molten substances over the surfaces [7].

The most widely used mechanistic approach to model the sticking propensity of a particle is the one proposed by Walsh et al. [55] (for applications see [56]-[59]). This approach considers a cluster of particles, with a given chemical composition and at temperature T , characterized by a sticking probability $p(T)$: this means considering that a

fraction $p(T)$ of the cluster are perfectly sticky, and $[1 - p(T)]$ does not stick at all. Under this model, the mass fraction (also called capture efficiency) of particles that hits an obstacle and sticks to it, is expressed as the sum of three different sticking mechanisms, as reported in (4.68):

$$f_{dep} = \underbrace{p(T_f)}_{\text{sticky particles}} + \underbrace{[1 - p(T_f)] p_{sur}(T_s)}_{\text{sticky deposit}} - \underbrace{k_e [1 - p(T_f)] [1 - p_{sur}(T_s)]}_{\text{erosion}} \quad (4.68)$$

At the right-hand-side of (4.68), the first term represents the contribution to f_{dep} given by the collision of sticky particles (at temperature T_f) against a surface; the second term represents the contribution given by the collision of non-sticky particles (considered at the fluid temperature T_f) against a sticky deposit layer (at temperature T_s); the last one represents the erosion effect. Function $p_{sur}(T_s)$ represents the sticking probability of the deposit surface, that is the sticking probability of an already formed deposit on the surface. This is related to the particle sticking probability through the relation

$$p_{sur}(T_s) = \frac{p(T_s)}{f_{dep}} \quad (4.69)$$

As indicated in (4.68), f_{dep} is a function of the particle and obstacle surface sticking probability, and the erosion coefficient k_e . Accounting for the erosion effect is extremely uncertain, since it involves empirical expressions, depending on the removal mechanisms. Apart from intentional periodic removal of deposits, the other mechanisms are completely random, therefore a sensible evaluation of the erosion coefficient k_e is extremely complicated. Therefore usually the erosion mechanism is ignored. In Chapter 5 re-entrainment of deposited particles is divided in two classes according to the removal mechanisms: removal by turbulence (here called re-suspension), and by other impacting particles (the real erosion mechanism, here called removal). Both of the mechanisms will be further discussed in Chapter 5 but here it is anticipated that whilst re-suspension is studied by several years and some models are available, removal seems a mechanism still not completely clear. Models found in literature are not completely clear and further studies are needed. In any case models proposed for re-suspension can be hardly expressed as in the form of the erosion term in (4.68), thus erosion will be considered following one of the models reported in Chapter 5.

As far as the particle sticking probability is concerned the widely used model is that called Critical Viscosity model (CVM). It relates the sticking probability of a given particle to its physical and chemical characteristics using expressions easy to implement in a code [7]. It assumes that the sticking probability is inversely proportional to the particle viscosity η ; further, particles are assumed to be perfectly sticky when their viscosity decreases below a reference value called critical viscosity η_{ref} [7], [54], [60]:

$$p(T) = \begin{cases} \frac{\eta_{ref}}{\eta} & (\eta > \eta_{ref}) \\ 1 & (\eta \leq \eta_{ref}) \end{cases} \quad (4.70)$$

An estimation of η_{ref} can be pursued after different approaches. Some authors dealing with pulverized coal combustion assume a constant value equal to 10.0^5 Pa·s [56], [60], whereas others [7] suggests 10.0^3 Pa·s. An alternative involves determining the temperature of critical viscosity T_{cv} , that is the temperature under which the viscosity of a given material abruptly increases with temperature [54] (Figure 4.18).

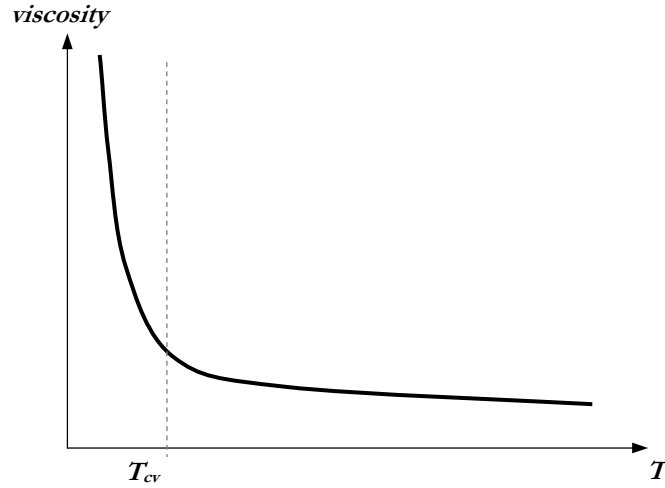


Figure 4.18 – Curve of viscosity as a function of temperature.

This temperature is evaluated using empirical relations depending on particle composition. Once T_{cv} is known, the critical viscosity can be related to it via a model such as the widely used Urbain's one [54], [60]:

$$\log\left(\frac{\eta_{ref}}{T_{cv}}\right) = A + \frac{10^3 B}{T_{cv}} \quad (4.71)$$

where A and B are model constants (dimensional) depending on particle composition. By replacing T_{cv} with the effective temperature T , and η_{ref} with η , equation (4.71) gives also the effective viscosity η of particles at that temperature. Therefore $p(T)$ and $p_{sur}(T_s)$ are computed, respectively using eqs. (4.70) and (4.69), and in turn the capture efficiency f_{dep} is evaluated by using eq. (4.68).

Note that this model can be applied without modifications if the PCT approach is adopted. In this case at each time step is known the concentration of particles in a cell, so deposited particles can be computed following equation (2.5). On the contrary, if the SPT approach is adopted the model must be modified. A particle cannot be fractionated, thus the sticking efficiency f_{dep} has no physical meaning; on the other hand sticking probability concept can still be used. Equation (4.70) can be modified as

$$p(T) = \begin{cases} 0 & (\eta > \eta_{ref}) \\ 1 & (\eta \leq \eta_{ref}) \end{cases} \quad (4.72)$$

that is if $\eta \leq \eta_{ref}$ particle sticks otherwise it does not stick.

This model, with or without modifications, does not take into account the physics of impact as the previous models do, and at the moment to the author's knowledge there is a lack in experiments to study the temperature effect on the adhesion force acting on a particle during contact. Further studies are needed.

CHAPTER 5

Particle re-suspension modelling

Particle re-suspension, that is the detachment of deposited particles, is still not completely understood and theoretical and experimental studies are still in progress. Re-suspension phenomenon is very complicate because several factors are involved, as well summarized by Ibrahim et al. [61], such as roughness of the bodies in contact, flow field fluctuations, adhesion forces, forces of cohesion between particles, humidity, and velocity of the incident particle. Humidity negatively affects the re-suspension because of the absorption of water vapour at the particle-surface interface and its effects on the adhesion. Corn [62], and Corn and Stein [63] found that humidity effect on adhesion force is almost negligible with relative humidity up to 30%, but rapidly increases thereafter. Roughness is always present even for nominally ‘smooth’ surfaces and some experiments [64] reveals that even small values of roughness suffice to reduce the pull-off force to a very small fraction of its value for smooth surface. New impacting or rebounding particles can impact deposited particles thus supplying sufficient momentum to them to overcome their adhesion with the surface.

A model which aims to predict the particle deposition should take into account all these aspects but the task is not simple and often some of them are omitted in models.

Particles deposited on a surface can be detached mainly by two mechanisms: hydrodynamic forces induced by flow field fluctuations due to turbulence, or impact of other particles. Re-suspension occurs when forces produced by the relevant mechanism are sufficiently strong to overcome the adhesion of the involved particles.

For the sake of simplicity in this work re-suspension induced by flow fluctuations will be referenced simply as re-suspension. On the contrary re-suspension due to impact of other particles will be named removal.

In this section models for particle re-suspension and removal are analysed.

5.1 Particle re-suspension

A particle stuck to a fixed surface can be considered in a state of equilibrium. If particle is exposed to a fluid flow, it is subjected to aerodynamic forces and moments which can alter the equilibrium state. Particle is held on the surface by the adhesion force F_A and body force F_B (i.e., gravitational and buoyancy). F_B for particles in the micron range is very small and often is neglected in the force and momentum balance equations. If the microparticle is contained within the viscous sublayer it experiences a linear mean shear flow which produces lift and drag forces (F_L and F_D) as well as moments of them. Figure 5.1 illustrates a deposited particles and the forces acting on it.

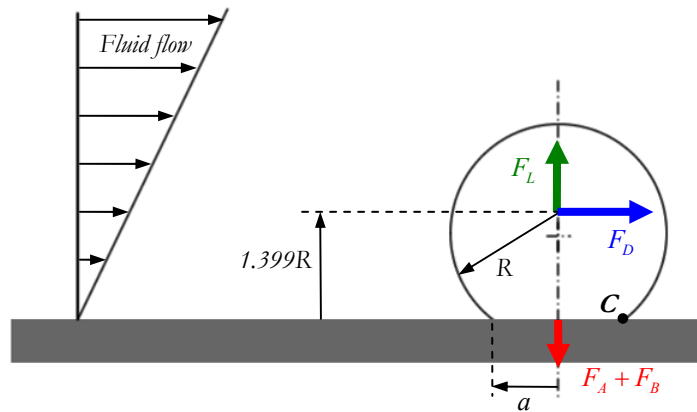


Figure 5.1 – Forces acting on a deposited particle.

According to Zhang et al. [65], and Ibrahim et al. [61], re-suspension can occur in three different ways: lift-off, sliding, and rolling. Lift-off is due to the lift force F_L which develops on particles because of flow velocity fluctuations. Depending on the intensity of velocity fluctuations and the particle size and density, the lift force can be sufficiently strong to overcome the adhesion F_A and body F_B (i.e., gravitational and buoyancy) forces thus detaching the particle. Lift-off takes place when it results

$$F_L > (F_A + F_B) \quad (5.1)$$

Drag force F_D can cause the sliding of the particle if it is large enough to win the friction between particle and surface; detachment condition in this case writes

$$F_D > f_s (F_A + F_B - F_L) \quad (5.2)$$

with f_s the static coefficient of friction. The rolling of particles over the surface is due to the moments of the forces acting on the particle. If drag and lift moments around point C (Figure 5.1) overcomes the moments of adhesion and body forces, particle rolls. As reported in [65], drag force acting on a particle near a wall could be substituted by an effective force acting not in the centre of the particle but at a distance of $1.399 \cdot R$ from the surface (Figure 5.1). Recalling that δ is the relative approach, the distance of drag

force application becomes $(1.399 \cdot R - \delta)$. Therefore the condition for particle rolling around point C is

$$(1.399R - \delta)F_D > (F_A + F_B - F_L)a \quad (5.3)$$

A different approach can be found in Reeks and co-authors [66], [67]. In contrast to the force balance models, authors consider the influence of turbulent energy transferred to a particle from the flow. This energy maintains the particle in vibrational motion on the surface within a surface adhesive potential well. Particle continues to accumulate energy from the flow, and detachment takes place when the particle has accumulated enough vibrational energy to escape from the well.

A number of models for re-suspension were developed in the past (see for example [61], [65]-[70]), each focusing on a particular aspect of re-suspension. In this work the force balance approach is adopted, and in the following the two models from Zhang et al. [58] and Ziskind et al. [71], are analysed.

5.1.1 Zhang et al. model

The model developed by Zhang et al. [65] is based on equations (5.1)-(5.3). The authors developed the model for submicron particles, but it can also be applied to supermicron ones. Zhang et al. focus their attention on the adhesion-induced deformations which make the adhesion force increase in comparison with the simple case of adhesion of an undeformable particle. Thus re-suspension is affected by this phenomenon.

Considering a particle of radius R stuck on a flat surface, the authors express the adhesion force as a sum of two terms: one due to the adhesion of undeformable sphere, and one due to deformation.

$$F_A = F_0 + F_d = \frac{A \cdot R}{6z_0^2} \left(1 + \frac{a^2}{Rz_0^2} \right) \quad (5.4)$$

where A is the Hamaker constant and z_0 the separation distance between the particle and the surface. The Hamaker constant is a constant used for describing the Van der Waals force. The magnitude of the Hamaker constant reflects the strength of this force between two particles, or between a particle and a substrate. It depends on the material properties of both the interacting bodies and the intervening media [72].

Re_p for a particle stuck to a surface is much smaller than one, because flow velocity assumes very low values close to a surface. Therefore, according to Cherukat and McLaughlin [73], lift force can be written as:

$$F_L = \frac{9.22\mu_f^2}{\rho_f} Re_p^3 \quad (5.5)$$

Since their study is focused on submicron particles, Zhang et al. [65] write equation (5.1)-(5.3) neglecting F_B . Moreover, since F_L is several orders of magnitudes smaller

than the drag force, it is too small to lift-off the particle, hence this re-suspension mechanism is not taken into account.

Neglecting F_B and F_L the sliding condition becomes

$$RS = \frac{F_D}{F_A} > f_s \quad (5.6)$$

and the rolling condition

$$RM = \frac{1.399F_D R}{F_A a} > 1 \quad (5.7)$$

Abd-Elhady et al. [74] used the Zhang et al. model as comparison to their experimental studies to determine the minimum gas speed to avoid fouling on heat exchanger tubes. Results are in good agreement. Equation (5.7) in [74] is written taking into account all the forces which can exert a moment on the particle, and the relative approach. Doing this (5.7) rewrites

$$RM = \frac{F_D (1.399R - \delta)}{(F_A + F_G + F_{BU} + F_L) a} > 1 \quad (5.8)$$

where F_G is the gravitational force, F_{BU} is the buoyancy force. δ is computed in Zhang et al. [58] as $\delta = R - (R^2 - \alpha^2)^{1/2}$, and the contact radius $a = (2\Gamma R/H)^{1/2}$. H is the hardness of the deformed solid.

5.1.2 Ziskind et al. model

Several models indicates as criterion for particle re-suspension that presented in the previous section, that is that the moment of the forces acting on a particle must exceed the adhesion moment $F_A a$. Ziskind et al. [71], according to the evaluation of the dependence between the contact radius and the force from the adhesion models, contest this approach.

Ziskind et al. analyse two different adhesion models: the JKR model, already mentioned above, and the Derjaguin et al. [75] (DTM). Since DTM is not very diffused, in this work the analysis is restricted to the JKR model. In this model a relation between applied force F and contact radius a is given by equation (4.5):

$$\frac{a^3 \left(\frac{4}{3} E^* \right)}{R^*} = F + \frac{3}{2} \pi \Gamma R^* + \sqrt{2\pi \frac{3\Gamma}{2} R^* F + \left(\frac{3}{2} \pi \Gamma R^* \right)^2} \quad (5.9)$$

Introducing the dimensionless applied force $F^* = -F/(3\pi\Gamma R/2)$ and rearranging, (5.9) provides the dimensionless contact radius a^* as a function of the dimensionless applied force.

$$a^{*3} = \frac{a^3 \left(\frac{4}{3} E^* \right)}{\left[\frac{3}{2} \pi \Gamma R^{*2} \right]} = \left(-F' + 1 + \sqrt{-2F' + 1} \right)^{1/3} \quad (5.10)$$

Note that F^* by definition, corresponds to a detaching force applied to the particle.

Figure 5.2 illustrates the dependence between the dimensionless contact radius and the applied force (blue dashed line): it shows a minimum in contact radius when $F^* = 0.5$, which corresponds to the dimensionless pull-off (or adhesion) force:

$$F_{\max}^* \equiv F_A^* = \frac{F_A}{\frac{3}{2} \pi \Gamma R^*} = 0.5 \quad (5.11)$$

The maximum in dimensionless contact radius is reached when $F^* = 0.0$ (i.e., no detaching force is applied). In this case equation (5.10) yields to the equilibrium contact radius as $a_e^* = 1.26$. Therefore following the JKR theory, the adhesion moment writes as

$$F_A^* a_e^* = 0.5 \cdot 1.26 = 0.63 \quad (5.12)$$

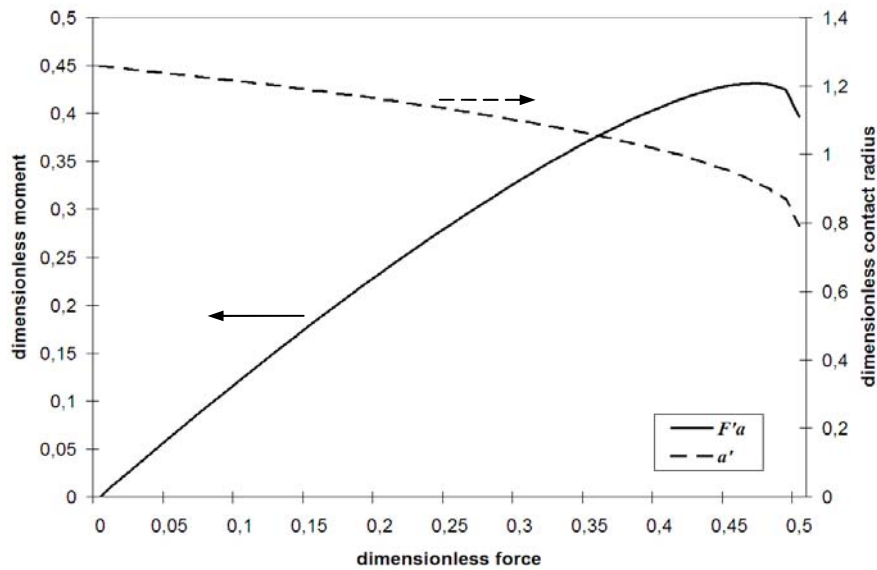


Figure 5.2 – Dependence between dimensionless contact radius and force, and dimensionless moment and contact force.

Figure 5.2 also reports the dimensionless detaching moment $F^* a^*$ as a function of F^* (red continuous line) showing a maximum value $(F^* a^*)_{\max}$ of about 0.42. Thus, comparing this value with the adhesion moment it results

$$\frac{(F^* a^*)_{\max}}{F_A^* a_e^*} = \frac{0.42}{0.63} = \frac{2}{3} \quad (5.13)$$

that is the maximum moment before the particle is detached from the surface do not exceed $(2/3)F_A a_e$. Therefore the commonly used models which assume $F_A a_e$ as a critical value of the moment for re-suspension, i.e., the value of the adhesion moment which has to be overcome for detaching the particle from the surface, underestimate the phenomenon. Accordingly, Ziskind et al. propose to use $(2/3)F_A a_e$ as critical adhesion moment.

5.2 Particle removal

Modelling removal of particle from a surface by impaction of other particles is a very complicated but also challenging task. Particle can be readily removed from a surface by impaction of other particles rather than by air flow fluctuations, because of the greater momentum carried by a particle compared to an air packet of the same volume moving at the same speed. Factors which make this phenomenon the most complicated in particle impact/adhesion mechanics are the impact velocity, the angle of impact, the number of particles attached to that impacted and their packing, the adhesion force in multiple-contact, and possibly the sintering of the deposited layer.

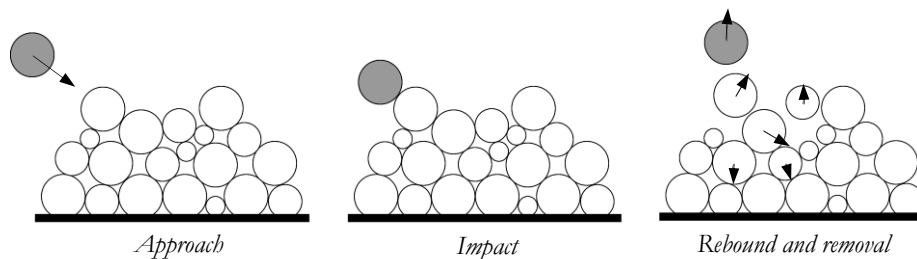


Figure 5.3 – Removal of particles from a surface by impact of another particle.

When a particle impacts a layer of deposited particles its momentum is transferred to them in different fractions depending on the impact angle, the number of particles in the layer, etc.. This causes elastic and possibly plastic deformations in all the particles involved. When at the end of the impact the incident particle separates from the target one, a number of particles in the layer are still moving with some fractions of velocity of the incident particle. Some of those particles can also be ejected from the layer as results of reaction forces due to impacts with other particles in the layer and the surface. A sketch of the process is depicted in Figure 5.3. Predicting particle removal is then very complicated and a lot of factors and variables have to be taken into account.

Perhaps this is the reason why particle removal is an almost completely unknown phenomenon. Few experiments have been done and even less models developed in the past. John et al. [76], measured the removal of 8.6 μm -diameter ammonium fluorescein particle from a Tedlar surface when impacted by 3.0 μm -diameter particle of the same material in a 40 m/s jet. They also proposed a model to predict the removal but, as the authors said and John reported in [77], theoretical results underestimate the measurements up to two orders of magnitude. John and Sethi [78] measured the threshold impact velocity for removal comparing results with predictions provided by the model proposed in [76] and a second model named momentum-energy model. Both of them underestimate the removal, but the threshold removal velocity predicted by momentum-energy model is just half of the measured one. The works of John and co-authors were the first attempt to model the removal by particle impaction. More recently some authors have faced this problem. Experiments by Abd-Elady and co-workers (see for example [79]-[81]) provide a measurement of particle removal as a function of the velocity of impacting particle. Van Beek [36] uses the two-body collision model (proposed by Werner [82]) which reduces the impact of a particle with a layer of deposited particles to that between two particles introducing a mass coefficient C_m . Indicating with m_1 and m_2 the mass of impacting and target particles respectively, m_2 can be written as a fraction of impacting particle mass $m_2 = C_m m_1$. In this case m_2 represents the mass of the deposited layer of particles. Using this relation, COR (see section 4.2) of the impacting particle can be calculated as in the case of two impacting particles. Moreover motion of particles in the layer can be studied using the same approach thus evaluating if some of them are removed from the layer.

It is not clear whether the two body collision correctly predict the removal of particles or how it behaves in the case of multiple impacts (i.e. incident particle impacts two or more particles in the layer contemporarily), but it could be a base for further developments.

CHAPTER 6

Deposit growth

Deposit growth is a process affected by several factors most of which has been analysed in the previous chapters (i.e., mechanics of impact, adhesion, and re-suspension). In all those models particles are always considered alone, i.e., as a single discrete entity. For instance the net adhesion energy computed in Chapter 4 represents the energy required to break the contact between a particle and a second body. In fact during the deposit formation process the simple impact particle-plane occurs just during a short transitory time interval. In the remaining time the impacting particles hit simultaneously a plane and other deposited particles, or only these latter if there is a deposit layer already formed. Thus the net adhesion energy changes and the deposit growth changes accordingly.

In order to account for this aspect it is important analysing the particle arrangement within a deposit.

6.1 Deposit growth: the particle packing approach

Particles that hit a surface place themselves according to the impact point, the presence of other particles on the surface, their deformations, etc.. Modelling these aspects is not simple but it is important in particle deposition/removal prediction, thus it should be considered somehow. The circle and sphere packing problems can provide some useful information.

Considering circles having the same size it results that the best regular arrangement to cover a surface is the hexagonal packing (HP) arrangement (see Figure 6.1) as reported in [83]. In this arrangement each circle is surrounded by other six circles as shown in figure, and the packing density (i.e., the ratio between the surface covered by circles and that of a polygon adjacent to them) writes:

$$\rho_{2D} = \frac{\pi}{\sqrt{12}} \approx 0.9069 \quad (6.1)$$

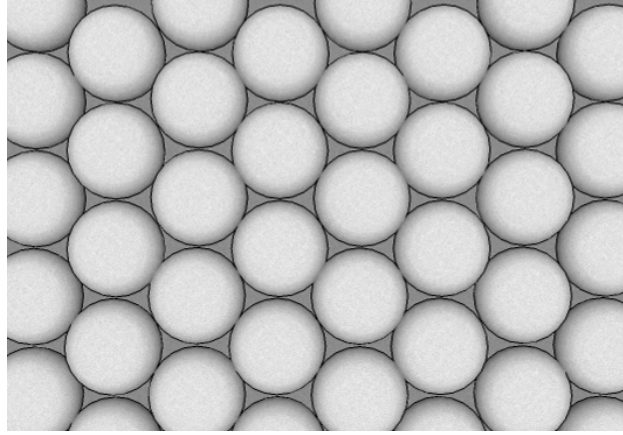


Figure 6.1 – 2D hexagonal packing.

The formation of a first layer of deposit can be viewed as a similar 2D problem. Assuming that all the particles depositing on a given surface S (i.e., the wall surface of a domain cell) place themselves according to the HP, the number of particles $n_{p,2D}$ that cover S it is readily calculated:

$$n_{p,2D} = \text{int}(\rho_{2D}S) \quad (6.2)$$

When a surface is covered by $n_{p,2D}$ particles, a first deposit layer is formed, and its thickness $h_{dep,1}$ results

$$h_{dep,1} = d_p f_{dep}$$

where $f_{dep} \leq 1$ is a factor which accounts for particle deformations. Figure 6.2 shows the ratio between plastic deformation and particle radius as a function of dimensionless Hertzian force (4.54) (particle characteristics are reported in Table 6.1). As shown in figure plastics deformations are negligible in comparison with particle diameter considering dimensionless Hertzian force up to 50. Thus it can be assumed $f_{dep} = 1$.

With this assumption the first deposit layer thickness simply equals the particle diameter:

$$h_{dep,1} = d_p \quad (6.3)$$

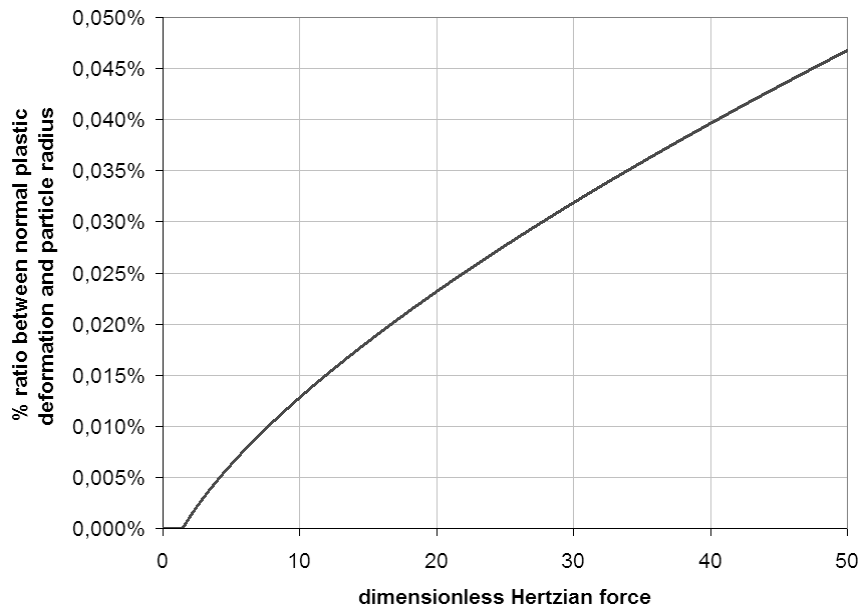


Figure 6.2 – Plastic deformations of particle as a function of dimensionless Hertzian force.

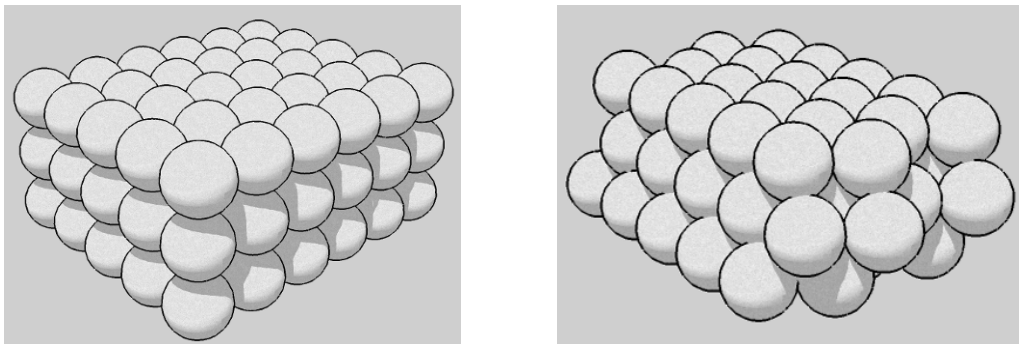


Figure 6.3 – Two different sphere arrangements in sphere packing problem: simple cubic (left), hexagonal (right).

Once the first deposit layer is completed, the 2D problem turns into a 3D one, and now the sphere packing problem, first faced by Kepler in 1611, provides useful information. In the sphere packing problem different regular arrangements are available. Figure 6.3 shows two examples: the simple cubic (SCP) and hexagonal packing (HP). The latter is that which guarantees the best packing (as guessed by Kepler and demonstrated by Hales [84]), that is the largest number of spheres in a given volume, having a volume density equal to

$$\rho_{3D} = \frac{\pi}{\sqrt{18}} \approx 0.74048 \quad (6.4)$$

Assuming that during the second (or successive) layer formation particles place themselves according to the HP, the deposit thickness can be evaluated considering a replicable section of the HP pattern as reported in Figure 6.4. Due to the sphere packing the deposit thickness $h_{dep,2}$ is not simply the sum of two single layers, that is $2 h_{dep,1}$. It results

$$l = 2R\sqrt{2} = 2R + 2\lambda \quad (6.5)$$

which leads to

$$\lambda = (\sqrt{2} - 1)R \quad (6.6)$$

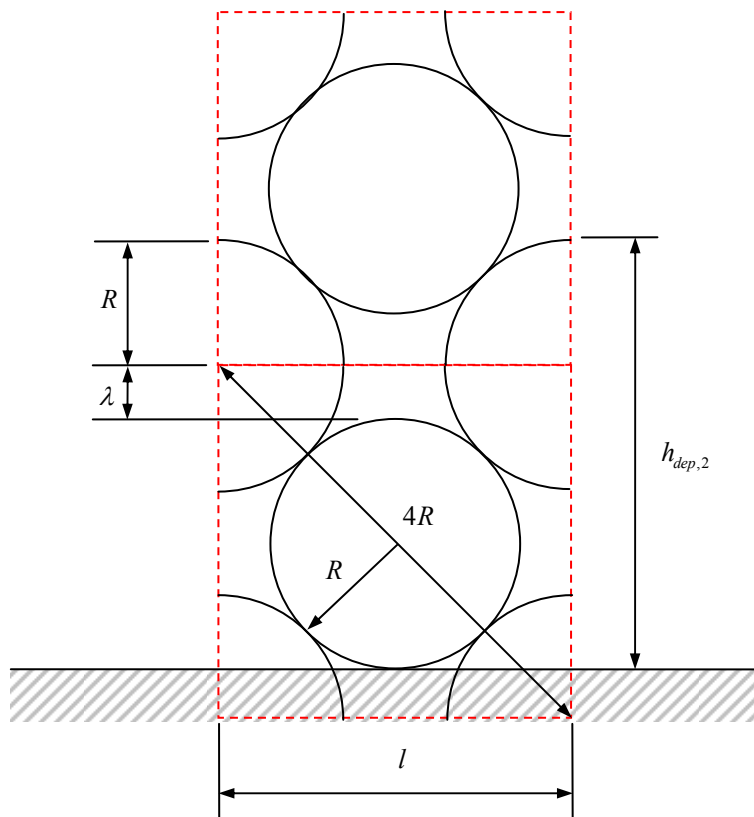


Figure 6.4 – Section of the HP arrangement.

Hence when a deposit is composed by two layers of particles, assuming the HP arrangement its thickness results

$$h_{dep,2} = h_{dep,1} + (\lambda + R) = (2 + \sqrt{2})R \quad (6.7)$$

In general when the deposit is composed by n_l layers the global thickness writes:

$$h_{dep,l} = h_{dep,1} + (n_l - 1)(\lambda + R) = \left[2 + (n_l - 1)\sqrt{2} \right] R \quad (6.8)$$

This approach is acceptable when particles impact on a deposit layer composed by similar particles. In fact in a real case the situation is much more complicated because different particles are entrained by the flow and impact a surface or a deposit layer at the same time. The above assumed sphere packing is therefore different from the real case. In order to take into account somehow the effect of different particles depositing at the same time, a correction factor f_{pack} should be introduced leading to:

$$h_{dep,l} = \left[2 + (n_l - 1)\sqrt{2} \right] R f_{pack} \quad (6.9)$$

where f_{pack} has to be expressed as a function of the size distribution of particles in the real flow.

6.2 Deposit growth: an engineering approach

Although the model presented in the previous paragraph provides a logical approach to the deposit prediction problem, its application to a real case needs more investigations and experimental studies, especially for the evaluation of the correction factor f_{pack} .

A different and more engineering approach can be followed in the meanwhile, based on the knowledge of the deposit bulk density ρ_{dep} . Knowing this quantity by experimental measurements the evaluation of the deposit thickness is quite simple. Considering n_p particles deposited on a surface S , the total mass deposited is

$$m_{dep} = m_p n_p \quad (6.10)$$

which can be also written as

$$m_{dep} = \rho_{dep} h_{dep} S \quad (6.11)$$

Combining equations (6.10) and (6.11) it results

$$h_{dep} = \frac{m_p n_p}{S \rho_{dep}} \quad (6.12)$$

6.3 Sticking velocity in presence of a deposit layer

According to van Beek [36], the net adhesion energy in a two bodies contact is:

$$\Delta Q = 7.09 \left(\frac{R_c^4 \Gamma^5}{E^{*2}} \right)^{1/3}$$

where R_c for elastic impact is equal to R^* . ΔQ represents the energy required to break the contact between two bodies. As said in section 6.1 during the deposition process a part from a transitory time interval, impacting particles hit simultaneously the surface and other particles, or only other particles if a deposit layer is already formed. In this case the net adhesion energy has to account for a multiple contact.

To better understand the process consider Figure 6.5. When a particle impacts a clean surface (part-plane impact Figure 6.5 a) ΔQ is the net adhesion energy between a particle and a plane. As particles deposit on the surface, but the first deposit layer is not completely formed, the new impacting particles hits both the plane and some deposited particles. Assuming that deposited particles follow the HP arrangement described in section 6.1, one can say that on the average each new impacting particle (red sphere in figure) collides the plane and three other particles (green spheres in Figure 6.5 b). In this case (here called 1st layer impact) the net adhesion energy is given by the sum of the energy of part-plane impact and three times the part-part (particle-particle) impact adhesion energy. As the deposit process continues, the first layer is formed, and a new impacting particle on the average does not hit the plane, but only six particles, three in the new deposit layer (green spheres in Figure 6.5 c), and three in the previous one (yellow spheres in Figure 6.5 c). In this case (here called 2nd layer impact), the net adhesion energy is six times the net adhesion energy of part-part impact.

Considering particles having the characteristics reported in Table 6.1 adhesion energy in the different impacts is evaluated and reported in Figure 6.6. As shown in figure the net adhesion energy increases as the deposition process proceeds. This means that for impacting particles it is easier to stick to a deposit layer than to a clean surface.

Recalling that the sticking velocity can be evaluated imposing $e = 0$ in the COR expression, equation (4.13) reported below

$$e^2 = 1 - \frac{\Delta Q}{\frac{1}{2} m^* v_{i,n}^2} \quad (6.13)$$

The sticking velocity calculated for different impacts, is reported in Figure 6.7. As shown the sticking velocity for part-plane impact is quite smaller than that for 1st or 2nd layer impact, therefore particle impacting on a deposit layer, both complete and not, are more prone to stick and, accordingly, less prone to be removed as also pointed out before.

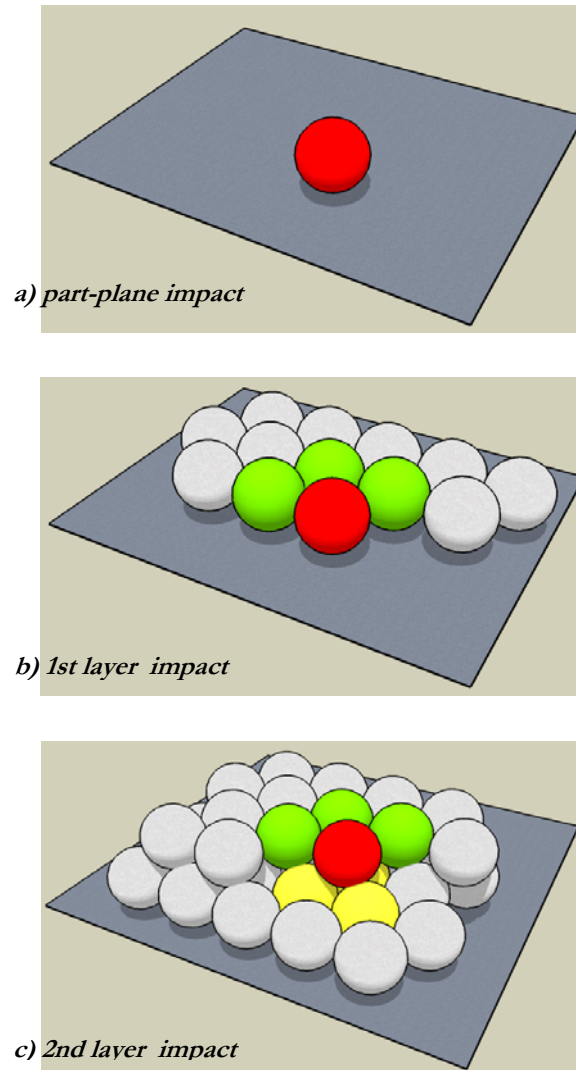


Figure 6.5 – Different impacts during the deposit formation process.

| | |
|----------------------------|-------------------------|
| Particle radius, R | 25.0 μm |
| Particle density, ρ | 8960 kg/m^3 |
| Young modulus, E | 1,29E+11 N/m^2 |
| Poisson coefficient, ν | 3,30E-01 |
| Surface energy, Γ | 0,12 J/m^2 |

Table 6.1– Particle characteristics used to evaluate the net adhesion energy.

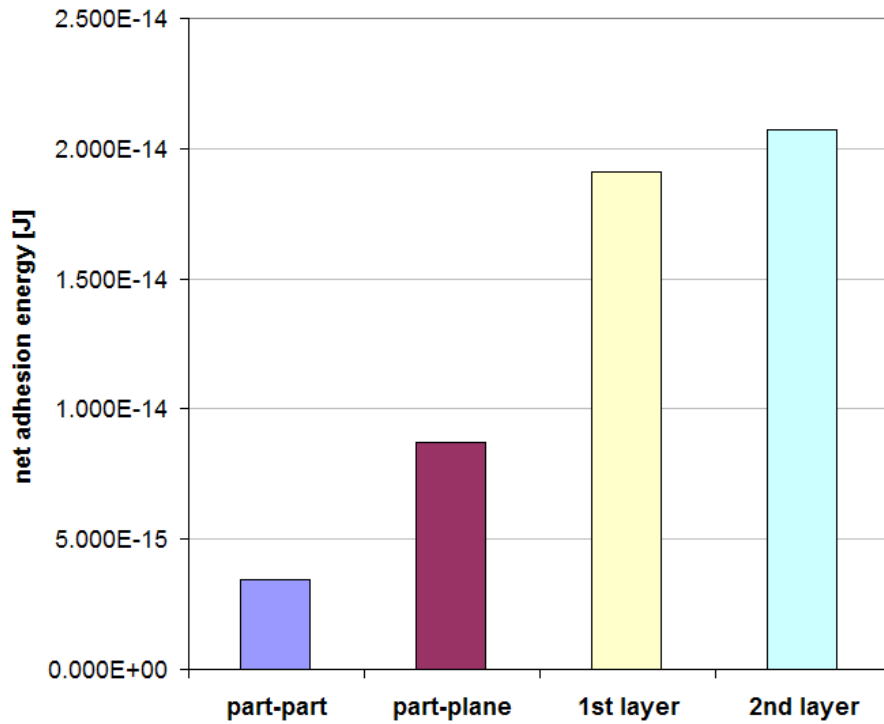


Figure 6.6 – Net adhesion energy in different impacts.

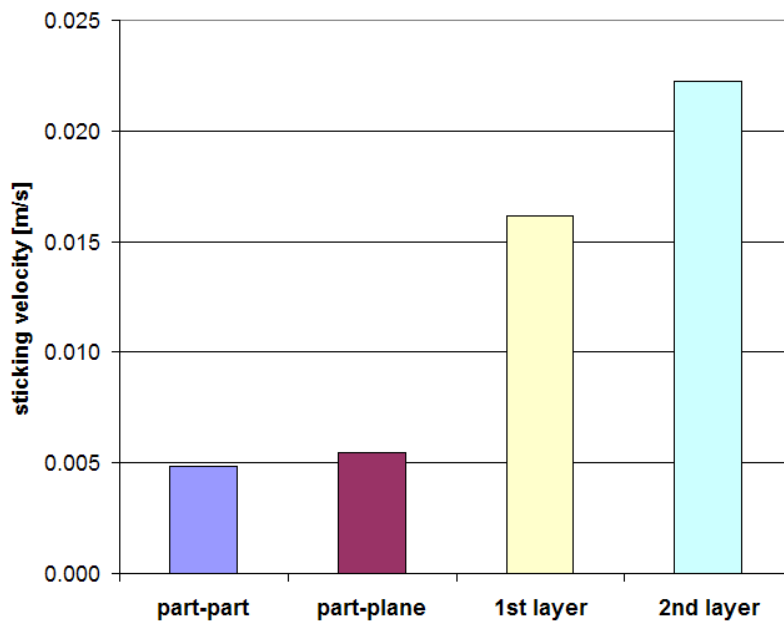


Figure 6.7 – Sticking velocity in different impacts.

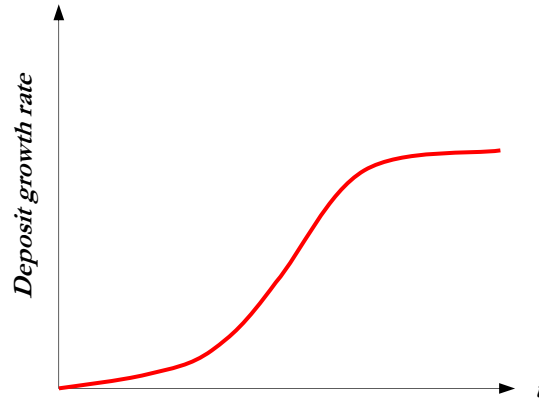


Figure 6.8 – Deposit growth rate as a function of time.

The above analysis is summarised by the curve reported in Figure 6.8. Deposition growth is a process which starts slowly and then, as some particles deposit, becomes faster.

6.4 Re-suspension from a bed of particles

As said above, particle packing in a deposit layer affects the net adhesion energy, thus also the sticking velocity. The presence of a deposit layer (partially or completely formed) influences also the re-suspension. In this case it is extremely difficult to evaluate and model this phenomenon. All the models presented in literature, to the authors knowledge, concern the re-suspension of a particle presenting a single contact (i.e., with a plane or with a second body), and none considers the problem of re-suspension of a particle with multiple contacts, that is what really happens in a deposit layer. The problem is sketched in Figure 6.9 and Figure 6.10. The first one represents the case of a particle being contemporarily in contact with a plane and a second particle. Recalling chapter 5, when a particle is in contact with a plane the force moments are computed around point C_0 (Figure 6.9), whilst in the case of a second contact with a deposited particle the point that should be considered in moment evaluation is C . Therefore the moment balance (5.3) rewrites:

$$(0.399R - a_2)F_D > (F_{A1} + F_B - F_L)R + F_{A2}a_2 \quad (6.14)$$

where R is the particle radius, a_2 the particle-particle contact radius, F_B is the body forces, F_{A1} and F_{A2} the adhesion force due to the contact with the plane and particle respectively. Form equation (5.3) the rolling moment criterion in the case of a double contact (RM_{2c}) results:

$$RM_{2c} = \frac{F_D(0.399R - a_2)}{(F_{A1} + F_B - F_L)R + F_{A2}a_2} > 1 \quad (6.15)$$

Recalling the criterion in a single contact (RM , equation (5.7) or (5.8))

$$RM = \frac{F_D (1.399R - \delta)}{(F_A + F_B - F_L)a} > 1$$

and comparing it with (6.15) it comes out that in case of a double contact re-suspension is more difficult to occur. As a matter of fact, F_D , F_B , and F_L being constant, and considering that F_A and a in (5.8) equals F_{A1} and a_1 (respectively) in (6.15), the numerator of RM_{2c} is smaller than that of RM ; on the contrary, the denominator of RM_{2c} is larger than that of RM . Therefore, with the above assumptions and considerations, it results $RM_{2c} < RM$, that is in the same flow conditions re-suspension occurs more easily in a single contact than in a double contact (i.e., in the case of a partially formed deposit layer). The situation is even more complicated when a general multi-contact case is considered (Figure 6.10).

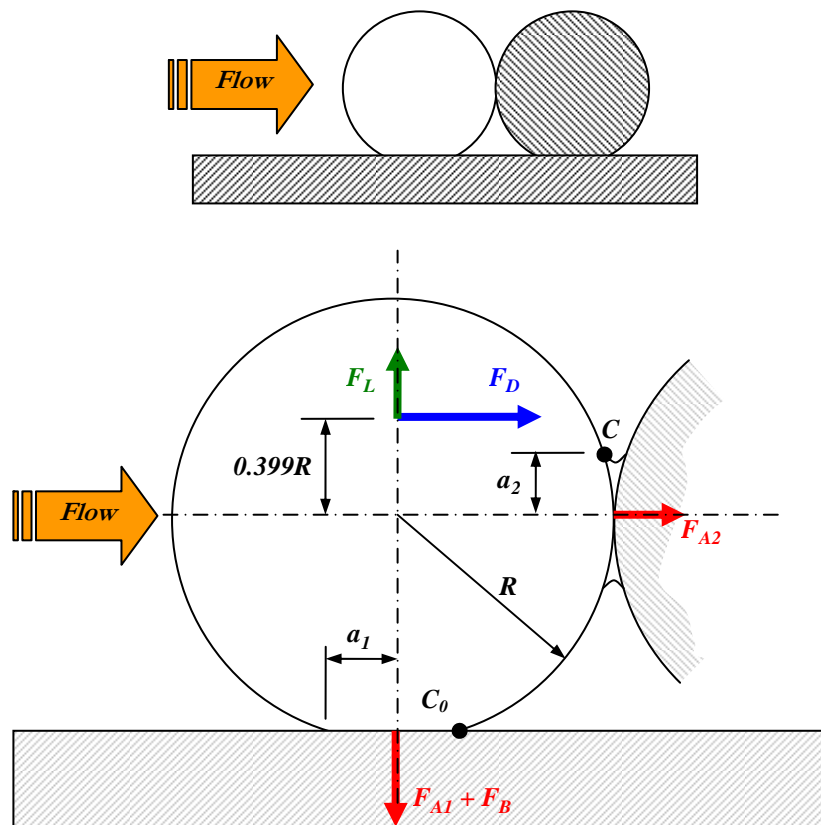


Figure 6.9 – Re-suspension: forces acting on a particle in contact with a plane and a second particle.

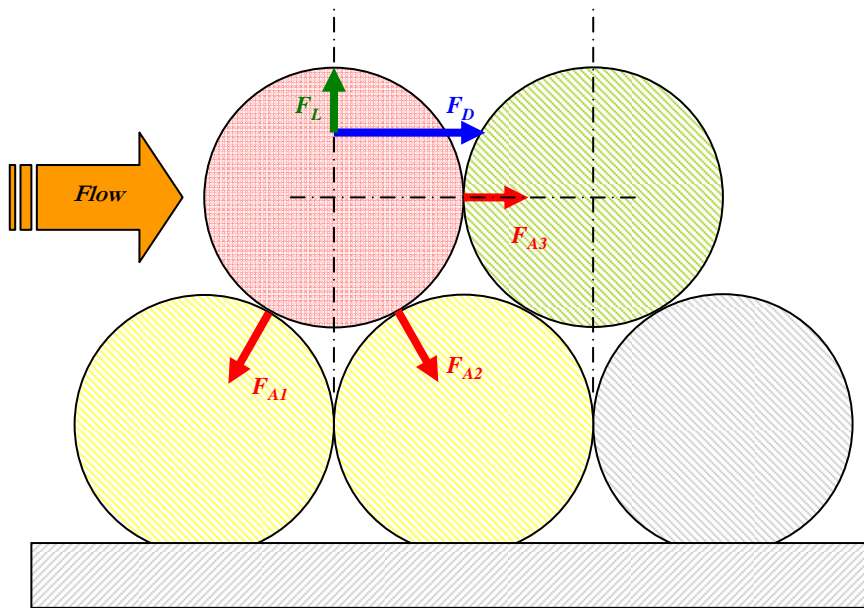
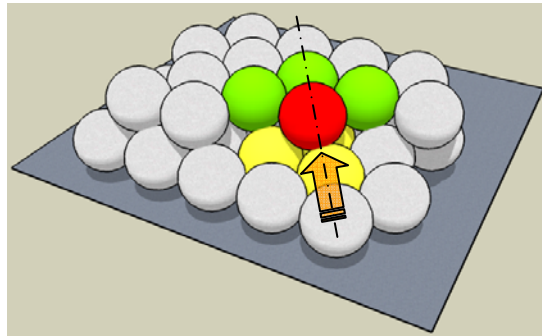


Figure 6.10 – Re-suspension: forces acting on a particle in a multiple contact case.

CHAPTER 7

Simulations: cases and models considered

The models proposed and analysed before and implemented on a computational code have been validated on a number of different applications. Relevant results are discussed in chapters 8 and 9, with particular attention to the differences among different approaches, and the applicability of the models to specific cases.

Before showing the results, a global view of the cases simulated and models adopted is reported here.

7.1 Summary of performed simulations

Table 7.1 gives a summary of all the simulations performed in this work.

A preliminary simulation, used for developing and testing the code for deposit prediction, was conducted considering a complex industrial flow carrying a large amount of particles. A biomass-fed furnace was selected: a RANS (standard $k-\epsilon$) simulation provided the flow field. The PCT approach is used in order to model turbulent dispersion, and particle deposition is controlled by temperature. Results of this case have been discussed in Chapter 3. Because of lack of any experimental data regarding the deposition, no validation of the method was possible.

More detailed models for particle impact/adhesion have been then introduced and tested, in order to better understand the particle deposition phenomenon and the parameters which mostly affect it.

First the code was validated using the work of Zhou et al. [85] (i.e., a long cylinder in a cross flow) as reference. A U-RANS simulation provided the flow field. SPT approach is used as turbulent dispersion model, and the temperature controlled adhesion model is adopted. As a matter of fact the reference flow is hot (1293 K) hence softening of particles has to be considered. The effect of impact angle was also analysed. Results will be discussed in Chapter 8.

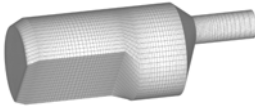
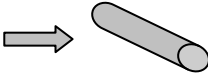
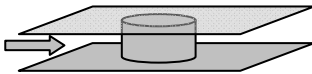
| <i>Flow configuration</i> | <i>Fluid velocity</i> | <i>Particle dispersion</i> | <i>Deposition model</i> |
|---|-----------------------|---|--|
| Industrial application: <i>Biomass combustor</i>  | RANS (k-ε) | PCT (standard) | - Temperature controlled |
| Model Validation case: <i>Long cylinder in a cross flow</i>  | RANS (ζ-f) | SPT | - Temperature controlled - Impact angle Deposit Growth: Engineering approach |
| Application 1: <i>Short wall-bounded cylinder</i>  | LES | PCT (modified) SPT | - RM (Zhang) - RM (Zhang) - Van Beek - Thornton & Ning - Feng - Impact angle - Re-suspension |

Table 7.1– Synoptic of the simulations performed in this work.

In order to test other adhesion models a different case was simulated (Application 1, a wall-bounded short cylinder). In this case the flow field is provided by LES. Adhesion models tested are all those presented in Chapter 4, and also re-suspension (Zikind model) is tested. As far the dispersion model, SPT and a modified version of the PCT have been used. It has to be noted that the introduction of a re-suspension model has not produced a deposit significantly different from that without re-suspension. This is due to the low velocity of the flow which is not sufficient to detach particles. Moreover the use of the Konstandopoulos model to take into account the effect of impact angle, provides no deposit at all. As a matter of fact in this case, because of the particular geometry and the starting positions of particles, deposit only forms on the walls showing an impact angle larger than the critical one. Results will be presented in Chapter 9.

CHAPTER 8

Validation of models and algorithms

In order to better simulate the deposition phenomenon the above discussed models have to be taken into account. Before implementing and evaluating them into the code for particle deposition it is paramount validate it. In this chapter the validation case and results are presented.

8.1 Validation of the code for deposit formation

The work of Zhou et al. is taken as reference [83]. They studied the deposit growth on a tube in cross flow within a small laboratory combustor. It is fed with straw and in order to study the deposit formation the authors placed a cylindrical probe in cross flow (Figure 8.1), at a certain distance from the flame. Further details on the experimental apparatus can be found in [83] and [86].

Figure 8.2 shows the sketch of the domain used for the simulation in this work. The domain was decomposed into 393540 nodes and 368000 hexahedral elements. A U-RANS (ζ -f model) simulation of the flow field was done using a finite volume code (T-Flows). Table 8.1 reports data used in the simulation. The gas evolving within the combustor has a temperature of 1293 K as reported in [83]. Since the composition of the gas is unknown, in this simulation it was substituted by air and its characteristics are taken accordingly. On the basis of these data Re results equal to 1700.

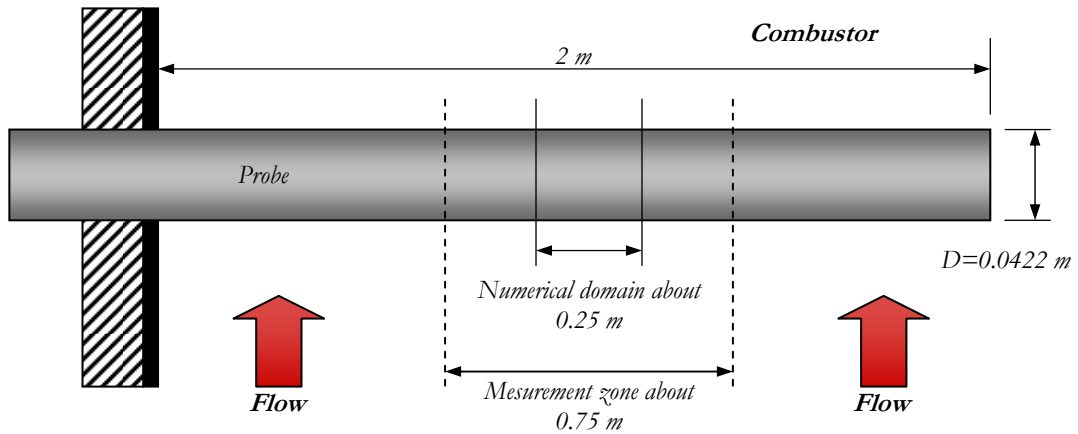


Figure 8.1 – Sketch of the probe location in the reference study.

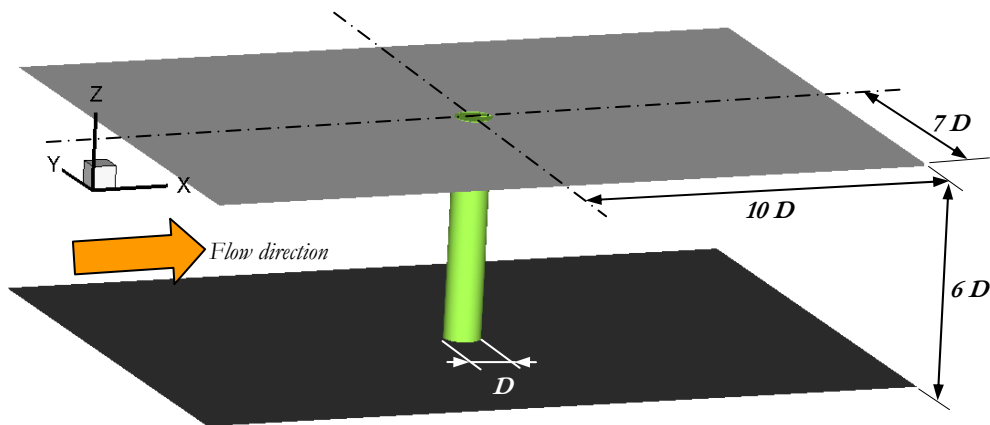


Figure 8.2 – Sketch of the numerical domain.

| | | |
|----------------------|-----------|-------------------|
| D | 4,22E-02 | m |
| gas type | air | - |
| gas velocity | 7,25 | m/s |
| gas temperature | 1293 | K |
| gas density | 0,271 | kg/m ³ |
| gas viscosity μ | 4,93E-05 | kg/ms |
| particle diameter | 8, 25, 58 | micron |
| particle density | 2600 | kg/m ³ |
| Deposit bulk density | 1500 | kg/m ³ |

Table 8.1 – Flow and particle data used in the simulation.

Particle size in [83] are divided into three classes: a sub-micron one, which is neglected in this study because other forces, not considered in the model, become important for this kind of particles; an intermediate class composed by particle of average size equal to $8\ \mu\text{m}$; and a third class composed by coarser particles ($58\ \mu\text{m}$ size). Since particle response time and behaviour are quite different depending on their size, such a size classification seems to coarse to obtain real results.

In the present study 8 , 25 , and $58\ \mu\text{m}$ are considered, with the concentrations reported in Table 8.2. The SPT approach is used. Adhesion is simply accounted for by assuming that a particle which impact a surface sticks to it. This is due to the flow temperature. For such values of temperature the critical viscosity approach (section 4.5) has to be adopted. Assuming that particles are in thermal equilibrium with the flow, that is particles have the same temperature of the flow, an considering a typical chemical composition of flay ashes from straw combustion (see for example [7], [87]), the temperature of critical viscosity is a bit lower than $1293\ \text{K}$. Therefore following the critical viscosity model, particles impacting an obstacle sticks to it.

A shear period ($\approx 2.561\text{E-}02\ \text{s}$) was divided into 37 different realizations, and loaded as new flow field every $6.92\text{E-}04\ \text{s}$, by the code for particle deposition. Particles start from 12 elements at a distance from the tube equal to about a tube radius (Figure 8.3). Different simulations have been performed. In the first one particle size and concentrations are taken equal to those reported in [83] (Table 8.2, simulation A). In the second one (simulation B) particles having size equal to $25\ \mu\text{m}$ are considered. In the last simulation (simulation C) three size classes are considered (8 , 25 and $58\ \mu\text{m}$). This simulation aims at better simulating the real distribution of particles in the flow.

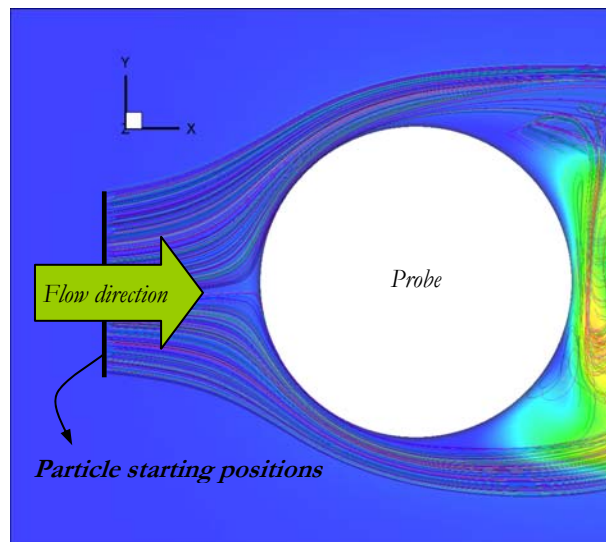


Figure 8.3 – Particle starting positions.

| <i>Simulation</i> | <i>8 μm</i> | <i>25 μm</i> | <i>58 μm</i> |
|-------------------|--|---|---|
| <i>A</i> | 4.9E-7 kg/Nm ³ | - | 9.3E-4 kg/Nm ³ |
| | 8,36E-12 m ³ /m ³ | - | 1,59E-08 m ³ /m ³ |
| <i>B</i> | - | 2.0E-4 kg/Nm ³ 3,41E-09 m ³ /m ³ | - |
| <i>C</i> | 4.9E-7 kg/Nm ³ 8,36E-12 m ³ /m ³ | 4.65E-4 kg/Nm ³ 7,93E-09 m ³ /m ³ | 4.65E-4 kg/Nm ³ 7,93E-09 m ³ /m ³ |

Table 8.2 – Particle concentrations used in the simulations.

8.1.1 Results

Figure 8.4 through Figure 8.12 report the results of the three different simulations.

Figure 8.4 and Figure 8.5 show the predicted deposit thickness after 3.5 h in the case of simulation A, and Figure 8.6 shows some particle trajectories (particle size equal to 8 μm). The results from Zhou et al. [83] (Figure 8.5 a) predicted a very smooth deposit while the real one presents a more irregular shape (Figure 8.7). A part from the irregularity of the deposit shape, authors correctly predicted that deposit thickness at the stagnation point is somewhat lower than that at its sides, as can be seen in Figure 8.7 a) and more evidently in Figure 1.1 [3] here reported in Figure 8.7 b) for comparison. A good agreement is shown even for the maximum angular position of the deposit, which is about 70-75° from the stagnation point.

The present numerical code, using the coarse size distribution given in [83], provides different results. Smaller particles (i.e., 8 μm) give almost no contribution to deposit since their concentration is very small and they follow quite closely the streamlines of the flow (response time $\approx 1.9\text{E-}4$ s). Thus larger particles give the main contribution to the deposit. Figure 8.5 b) shows the present simulation. After 3.5 h the deposit shape is quite regular and presents a small peak around the stagnation point. The maximum angular position is about 40° but this is due to the particle starting location chosen for the simulation. As a matter of fact particles are uniformly distributed into some starting elements which do not cover the whole diameter of the tube (Figure 8.3), and this affects the maximum angular position of the deposit especially for the fraction related to particles with larger inertia.

To study the deposit shape as a function of the particle size, a second simulation using 25 μm particles was performed. Figure 8.8 and Figure 8.9 show the deposit shape and thickness after 3.5 h. In Figure 8.8 a) the deposit shape predicted in simulation B is compared to the deposit shape predicted in simulation A only considering the contribution given by 8 μm particles. Note that in both the cases the deposit is thinner at the stagnation point and thicker at its sides, according to the shape predicted in [83] (see also Figure 8.9), but the difference decreases as particle size increases. This confirms that the size classification given in [83] is probably too coarse to perform a good simulation.

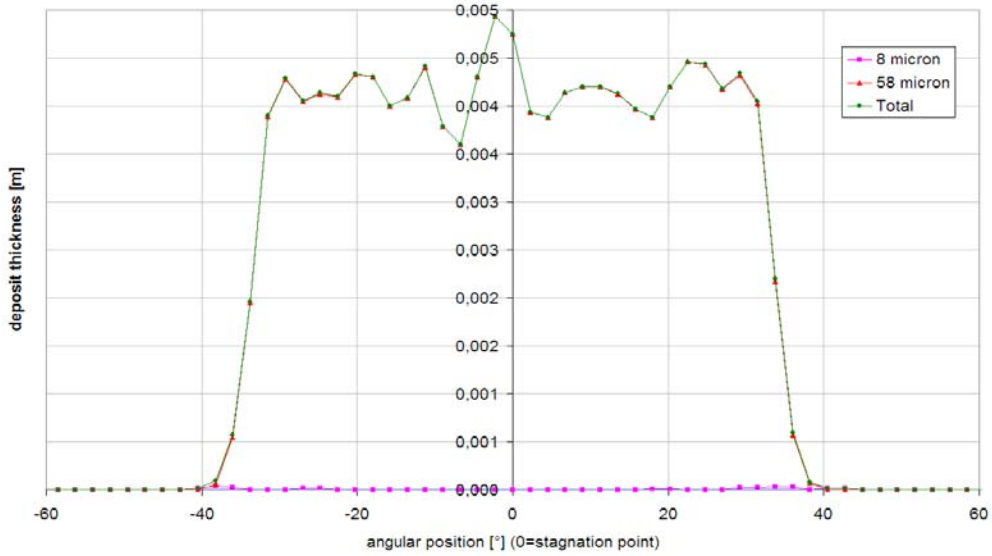


Figure 8.4 – Numerical prediction of deposit thickness after 3.5 h.

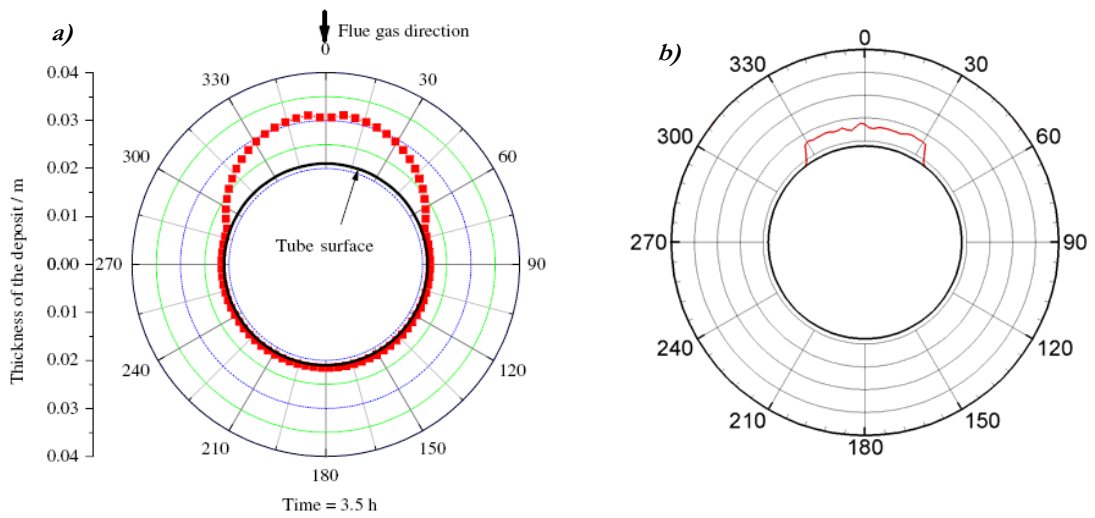


Figure 8.5 – Numerical prediction of deposit thickness after 3.5 h: a) Zhou et al. [83]; b) present simulation (simulation A).

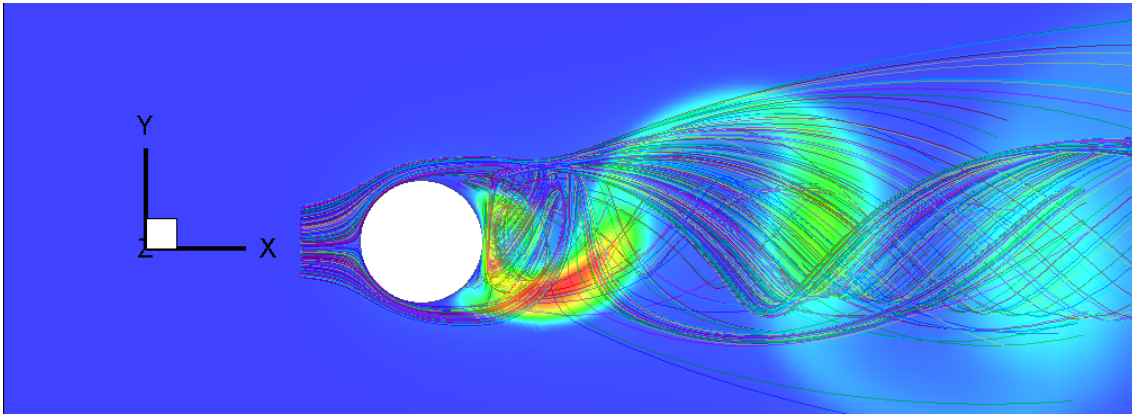


Figure 8.6 – Simulation A: particle trajectories.

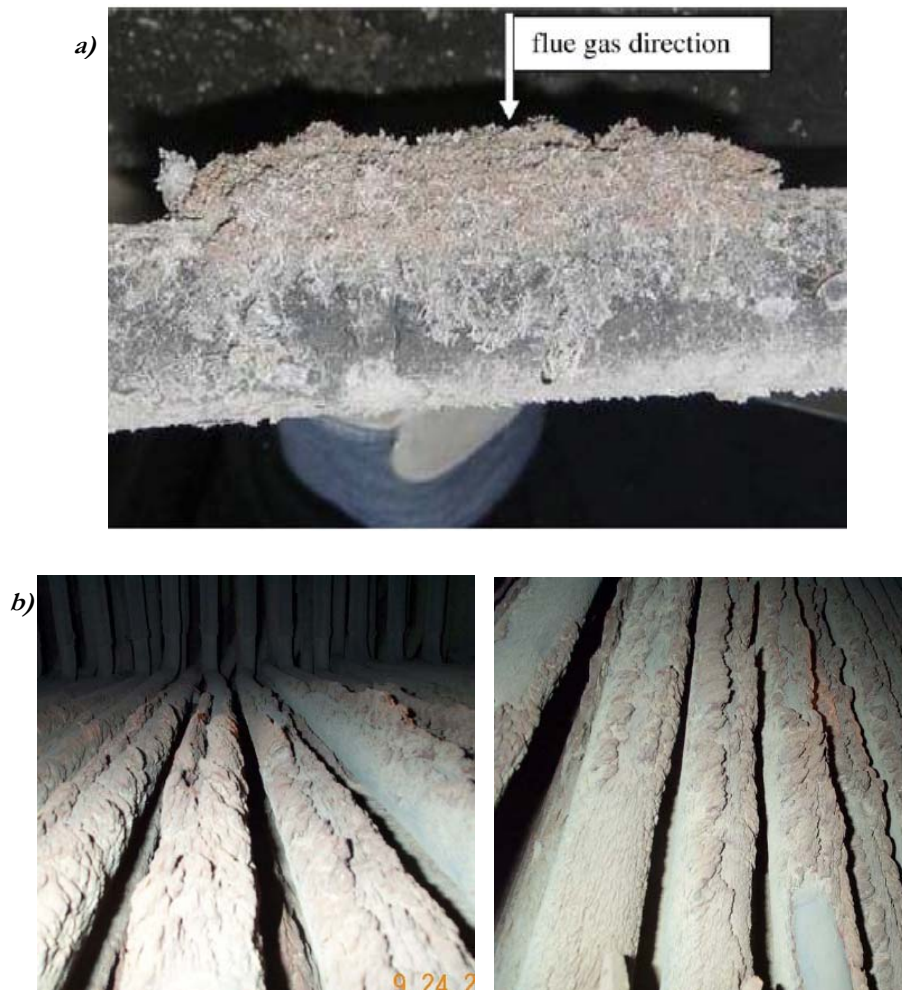


Figure 8.7 – a) Deposit shape after 3.5 h [83]; b) deposit shape in a biomass fed boiler [3].

In comparison with Figure 8.7, deposit predicted by simulation B better reproduces the real asperities. Figure 8.10 shows some particle trajectories of simulation B: comparing to trajectories in Figure 8.6, here particle trajectories are less dispersed. As a matter of fact, due to the increased size of particles the response time increases accordingly ($\approx 1.830E-03$ s), thus particles tend to separate from the streamlines and deposit on the cylinder.

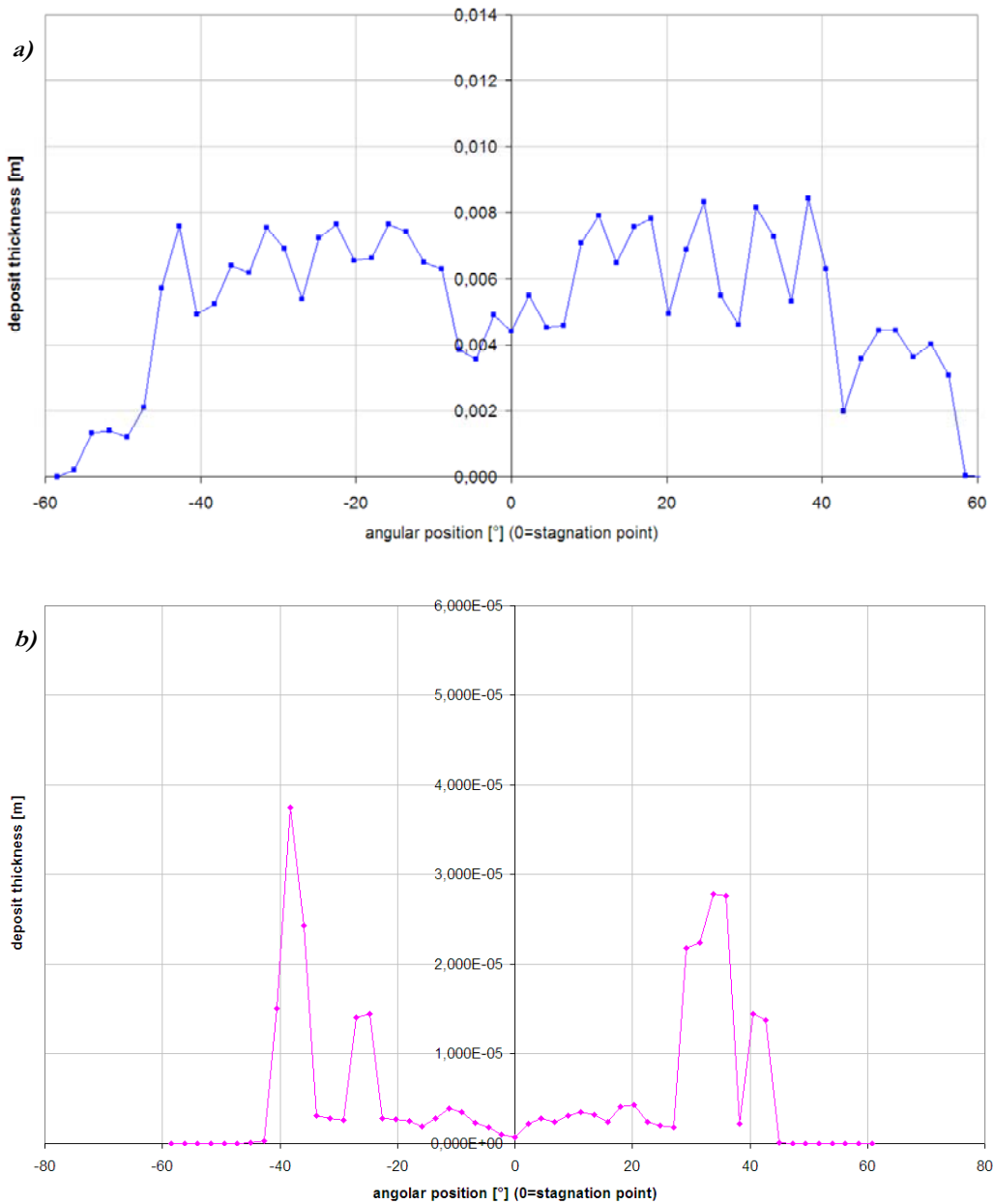


Figure 8.8 – a) Simulation B: deposit shape and thickness after 3.5 h; b) Simulation A: shape of the deposit due to 8 μ m particles, after 3.5 h.

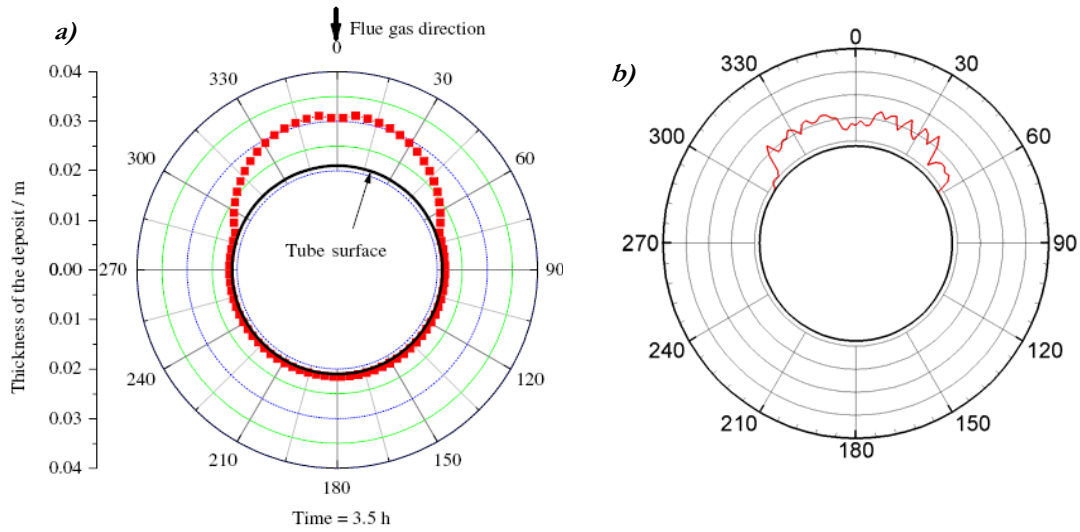


Figure 8.9 – Simulation B: deposit shape and thickness after 3.5 h.

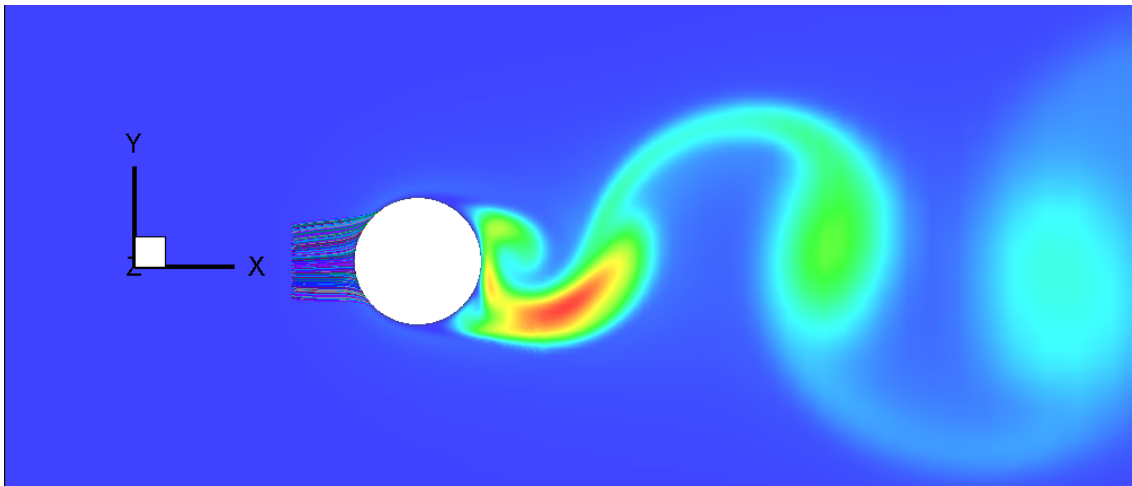


Figure 8.10 – Simulation B: particle trajectories.

According to the above considerations, a new simulation (simulation C, Table 8.2) was performed using a finer particle size classification. In this simulation particles are divided into three size classes (8, 25, and 58 μm). For the finest one the concentration is taken according with [83]. For both the remnant size classes (i.e., 25, and 58 μm) a concentration equal to $4.65\text{E-}4 \text{ kg/Nm}^3$, that is the half of that given in [83] for 58 μm particles, is assumed.

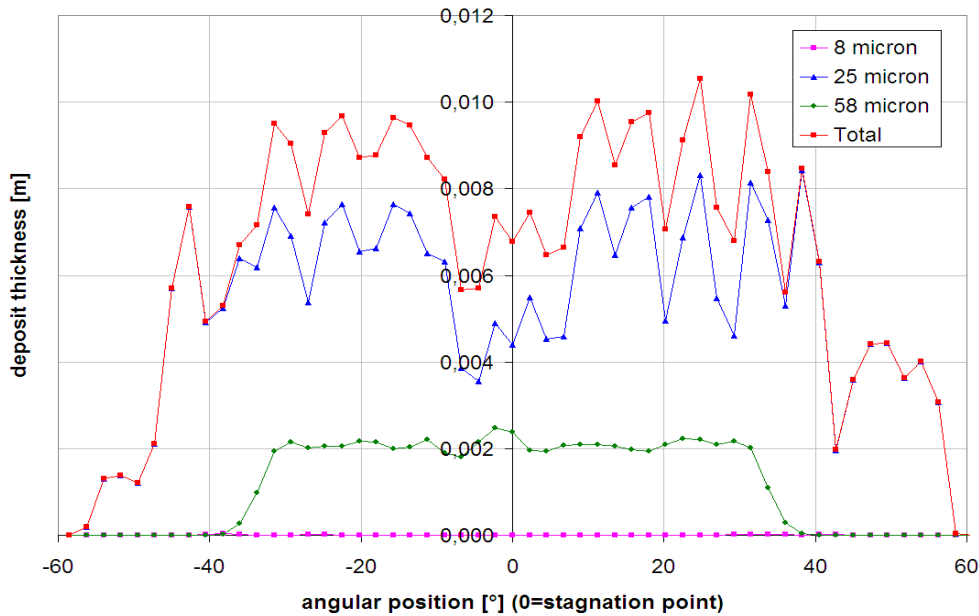


Figure 8.11 – Simulation C: deposit shape and thickness after 3.5 h.

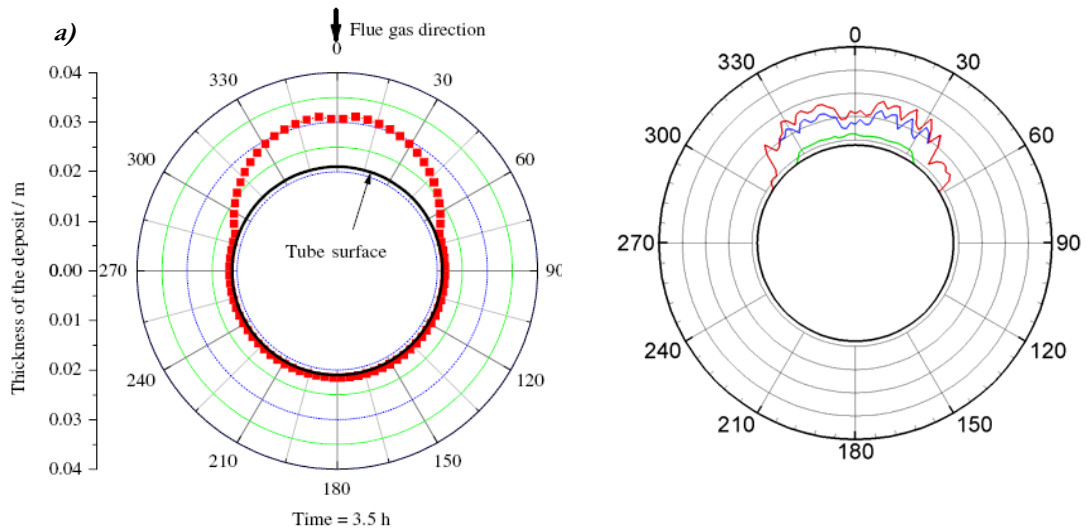


Figure 8.12 – Simulation C: deposit shape and thickness after 3.5 h.

Figure 8.11 and Figure 8.12 show the deposit shape and thickness after 3.5 h. It is evident that considering an intermediate size class of particles produce more realistic results. Deposit thickness after 3.5 h predicted by the present simulation is in better agreement with the results of Zhuo et al. [83], even if the predicted values are still a bit lower. Asperities in the deposit shape are present as in the real case, and the thickness at the stagnation point is lower than that at its sides. Figure 8.13 reports the deposit growth rate as predicted by simulation C.

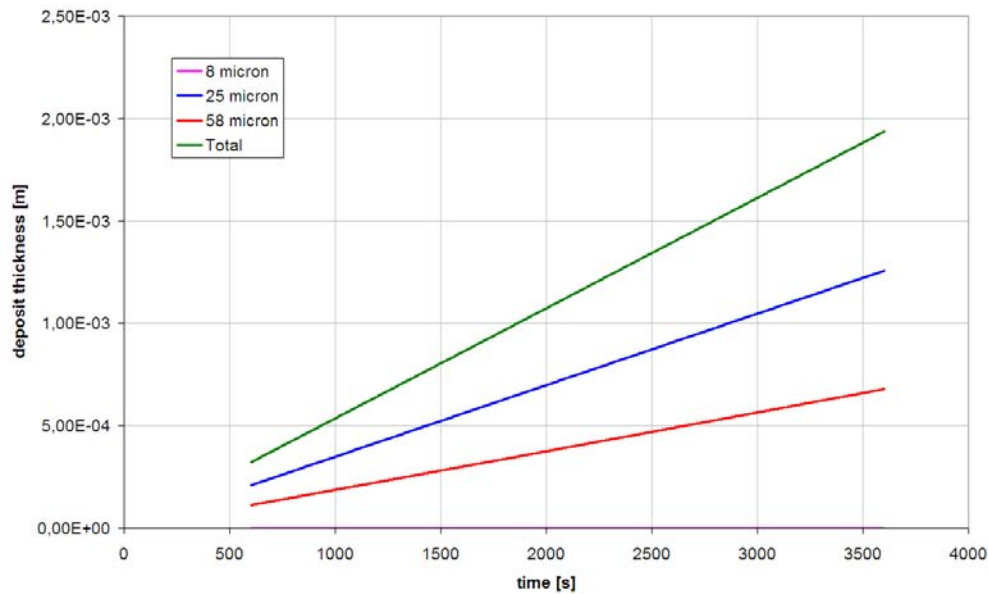


Figure 8.13 – Simulation C: deposit growth rate.

Summing up, simulation C, which used a finer particle size classification, produced results very alike to the real case. Differences in the shape and thickness can be ascribed to several factors. First of all Zhuo et al. [83] studied the deposit formation on a cylindrical probe inserted in a laboratory combustor which burns straw. Due to the nature of straw itself, fly ashes from straw combustion are partly cylindrical, thus this implies some differences in the particle motion and deposit formation and growth. Secondly a coarse size particle classification can affect the shape of the deposit because it neglects particle sizes which are important in simulation. Lastly the deposit growth provokes a modification in the flow field which can be accounted for only using a moving mesh approach.

8.2 Effect of the impact angle

In order to study the effect of the impact angle two different series of simulations have been performed. In the first one the particles enter the domain from just one element, while in the second one particles enter from 12 different elements. For both the series, simulations with and without impact angle effect have been performed; the adhesion criterion is that of critical viscosity, while the impact angle model is that proposed by Konstandopoulos [48]. Particles used in the two series are those of simulation B in the validation case (Table 8.2). Since the time evolution of the flowfield is represented by 37 realizations, and considering that at each new realization 100 particles per element enter the domain, in the first series of simulations the total amount of injected particles is 3700, while in the second series is 44400.

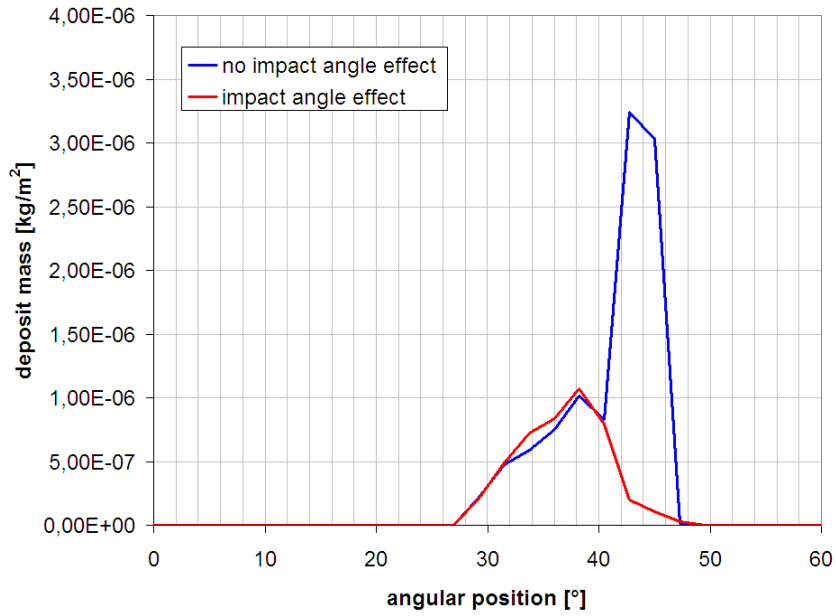


Figure 8.14 – Deposit mass on the cylinder when particles enters the domain from a single element (first series of simulations).

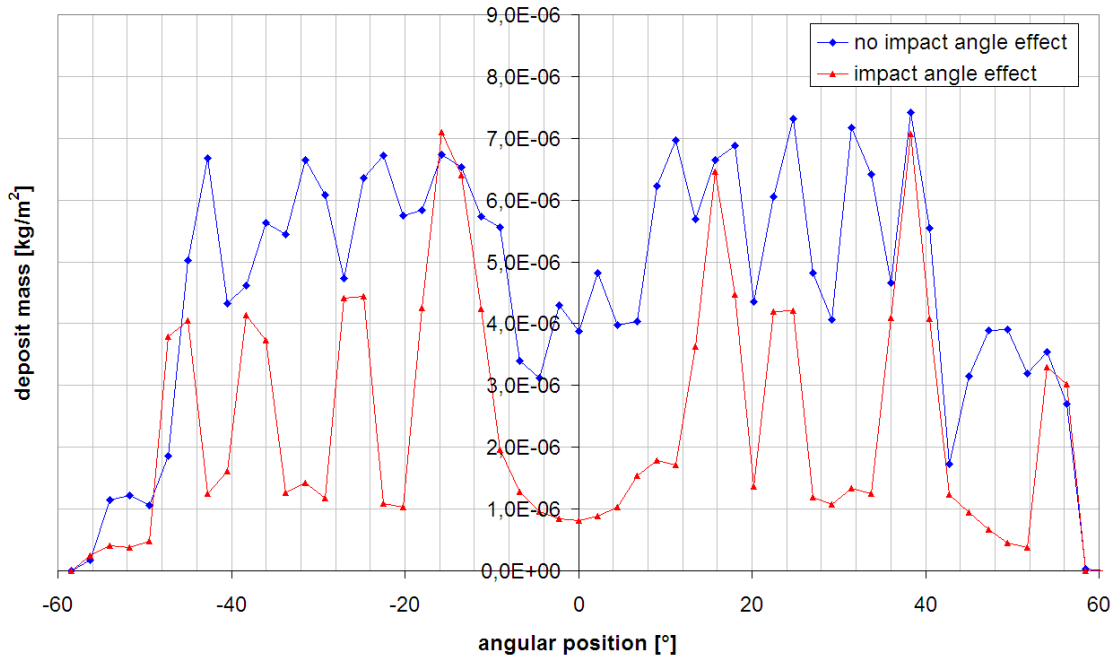


Figure 8.15 – Deposited mass on the cylinder when particles enter the domain from 12 different elements (second series of simulations).

Figure 8.14 shows results of the first series of simulations. Particles starting from the coloured element in Figure 8.16 deposit on a zone of the cylinder ranging from around 26° to 50° . It is readily seen that the effect of impact angle become important only at extreme angular positions: from 26° to 40° the deposited mass is practically the same, but for larger angular positions deposit is much smaller when the impact angle is considered. This can be easily explained considering that impact angle increases as particles impact the surface at extreme angular position. Thus beyond a certain angular position the impact angle overcomes the critical one and particles do not stick.

Figure 8.15 shows results of the second series of simulation. In this case (particles enter the domain from 12 different elements) the effect of impact angle is more complicate. The deposit mass curve as a function of the angular position shows a similar trend either considering or not the effect of impact angle: in both cases there are irregularities, and deposit on the stagnation point is smaller than that at its sides. In the simulation accounting for the impact angle, it is evident a general reduction in deposited mass, a part from few exceptions which can be ascribed to the fact that within a given element particles start from random positions. Focusing the attention to the angular position ranging from 26° to 50° , it can be seen that the profile is different from that predicted in the first series of simulations. This is probably due to the fact that now particles impacting the zone under consideration come from different elements, as sketched in Figure 8.16. Particles starting from elements closer to the cylinder axis (green lines in figure) impact the zone under consideration with a large impact angle which could be larger than the threshold value, thus they do not stick. On the contrary particles starting from more external elements (blue lines in figure) impact the same zone with a small impact angle, which could be smaller than the critical value, so they stick. Hence when particles start from different elements at the same time it results in a general reduction in deposit mass.

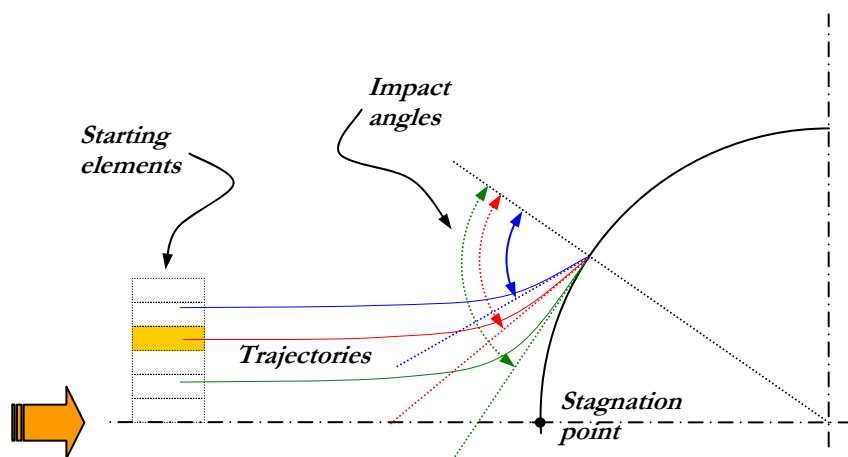


Figure 8.16 – Effect of the impact angle.

CHAPTER 9

Model application to a simple problem of industrial relevance

In the following paragraphs results produced by numerical simulations will be presented. They report the case of a wall bounded short cylinder immersed in a cross flow. They are based on both the PCT and SPT models (Chapter 1). Different adhesion models are compared.

9.1 Deposit on a wall bounded short cylinder

In this section results of wall deposition of particles in a turbulent flow over a single short cylinder bounded by end-walls are presented. Such a configuration is commonly found in plate-fin-and-tube heat exchangers.

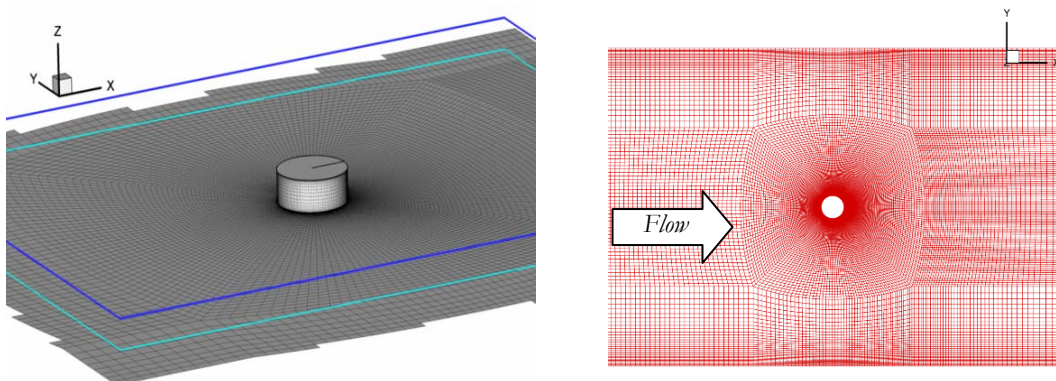


Figure 9.1 – Geometry of the domain.

The domain is composed by a short cylinder of diameter D and height $h = 0.4D$, bounded by flat end-walls (Figure 9.1), and it is divided into 647560 hexahedral elements, which correspond to 687582 nodes. Velocity field is simulated using LES approach [88]. The vortex shedding period is $T = 1.75$ s, which corresponds to 432 computational time steps. In order to simulate particle deposition 36 sequential realizations were extracted at every 10° ($\Delta\tau \approx 0.486$ s) and fed into the particle tracking/deposition code.

Deposit formation is simulated adopting different adhesion models, and comparing PCT approach with SPT. Spherical bronze particles with diameter of $50 \mu\text{m}$ are considered. Independently from the particle tracking approach the rationale of the simulation is illustrated in Figure 9.2. Name τ and t the partial and total simulation time. At the beginning of the simulation the first LES realization is taken as reference velocity field, particles (or clouds) are placed at the starting points and particle (or cloud) tracking/deposition simulation starts. It goes on, updating t and τ , until the latter reaches the value of $\Delta\tau$. At this point if the maximum simulation time is reached simulation ends, otherwise τ is set to zero and the next realization is loaded. If $t < 36 \Delta\tau$ new particles (or clouds) are placed at the starting points, and simulation continues; on the contrary no new particles (or cloud) are added and simulation those already entered within the domain.

Particle number depends on the particle tracking models used. In PCT simulation 12 clouds, each containing 1000 particles and starting from a different element, enter the domain at each new realization according to the rationale illustrated above. Thus a total of 432 clouds starting from 12 different positions are simulated, with 432000 particles in total. On the contrary in single particle simulations 1800 particles, uniformly divided on the 12 different starting elements, enter the domain at each new realization. Thus a total of 64800 particles are simulated. The number is limited by computational limits.

The main difference between PCT and SPT approaches is evident: the former allows the simulation of a huge number of particles distributed in a limited number of clouds, the latter has to deal with computation limits.

9.1.1 Results

Preliminary results are presented in [89], [90].

In Figure 9.3 a snapshot of the flow field, identified by streamlines on three different sections, is depicted. Before the cylinder flow shows an almost laminar behaviour which drastically change close to the cylinder. Two horse shoe vortexes, in proximity of the two walls, form and develop around the cylinder. On the back side of the cylinder a recirculation take place and the wake forms and starts to oscillate.

Figure 9.4 reports some sample of cloud trajectories (coloured lines), the time evolution of a cloud size, and the *pdf* at two different time instants. As shown in the figure clouds starts having small size (initial diameter is set equal to $0.02D$) which does not increase sensitively until clouds cross the cylinder. This is due to the fact that flow before the cylinder has very low turbulence, thus recalling expression of σ (1.25), particles within a cloud are not dispersed. After the cylinder, where the wake develops, turbulence increases as well as the cloud size. Accordingly *pdf* flatten as clouds become larger.

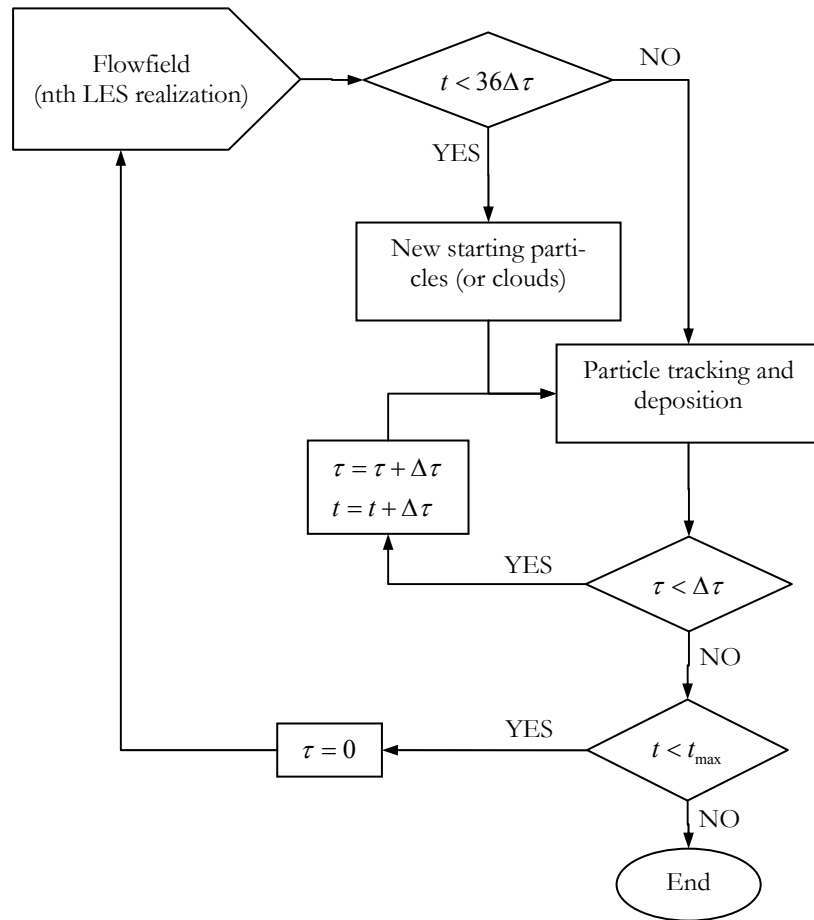


Figure 9.2 – Rationale of the simulations.

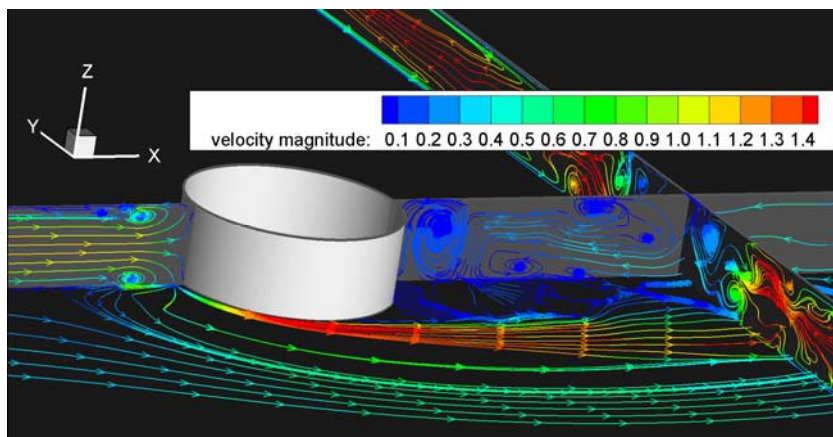


Figure 9.3 – A snapshot of streamlines in three planes ($z/Z_{max}=0.05$, $y/Y_{max}=0.5$, $x/X_{max}=0.6$) coloured by the velocity module.

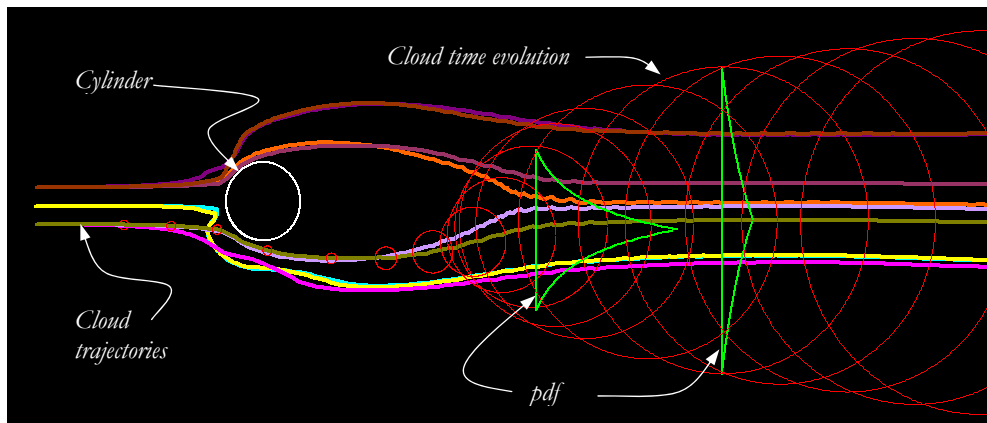


Figure 9.4 – Sample cloud trajectories, time evolution of a cloud (red circles), and pdf at two different time steps (green lines).

In Figure 9.5 turbulence structures around the cylinder, identified by pressure Laplacian, and some cloud trajectories are reported. Before the cylinder trajectories follow the streamlines (see also Figure 9.4) but as soon as they approach the cylinder most of them are captured by the two horse shoe vortices which form close to the cylinder. Therefore trajectories rotate around it and spread.

Figure 9.6 shows some clouds and particles trajectories starting from two different elements: yellow lines represent clouds trajectories, and green lines represent the particles one. All of them start from the same element. As evident from figure, cloud trajectories are quite different from that of particles. In particular single particles are more sensitive to the horse shoe vortices whilst clouds follow all a similar trajectory. Besides clouds seem not to be very affected by the recirculation zone behind the cylinder although some trajectories are attracted by this zone. On the contrary single particles show a prompt response going backward to the cylinder. This different behaviour is due to the average nature of STP model: as a matter of fact since the cloud velocity is computed by taking into account the weighted contribution of all the particles, local effects are inevitably smoothed by the cloud effect, and larger the cloud more smoothed the local effects.

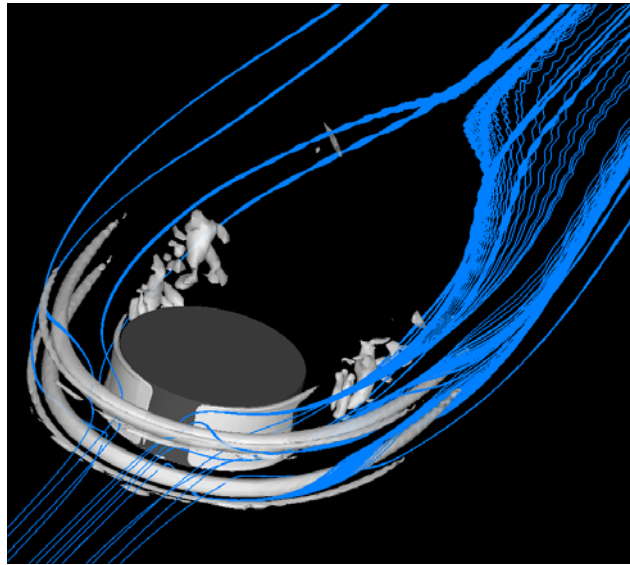


Figure 9.5 – Turbulence structures (here indicated in white and identified by pressure Laplasian) and trajectories of the clouds.

Deposits predicted by PCT and SPT models are compared in Figure 9.7. The Zhang et al. adhesion model ([65], section 4.1.1) based on the ratio between adhesion and rolling moment (RM) is adopted. Actually the Zhang et al. models (RM in the following) was developed with the aim of modelling the re-suspension of deposited particles, thus using it as adhesion model is not completely proper. On the other hand since it takes into account adhesion and drag forces, in a rough approximation it could be also used as an adhesion model. Accepting this approximation means neglecting the dynamics of impact because in the RM model particle are subjected nothing else but the gravitational force, and the deformation are due only to this force.

On the (top and bottom) left side of Figure 9.7 the PCT approach is reported in two different point of view, and on the (top and bottom) right side SPT approach in the same views is reported. Deposit predicted by the two models are coherent but different. Comparing the two sides of the figure is evident that PCT provide a continuous deposit contour due not only to the different number of particles simulated in the two models, but also to the fact that particle distribution within a cloud is continuous. In both cases deposit forms mainly along the horse shoe vortexes which capture trajectory of both the single particle and clouds. Analysing the deposit formed close to the cylinder is evident that the one produced by the SPT approach is much larger than that form PCT. This agrees with the grater spread of single particle due to horse shoe vortexes said above. For the same reason PCT does not provide any deposit on the recirculation zone close to the cylinder as indeed SPT model does. To better fit the single particle results fundamental quantities in PCT model are the initial cloud size and number. A PCT simulation with a lot of small clouds becomes similar to the SPT simulation but conserves the advantages of the STP approach. An optimization of this two quantities has to be found.

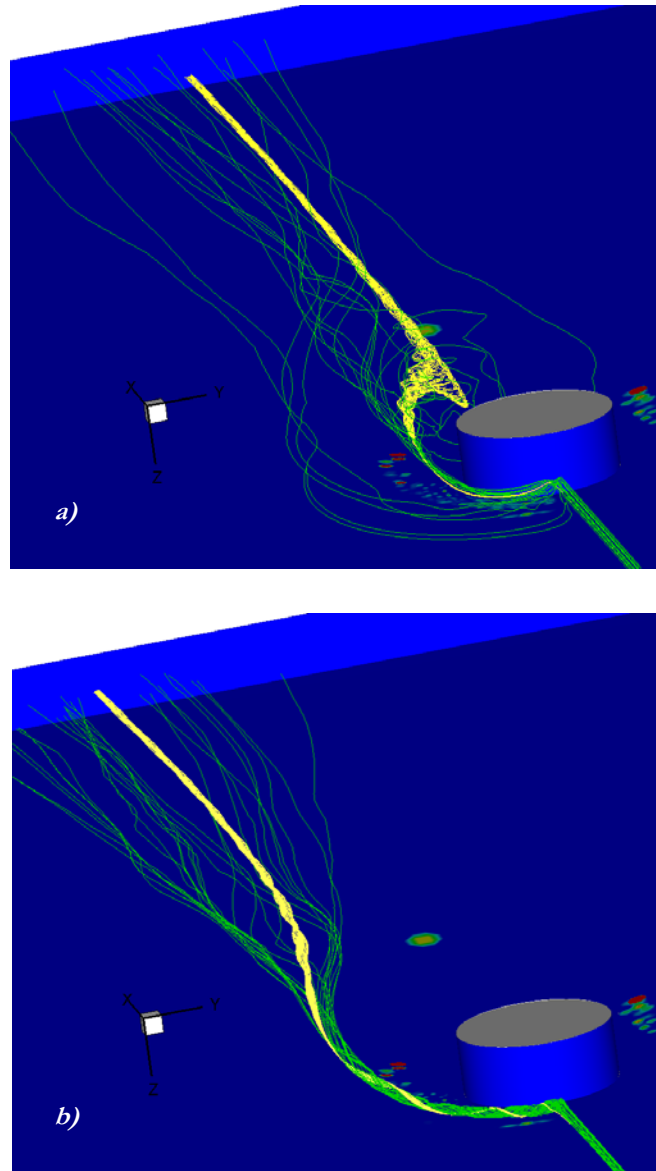


Figure 9.6 – Cloud (yellow lines) and particles (green lines) trajectories starting from two different elements.

RM, van Beek (vB), Thornton and Ning (TN), and Feng et al. (FA) adhesion models are compared in Figure 9.8. Details of the last three models are reported in Chapter 4; the first one is analysed in Chapter 5. Figure 9.8 demonstrates that all the models returns similar qualitatively results, with some differences especially in the recirculation region. In this region the *RM* solution (Figure 9.8 a) returns less deposit if compared with impact models. This is probably due to the fact that, as said before, *RM* is a model to account for the re-suspension of particles and we used it just as a rough approximation to predict the deposit. In fact recalling the expression of *RM* given in equation (5.7), or in (5.8) reported below

$$RM = \frac{F_D (1.399R - \delta)}{(F_A + F_G + F_{BU} + F_L) a} > 1$$

and that in *RM* model the contact radius is $a = (2\Gamma R/H)^{1/2}$, which is the deformation due to the contact force which rises when a particle lies on a surface, no impact is thus considered as well as the effect of elasto-plastic deformation. Therefore it is much easier that a particle can rebound from the surface reducing the overall amount of deposit in regions where only a small fraction of particles (with respect to the total amount) is transported.

As far as the *FA* model (Figure 9.8 d) is concerned the deposit in this case is similar to that predicted using *RM* model. In this case impact is accounted for but just the elastic phase, hence even in this case elasto-plastic deformation are not considered and particles are more prone to rebound.

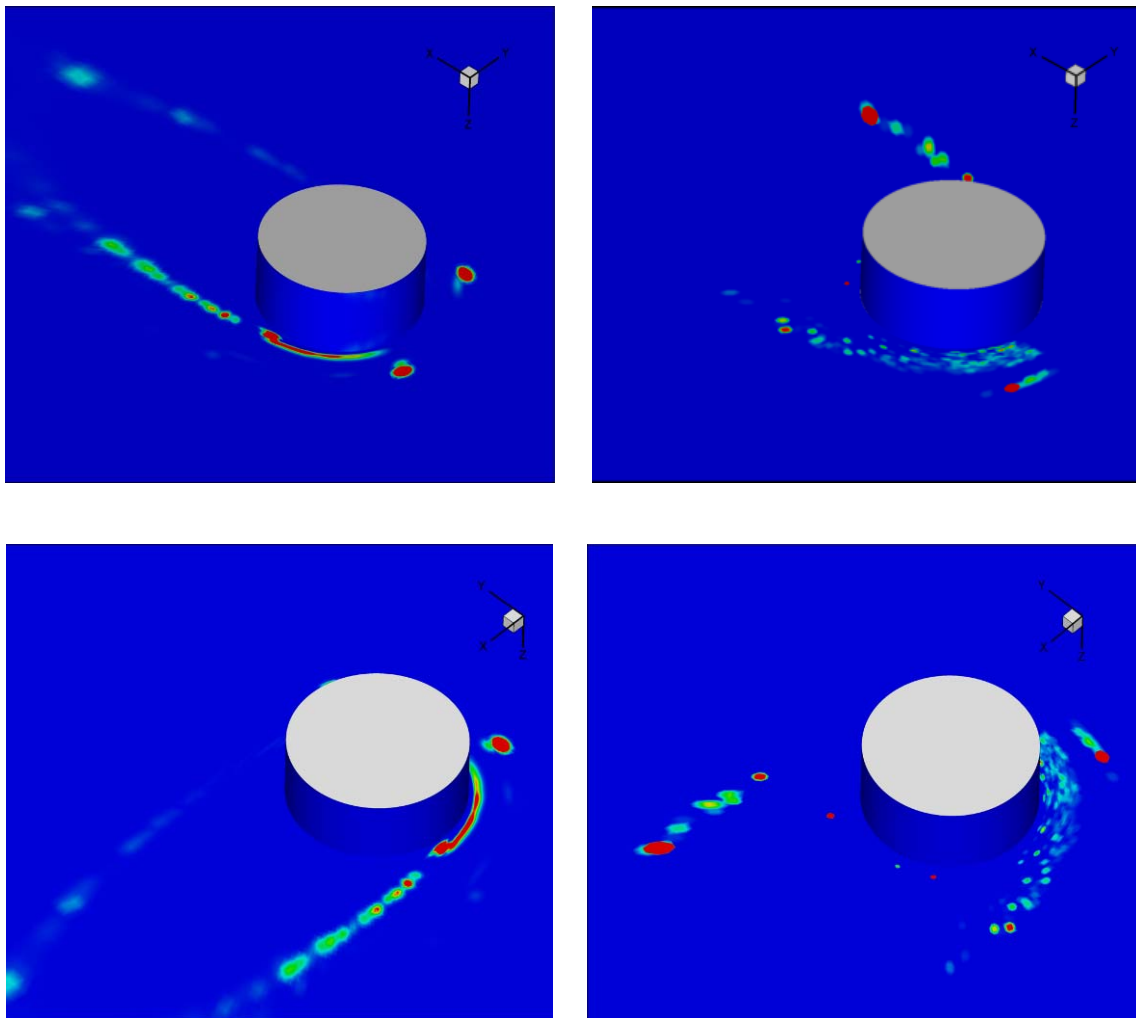


Figure 9.7 – Deposit predicted using *RM* criteria: left - *STP* model; right – single particle model; top and bottom: two different points of view.

The best models from a physical point of view are the vB and TN ones (Figure 9.8 b and c). They show a bit larger amount of deposit especially in the recirculation zone. TN model in particular is the one which predicts the largest amount of deposited particles and the only one which predict a deposition even on the cylinder surface. Since in actual applications fouling on cylinders surface occurs even in the recirculation side, from this preliminary results seems that TN model is the one which predict more realistic results.

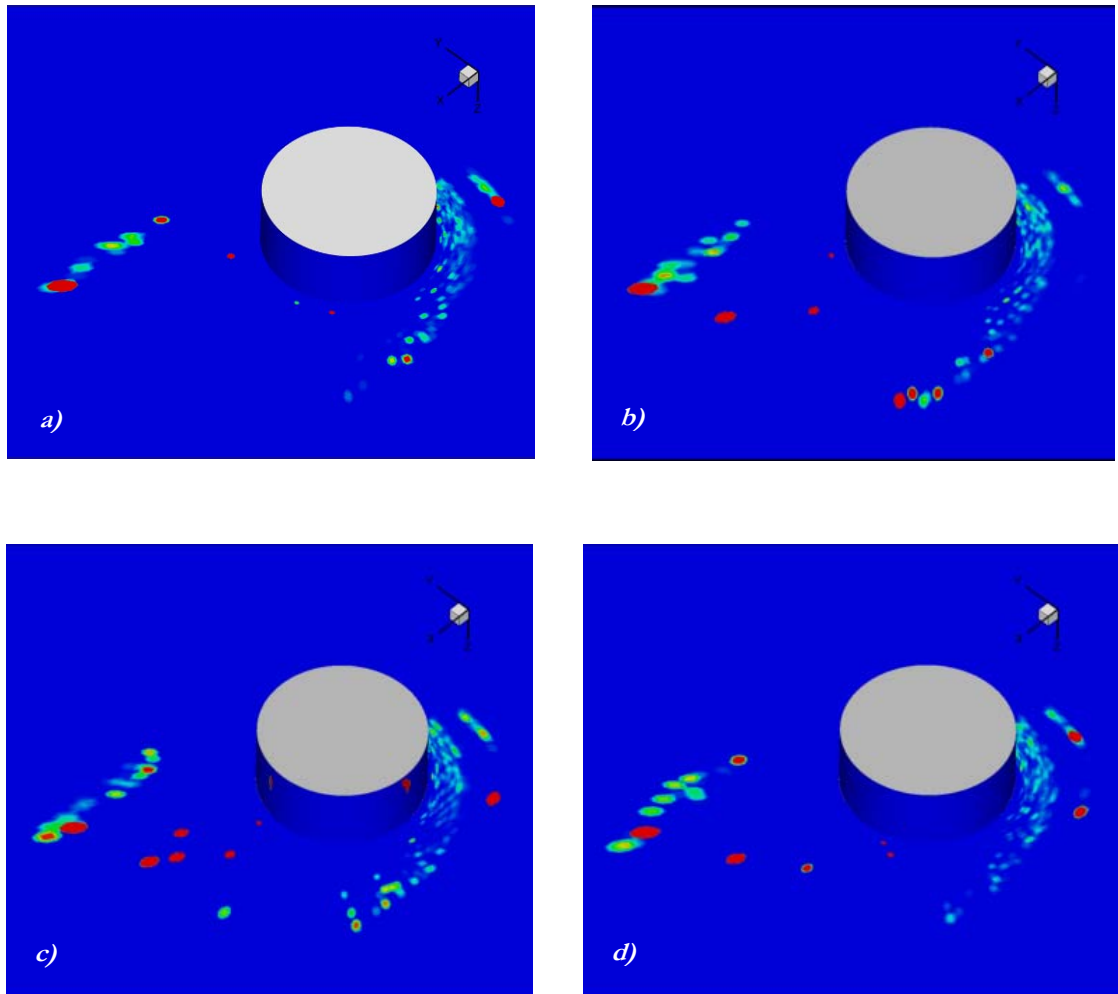


Figure 9.8 –Comparison of particle deposit using single particle approach and several adhesion criteria: a) RM; b) Van Beek; c) Thornton and Ning; d) Feng et al..

CHAPTER 10

Conclusions

The aim of this work was to develop a numerical model which, used in conjunction with a CFD code, can predict the formation of deposit of solid particles on surfaces as encountered in biomass-fired boilers and auxiliary equipment. Specifically, the target is to predict the dynamics of deposit formation (the growth rate and the shape of the deposit) on the furnace interior walls, but also (and even more importantly) on tubes and bounding walls of superheaters, heat exchangers and other equipment in which the boiler flue gases are used or processed. In these applications particles are mainly in the supermicron size range where inertia is the most important deposit mechanism. Thus this work is focused on this mechanism.

In developing a model to predict the inertia dominated deposit process, several aspects and issues have to be accounted for. First of all a model is needed for simulating *transport of particles entrained by fluid flow and their dispersion due to turbulence*. In this work two different approaches were adopted: the SPT and the PCT [21] models. Both are based on the BBO equation but the latter model solves an averaged equation for the cloud centres. Of course the STP is more exact and allows to better model and understand the effect of the various phenomena involved in transport, impact and adhesion of particles. Although the PCT approach is very appealing because one can handle a very large number of particles tracking few trajectories, some shortcomings have been pointed out in this work, i.e. the smoothing of the local velocity effect, and the dependence on the number, distribution and initial size of the clouds. A modified version of the PCT model was proposed to take into account the local velocity, but the crucial issue is the choosing of the right number of clouds, their starting point and their initial size. Due to its averaging nature PCT model seems to be more indicative for RANS flow fields than for LES ones, or in the case that a qualitative prediction of deposit suffices. Moreover since applying SPT model to industrial flows, characterised by large domains and number of particles, is too computational demanding, the PCT could be a possible alternative, but it should be used with caution and care.

Next point is the modelling of *impact/adhesion* mechanics. In order to better study this aspect, which is the focus of this work, several models have been analysed and compared. As for the normal impact/adhesion the vB [36], T&N [37], and FA [42] models have been studied. It results that vB and TN better describe and model the phenomenon, and seem to predict more realistic deposits. The FA model can be used as a rough approximation, thus just to identify the zones within a device which are at higher risk of deposit formation.

The analysis of the effect of *impact angle* showed that the presence of a tangential force results in a reduction of the contact area and thus of the net adhesion energy. However it has been demonstrated that this effect becomes appreciable only for high impact angles (greater than about 70°). Therefore, the Konstandopoulos model [48], which introduces a critical impact angle above which particles do not stick anyway, is adopted. A series of simulations have then been performed and it comes out that the effect of the impact angle is a global reduction of deposit.

In this work *re-suspension* was analysed considering the *RM* [65] and Ziskind [71] models. These models are similar, both being based on the force and moment balance, but Ziskind deepens the analysis and gives a condition for re-suspension which is less restrictive than that in *RM* model.

In the analysis of *deposit growth* the focus on the effect of *particle packing* during deposit formation shows that the net adhesion energy increases with the number of deposited particles, becoming larger once the first layer of deposit is formed. This is due to the fact that particle impacting a deposit layer undergoes multiple contacts (i.e., with the surface and/or with other deposited particles). The augmented net adhesion energy results in an increasing of the sticking velocity, that is particles which would not have stuck to a clean surface, can stick to it if even a partial deposit layer is already formed. The presence of a deposit layer and multiple contacts between deposited particles, influences also the re-suspension phenomenon. A particle stuck to a surface is more prone to be re-entrained by the flow in the case that it is isolated rather than when it is within a deposit layer. As a matter of fact the presence of multiple contacts introduces new forces and change the moment balance. The study has shown that this results in a reduction of the *RM*, that is in the same flow conditions, particles re-suspension occurs with more difficulty.

Assuming that during the deposition process particles place themselves according to hexahedral packing pattern, it is also possible to compute the *deposit thickness*. This approach has some limits due to the random size distribution of particles carried by a flow. Besides, permanent deformations that particles undergo during the impact can affect the packing and hence the thickness. Therefore also a more engineering (and affordable) model, based on the deposit bulk density, was proposed.

The above mentioned models were *implemented into the code* for deposit prediction, and several simulations were performed. The code was validated referring to the study of Zhou et al. [83]. The simulation revealed that the code *can predict deposit shapes* very alike to the real situation, but some factors (i.e., particle shape, particle size distribution, deposition rate) are important to provide the desired fidelity in predictions. The *shape of particles* is important, but all the models assume spherical particles. Thus if the real particles are cylindrical or differently shaped it could compromise the simulation. In any case the simulation performed to validate the code, showed good agreement with the reference study even if in this case some non-spherical (but elongated, cylindrical-like) particles are surely present. Another important factor is the *particle size distribution*: a coarser size classification affects the prediction. Larger particles have higher response time so they leave the streamlines of the flow, and deposit on surfaces, more easily than the smaller ones. Therefore if the particle size classification is coarse, simulations can provide unrealistic results. The same can occur in the case of high deposition

rate. In this case the flow field could change rapidly, requiring a modification of the computational mesh.

The Impact angle effect and re-suspension need further studies, and so does the effect of the particle packing within a deposit layer. This latter aspect can be very important in predicting the particle deposition and deposit growth, as discussed in Chapter 6. This, however, brings in more complexities and require further theoretical and most of all experimental studies.

References

- [1]. T.R. Miles, T.R. Miles Jr, L.L. Baxter, R.W. Brayers, B.M. Jenkins, L.L. Olden. Boiler deposits from firing biomass fuels. *Biomass and Bioenergy* (1996), 10, 125-138.
- [2]. L.L. Baxter, T.R. Miles, T.R. Miles Jr, B.M. Jenkins, T. Milne, D. Dayton, R.W. Brayers, L.L. Olden. The behaviour of inorganic material in biomass-fed power boilers: field and laboratory experience. *Fuel Processing Technology* (1998), 54, 47-78.
- [3]. D.A. Tillman. Practical applications of ash chemistry in combustion systems. Foster Wheeler Power Group, inc. 2002.
- [4]. R.W. Bryers. Fireside slagging, fouling, and high-temperature corrosion of heat-transfer surface due to impurities in steam-rising fuels. *Progress in Energy and Combustion Science* (1996), 22, 29-120.
- [5]. C.T. Crowe, E.E. Mechaelides. Basic concepts and definitions. In *Multiphase Flow Handbook*, Edited by C.T. Crowe, Taylor & Francis, Boca Raton, 2006.
- [6]. LL. Baxter. Ash deposition during biomass and coal combustion: a mechanistic approach. *Biomass and Bioenergy* (1993), 4(2), 85-102.
- [7]. S.K. Kær. *Numerical investigation of ash deposition in straw-fired boilers*. Ph.D. dissertation, Institute of Energy Technology, Aalborg University, Denmark, October 2001.
- [8]. L. Talbot. Thermophoresis of particles in a heated boundary layer. *Journal of Fluid Mechanics* (1980), 101(4), 737-758.
- [9]. I. Oberberger. Aerosols in fixed-bed biomass combustion. Bio-Energy Enlarged Perspectives, Budapest 16-17 October 2003.
- [10]. J. Kurkela, J. Latva-Somppi, U. Tapper, E.I. Kauppinen. Inorganical aerosol formation and deposition during fluidized bed of biomasses and wood waste. *Journal of Aerosol Science* (1997), 28(Suppl. 1), S415-S416.
- [11]. J.K Jokiniemi, T. Lind, J. Hokkinen, J. Kurkela, E.I. Kauppinen. Modelling and experimental results on aerosols formation, deposition, and emissions in fluidized bed combustion of biomass. In *Aerosols from biomass combustion*. T. Nussbaumed Ed., International Seminar: IEA BioenergyTask 32: Biomass combustion and Cofiring. Zurich, 27 June 2001.
- [12]. M. Sommerfeld, B. van Wachem, R. Oliemans. *Best practice guidelines*. ERCOFTAC Special Interest Group on “Dispersed Turbulent Multi-Phase Flow”. Version 20-08-2007.

- [13]. M.R. Maxey, J.J. Riley. Equation of motion for a small rigid sphere in a nonuniform flow. *Physics of Fluids* (1983), 26 (4), 883-889.
- [14]. A. Barlemont, P. Desjonqueres, G. Gouesbet. Particle Lagrangian simulation in turbulent flows. *International Journal on Multiphase Flows* (1990), 6 (1), 19-34.
- [15]. J.W. Brooke, K. Kontomaris, T.J. Hanratty. Turbulent deposition and trapping of aerosols at wall. *Physics of Fluids* (1992), A4 (4), 825-834.
- [16]. C.T. Crowe, T.R. Troutt, J.N. Chung. Numerical models for two-phase turbulent flows. *Annual Review of Fluid Mechanics* (1996), 28, 11-43.
- [17]. V. Armenio, V. Fiorotto. The importance of the forces acting on particles in turbulent flows. *Physics of Fluids* (2001), 13 (8), 2437-2440.
- [18]. J.S. Shirolkar, C.F.M. Coimbra, M. Queiroz McQuay. Fundamental aspects of modelling turbulent particle dispersion in diluted flows. *Progress in Energy and Combustion Science* (1996), 22, 363-399.
- [19]. J.S. Shuen, L.D. Chen, g.M. Faeth. Evaluation of a stochastic model of particle dispersion in a turbulent round jet. *AIChE Journal* (1983), 29 (1), 167-170.
- [20]. A.A. Mostafa, H.C. Mongia. On the interaction of particles and turbulent fluid flow. *Journal of Heat and Mass Transfer* (1988), 34 (10), 2063-2075.
- [21]. L.L. Baxter. *Turbulent transport of particles*. Ph.D. Thesis, Brigham Young University, 1989.
- [22]. K. Hanjalić, M. Sijerčić. Application of computer simulation in a design study of a new concept of pulverized coal gasification. *Combustion Science and Technology* (1994). Part I: Rationale of the concept and model of hydrodynamics and heat transfer, 97, 331-350. Part II: Model of Coal Reaction and Discussion of Results, 97, 351-376, 1994.
- [23]. P. Venturini, D. Borello, C.V. Iossa, D. Lentini, F. Rispoli. Modelling of multiphase combustion and deposit formation and deposit formation in a biomass-fed boiler. *Energy* (2010), 35, pp. 3008-3021.
- [24]. C.V. Iossa, D. Lentini, F. Rispoli, P. Venturini. Combustion modelling in a biomass-fed furnace. International Symposium on Convective Heat and Mass Transfer in Sustainable Energy (CONV-09). April 26th-May 01st, 2009, Hammamet, Tunisia.
- [25]. I. Oberberger. Aerosols in fixed-bed biomass combustion. Bio-Aerosols, Bio-Energy Enlarged Perspectives, October 16th-17th, 2003, Budapest.
- [26]. W. Cheng, R.M. Brach, P.F. Dunn. Three-Dimensional modelling of microspheres contact/impact with smooth, flat surfaces. *Aerosol Science and Technology* (2002), 36, 1045-1060.
- [27]. K.L. Johnson, K. Kendall, A.D. Roberts. Surface Energy and the contact of elastic solids. *Proceedings of the Royal Society of London* (1971), series A 324, 301-313.
- [28]. A.D. Roberts. Ph.D. dissertation, Cambridge University, England (1968).
- [29]. K. Kendall. Ph.D. dissertation, Cambridge University, England (1969).
- [30]. L.N. Rogers, J. Reed. The adhesion of particles undergoing an elastic-plastic with a surface. *Journal of Physics D: Applied Physics* (1983), 17, 677-689.
- [31]. S. Wall, W. John, H.-C. Wang. Measurements of kinetic energy loss for particles impacting surfaces. *Aerosols Science and Technology* (1990), 12, 926-946.

- [32]. R.M. Brach, P.F. Dunn. A mathematical model of the impact and adhesion of microspheres. *Aerosol Science and Technology* (1992), 16, 51-64.
- [33]. B. Dahneke. Particle bounce or capture – Search for an adequate theory: I. Conservation-of-energy model for a simple collision process. *Aerosol Science and Technology* (1995), 23, 25-39.
- [34]. N. Maw, J.R. Barber, J.N. Fawcett. The oblique impact of elastic spheres. *Wear* (1976), 38, 101-114.
- [35]. M. Xu, K. Willeke, P. Biswas, S.E. Pratsinis. Impaction and rebound of particles at acute incident angles. *Aerosol Science and Technology* (1993), 18, 143-155.
- [36]. M.C. van Beek. *Gas-side fouling in heat-recovery boilers*. Ph.D. Technische Universiteit Eindhoven, Germany, 2001.
- [37]. C. Thornton, Z. Ning. A theoretical model for stick/bounce behaviour of adhesive, elastic-plastic spheres. *Powder Technology* (1998), 99, 154-162.
- [38]. K.L. Johnson. Adhesion at the contact of solids. *Theoretical and Applied Mechanics* (1976), 133-143.
- [39]. J.G.A. Bitter. A study of erosion phenomena part I. *Wear* (1963), 6, 5-21.
- [40]. C. Thornton. Coefficient of restitution for collinear collision of elastic-perfectly plastic spheres. *Journal of Applied Mechanics* (1997), 64, 383-386.
- [41]. C. Hardy, C.N. Baronet, G.V. Tordion. The elasto-plastic indentation of a half-space by a rigid sphere. *International Journal of Numerical Methods in Engineering* (1971), 3, 451-462.
- [42]. X.-Q. Feng, H. Li, H.-P. Zhao, S.-W. Yu. Numerical simulations of the impact of adhesive microparticles with a rigid substrate. *Powder Technology* (2009), 189, 34-41.
- [43]. R.D. Mindlin, H. Deresiewicz. Elastic spheres in contact under varying oblique forces. *Journal of Applied Mechanics* (1953), 75, 327-344.
- [44]. A.R. Savkoor, G.A.D. Briggs. Effects of tangential force on contact of elastic solids in adhesion. Proceedings of the Royal Society of London. Series A (1977), 356, 103-114.
- [45]. C.-Y. Wu, C. Thornton, L.-Y. Li. Coefficients of restitution for elastoplastic oblique impacts. *Advanced Powder Technology* (2003), 14, 435-448.
- [46]. C. Thornton. Interparticle sliding in the presence of adhesion. *Journal of Applied Mechanics* (1991), 24, 1942-1946.
- [47]. D.A. Gorham, A.H. Kharaz. The measurement of particle rebound characteristics. *Powder Technology* (2000), 112, 193-202.
- [48]. A.G. Konstandopoulos. Particle sticking/rebound criteria at oblique impact. *Aerosol Science* (2006), 37, 292-305.
- [49]. G.P. Broom. Adhesion of particle in fibrous air filter. *Filtration and Separation* (1979), 16, 661-669.
- [50]. X. Li, P.F. Dunn, R.M. Brach. Experimental and numerical studies of microsphere oblique impact with planar surface. *Journal of Aerosol Science* (2000), 32 (5), 583-594.
- [51]. R.M. Brach, P.F. Dunn. Macrodynamics of microparticles. *Aerosol Science and Technology* (1995), 23, 51-71.
- [52]. R.M. Brach, P.F. Dunn. Models of rebound and capture for oblique microparticle impacts. *Aerosol Science and Technology* (1998), 29, 379-388.

- [53]. R.A. Wessel, J. Righi. Generalized correlations for inertial impaction of particles on a circular cylinder. *Aerosol Science and Technology* (1988), 9, 29-60.
- [54]. J. Young, A. Leeming. A theory of particle deposition in turbulent pipe flow. *Journal of Fluid Mechanics* (1997), 340, 129-159.
- [55]. P.M. Walsh, A.N. Styre, D.O. Loehden, L.S. Monroe, J.M. Beer, A.F. Sarofim. Deposition of bituminous coal ash on an isolated heat exchanger tube: effect of coal properties on deposit growth. *Progress in Energy and Combustion Science* (1990), 16, 327-346.
- [56]. F.C.C. Lee, F.C. Lockwood. Modelling ash deposition in pulverized coal-fired applications. *Progress in Energy and Combustion Science* (1999), 25, 117-132.
- [57]. G.H. Richards, P.N. Slater, J.N. Harb. Simulation of ash deposit growth in a pulverized coal-fired pilot scale reactor. *Energy and Fuels* (1993), 7, 774-781.
- [58]. L.Y. Huang, J.S. Norman, M. Pourkashanian, A. Williams. Prediction of ash formation on superheater tubes from pulverized coal combustion. *Fuel* (1996), 75(3), 271-279.
- [59]. C.L. Senior, S. Srinivasachar. Viscosity of ash particles in combustion system for prediction of particle sticking. *Energy and Fuels* (1995), 9, 277-283.
- [60]. H. Wang, J.N. Harb. Modelling of ash deposition in large-scale combustion facilities burning pulverized coal. *Progress in Energy and Combustion Science* (1997), 23, 267-282.
- [61]. A.H. Ibrahim, P.F. Dunn, R.M. Brach. Microparticle detachment from surfaces exposed to turbulent air flow: controlled experiments and modelling. *Aerosol Science* (2003), 34, 765-782.
- [62]. M.J. Corn. The adhesion of solid particles to solid surfaces II. *Journal of the Air Pollution Control Association* (1961), 11, 566-575.
- [63]. M.J. Corn, F. Stein. Re-entrainment of particles from a surface. *American Industrial Hygiene Association Journal* (1965), 26, 325-336.
- [64]. W. Cheng, R.M. Brach, P.F. Dunn. Surface roughness effects on microparticle adhesion. *Journal of Adhesion* (2002), 78, 929-965.
- [65]. F. Zhang, A.A. Busnaina, M.A. Fury, S.-Q. Wang. The removal of deformed submicron particles from silicon wafers by spin rise and megasonics. *Journal of Electronic Materials* (2000), 29, 199-204.
- [66]. M.W. Reeks, D. Hall. Kinetic models for particle resuspension in turbulent flows: theory and measurement. *Journal of Aerosol Science* (2001), 32, 1-31.
- [67]. M.W. Reeks, J. Reed, D. Hall. On the resuspension of small particles by turbulent flow. *Journal of Physics, D: Applied Physics* (1988), 21, 574-589.
- [68]. E. Hontañón, A. de los Reyes, J.A. Capitão. The CÆSAR code for aerosol resuspension in turbulent pipe flows. Assessment against the storm experiments. *Journal of Aerosol Science* (2000), 9, 1061-1076.
- [69]. E. Hontañón, A. de los Reyes, J.A. Capitão. The CÆSAR code for aerosol resuspension in turbulent pipe flows. Assessment against the storm experiments. *Journal of Aerosol Science* (2000), 9, 1061-1076.
- [70]. I. Adhiwidjaja, S. Matsusaka, H. Tanaka, H. Masuda. Simultaneous phenomenon of particle deposition and re-entrainment: effect of surface roughness on deposition layer of striped pattern. *Aerosol Science and Technology* (2000), 33, 323-333.

- [71]. G. Ziskind, M. Fichman, C. Gutfinger. Adhesion moment model for estimating particle detachment from a surface. *Journal of Aerosol Science* (1997), 28 (4), 623-634.
- [72]. S. Beaudoin, R. Jaiswal, C. Kilroy. Discussion on Hamaker constant. <http://pharmahub.org/resources/206>, 2008.
- [73]. P. Cherukat, J.B. McLaughlin. The inertial lift on a rigid sphere in a linear shear flow field near a flat wall. *Journal of Fluid Mechanics* (1994), 263, 1-18.
- [74]. M.S. Abd-Elhady, C.C.M. Rindt, J.G. Wijers, A.A. van Steenhoven, E.A. Bramer, Th.H. van der Meer. Minimum gas speed in heat exchangers to avoid particulate fouling. *International Journal of Heat and Mass Transfer* (2004), 47, 3943-3955.
- [75]. B.V. Deryagin, V.M. Muller, Yu.P. Toporov. Effect of contact deformation on the adhesion of particles. *Journal of Colloid Interface* (1975), 53, 314-326.
- [76]. W. John, D. N. Fritter, W. Winklmayr. Resuspension induced by impacting particles. *Journal of Aerosol Science* (1991), 22, 723-736.
- [77]. W. John. Particle surface interaction: charge transfer, energy loss, resuspension, and deagglomeration. *Aerosol Science and Technology* (1995), 23, 2-24.
- [78]. W. John, W. Sethi. Threshold of resuspension by particle impaction. *Aerosol Science and Technology* (1993), 19, 69-79.
- [79]. M.S. Abd-Elhady, C.C.M. Rindt, J.G. Wijers, A.A. van Steenhoven. Modelling the impaction of a micron particle with a powdery layer. *Powder Technology* (2006), 168, 111-124.
- [80]. M.S. Abd-Elhady, C.C.M. Rindt, J.G. Wijers, A.A. van Steenhoven. Particulate fouling growth rate as influenced by the change in the fouling layer structure. 2005 ECI Conference on Heat Exchanger Fouling and Cleaning: Challenges and Opportunities. ECI Symposium Series, RP2, Article 19. Berkeley Electronic Press, 2008.
- [81]. M.S. Abd-Elhady, C.C.M. Rindt. Removal of particles from a powdery fouled surface due to impaction. 2003 ECI Conference on Heat Exchanger Fouling and Cleaning: Fundamentals and Application. Paper 18, Berkeley Electronic Press, 2008.
- [82]. B.T. Werner. A physical model of wind-blown sand transport. Ph.D. Thesis, California Institute of Technology, 1987.
- [83]. Sphere packing. From <http://mathworld.wolfram.com/SpherePacking.html>.
- [84]. C.T. Hales. The sphere packing problem. *Journal of Computational and Applied Mathematics* (1992), 44, 41-76.
- [85]. H. Zhou, P.A. Jensen, F.J. Frandsen. Donnan mechanistic model of superheater deposit growth and shedding in a biomass fired grate boiler. *Fuel* (2007), 86, 1519-1533.
- [86]. A. Zbogor, P.A. Jensen, F.J. Frandsen, J. Hansen, P. Glarborg. Experimental investigation of ash deposit shedding in a straw-fired boiler. *Energy and Fuels* (2006), 20, 512-519.
- [87]. H. Biricik, F. Aköz, I. Berktaş, A.N. Tuglar. Study of pozzolanic properties of wheat straw ash. *Cement and Concrete* (1999), 29, 637-643.

- [88]. D. Borello, G. Delibra, K. Hanjalić and F. Rispoli. LES and hybrid LES/RANS study of flow and heat transfer around a wall-bounded short cylinder. ITI Conference, 15-16 October 2008, Bertinoro, Italy.
- [89]. P. Venturini, D. Borello, K. Hanjalić and F. Rispoli. A study of wall-deposit formation using LES-generated velocity field. Turbulence Heat and Mass Transfer 6, K. Hanjalić, Y. Nagano, S. Jakirlić. Begell House, Inc., 2009. 14th-18th September 2009, Rome, Italy.
- [90]. P. Venturini, D. Borello, F. Rispoli, K. Hanjalić. LES-Based prediction of deposit on a wall-bounded short cylinder. International Symposium on Convective Heat and Mass Transfer in Sustainable Energy (CONV-09). April 26th- May 01st, 2009, Hammamet, Tunisia.

Summary

The ultimate aim of this project was to investigate and develop a computational model which can be used in conjunction with a CFD code for URANS (and eventually coarse-grid LES or hybrid RANS-LES methods) to predict the formation of deposit of solid particles on oblique wall surfaces as encountered in biomass-fired boilers and auxiliary equipment. Specifically, the target is to predict the dynamics of deposit formation (the growth rate and the shape of the deposit) on the furnace interior walls, but also (and even more importantly) on tubes and bounding walls of superheaters, heat exchangers and other equipment in which the boiler flue gases are used or processed. This application, involving relatively large particles (over 10 microns) immediately imposes some specific constraints, but also eliminates the need to consider phenomena that are specifically related to smaller (submicron and nano-particles). Notwithstanding these specific effects, a practically useful model should still account for a variety of phenomena and issues.

First of all, a model is needed for computing the transport of particles entrained by a flow and their dispersion due to turbulence. This in itself is still an open research problem, especially if complex interactions between particles (collision, agglomeration, coagulation, burning and or other chemical reactions, etc) are involved. The problem of particle tracking in the flow is, however, *not* the research focus of this thesis, though several existing approaches have been considered as to select the most suitable method for the application in question, which is featured by a very large number of relatively large particles. Among the several approaches available in the literature (four methods are briefly discussed in the Introduction (Chapter 1), two approaches have been considered in parallel: the conventional single particle tracking (SPT) by solving the standard BBO equation, which has been applied to families of equal-size particles in a prescribed distribution, then a particle cloud tracking (PCT) in which clouds of particles with an assumed (usually Gaussian) particle distribution within the cloud is being tracked. In the latter, the same BBO equation is solved, but for the cloud centres. The SPT method is of course, more exact and easily applicable to and associate with models of particle deposition on solid surfaces, but it is limited by computer resources to a relatively small number of particles, i.e. diluted two-phase flows. In contrast, the PCT approach allows a very large number of particles to be considered, and is thus suitable for (U)RANS com-

putation of complex industrial flows. However, the PCT with its inherent averaging and prescribed particle distribution within the clouds brings in considerable approximation to the physics. Moreover, it requires an inverse process of extracting individual (or a family of) particles and their properties (velocity, temperature) once the cloud hits a solid surface. To this purpose, a modification of the PCT was proposed in order to take into account the local particle velocity. Of course, the PCT method can approach the SPT by reducing the assumed size of the clouds, but then the method loses its primary advantage in dealing with large number of particles in a rational and computationally affordable way. Both approaches are discussed and tested in combination with different impact and deposition models.

In order to get an impression of the problem complexity and to design a computer code that could handle complex industrial flows with large number of solid particles depositing on wall, a preliminary study was first conducted by applying a PCT approach in conjunction with a deposition model which accounts for the particle temperature: impacting particles stick on the wall if they have the proper temperature. For that purpose, an industrial biomass combustor was selected, for which earlier computations of flow and combustion have been conducted in the group. In order to handle particle impact, the (in-house) CFD code had to be amended by creating and implementing a separate subroutine with an algorithm for particle tracking within the computational mesh, as well as their impacts on solid walls. This algorithm is described in Chapter 2 and its application to the computations of a biomass combustor in Chapter 3. The results obtained look feasible, but because of the lack of any experimental data regarding the deposition, no validation of the method was possible.

The attention has then been turned to the main focus of the thesis, that is the modelling of the mechanisms and dynamics of particles deposition on a solid wall. This process involves a number of phenomena, from particle impact on the wall, its sticking or rebounding, and particle re-suspension from the deposit layer back into the fluid flow. The process involves the particle-wall sticking properties, adhesion mechanism, effects of impact angle, temperature, the conditions of the wall (especially whether the wall is clean – first series of impacts) or a layer of deposit already has been formed. The particle material properties are, of course, also influential, and so is the particle shape, but the present work is confined only to one or two materials and to only spherical particles. Because different models are available in the literature for the same phenomenon, a priority analysis and direct comparison of some models have been performed and conclusions drawn in regard to the selection of the final models to be implemented in the CFD code. These studies are elaborated in the subsequent three chapters (4. Particle impact and adhesion, 5. Re-suspension and 6. Deposit growth).

To better understand the mechanics of impact, in the chapters dealing with various impact/adhesion models and their validation, the SPT approach was indiscriminately used to compute particle movements, assuming that the results and the selected models can later be used in combination with the PCT or other particle dispersion modelling approaches. Here different impact/adhesion models were analysed and compared. Effect of impact angle, particle temperature and re-suspension on the deposition were also analysed and then implemented into the code.

The code was then applied to two other cases in which various combinations of particle tracking and deposition models have been considered. A graphic summary of cases considered and model combinations are outlined in Chapter 7.

Chapter 8 reports on the validation of the deposition models considered, which was performed by computational mimicking of an experimental and numerical study of particle deposition in a flow over a single long circular cylinder, reported by Zhou et al (2007). The flow was solved using a URANS model. The results obtained with several impact/adhesion models come to close agreement with the visual observation of the deposition shape and thickness after a period of time, as well as with simulations (obtained with a different approach). These validations demonstrated that the code with the models implemented can predict deposit shapes very much alike to the real situation, but some factors not accounted for in the present simulations (i.e., particle shape, particle size distribution, deposition rate) are most probably needed in order to reach the desired prediction.

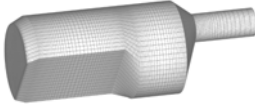
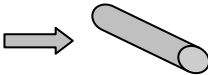
Another, independent set of computations and tests, reported in Chapter 9, were then conducted by considering a relatively simple, but still industrially relevant case: flow and deposit formation on a short cylinder and the two parallel wall bounding it, as encountered in fin-and tube heat exchangers. While no evidence of deposit properties is available, this case was selected because detailed LES study of flow (without particles) has been performed earlier in the same group, thus making it possible to use the LES realisation as an input for the velocity field and thus facilitating to focus on the study of effects of different impact/adhesion and re-suspension models. A series of results obtained with different model combinations are presented and discussed. Although no direct validation with experiments was possible because of the lack of any experimental or other information, a comparison of results obtained with different models made it possible to draw valuable conclusions on different models and their applicability to predict deposit dynamics in real flows. Major conclusions are provided in Chapter 10.

A summary of the cases and models considered in different combinations is given in Table below.

The main outcome and achievements of the thesis can be summarised as follows:

- Extensive and systematic literature survey and *critical and comparative analysis* of various approaches in modelling particle dispersion and deposition (deposit formation) on solid oblique surfaces, with a specific focus on dilute two-phase gas-solid flow with large particles as encountered in industrial combustion applications;
- Selection, testing and modifying various segments (sub-models) of the comprehensive model and their implementation into an in-house CFD code, which has been used to compute several cases of flows with particle deposition;
- Original *algorithm* for particle tracking in conjunction with a specific CFD code
- Illustrative and educationally very useful *computations of three practically relevant flow cases*;
- *Identifying the weak points and critical issues* in modelling the particle deposition and useful suggestions for improving models;
- *Conclusions and recommendations on the future direction of research* on particle deposition and on industrial application of the models.

Summary of the cases and models considered

| <i>Flow configuration</i> | <i>Fluid velocity</i> | <i>Particle dispersion</i> | <i>Deposition model</i> |
|--|-----------------------|--|--|
| <p>Industrial application: <i>Biomass combustor</i></p>  | RANS (k-ε) | PCT (standard) | Temperature controlled |
| <p>Model Validation case: <i>Long cylinder in a cross flow</i></p>  | RANS (ζ-f) | SPT | <ul style="list-style-type: none"> - Temperature controlled - Thornton & Ning - impact angle <p>Deposit Growth: Engineering approach</p> |
| <p>Application 1: <i>Short wall-bounded cylinder</i></p>  | LES | <p>PCT (modified)</p> <p>SPT</p> | <ul style="list-style-type: none"> - RM (Zhang) - RM (Zhang) - Van Beek - Thornton & Ning - Feng - Impact angle - Re-suspension |

Sommario

L'obiettivo finale del progetto è quello di studiare e sviluppare un modello computazionale da utilizzare in combinazione con un codice CFD per URANS (ed eventualmente LES su griglie non raffinate o metodi ibridi RANS-LES), per prevedere la formazione di depositi all'interno di caldaie alimentate a biomassa e dispositivi ausiliari. In particolare, l'obiettivo è quello di prevedere le dinamiche di formazione di depositi (il tasso di crescita e la forma del deposito) sulle pareti interne del forno, ma anche (cosa ancor più importante) su tubi e pareti di surriscaldatori, scambiatori di calore, e di altre apparecchiature in cui il gas di combustione delle caldaie vengono utilizzati o trasformati. Questa applicazione, coinvolgendo particelle di dimensioni relativamente grandi (in genere oltre 10 micron) impone immediatamente alcune limitazioni specifiche, ma al contempo elimina la necessità di dovere considerare fenomeni specificamente legati a particelle più piccole (submicron e nanoparticelle).

Tuttavia, un modello che risulti utile dal punto di vista pratico dovrebbe tener conto di una varietà di fenomeni e problematiche. Prima di tutto, è necessario modellare il trasporto (particle tracking) e la dispersione turbolenta delle particelle presenti nel flusso di gas. Questo è uno dei problemi ancora aperti della ricerca, soprattutto nel caso in cui siano coinvolte complesse interazioni tra le particelle (collisioni, agglomerazioni, combustione e/o altre reazioni chimiche, ecc.). Il problema del particle tracking, tuttavia, non è il punto centrale di questo lavoro di ricerca, anche se diversi approcci sono stati considerati per selezionare il metodo più adatto per l'applicazione in questione, caratterizzata da un numero molto elevato di particelle (relativamente) grandi. Tra i vari approcci disponibili in letteratura (quattro sono quelli brevemente descritti nell'introduzione, Capitolo 1), due sono stati utilizzati in parallelo: quello in cui viene risolta l'equazione standard BBO del moto di ogni singola particella simulata (SPT), applicato a famiglie di particelle tutte uguali con una data distribuzione spaziale, e quello a nuvola di particelle (PCT) all'interno della quale si assume che le particelle seguano una distribuzione Gaussiana. In questo caso, l'equazione BBO viene risolta non per le singole particelle ma per il centro della nuvola. Il metodo SPT è, naturalmente, più preciso e facilmente applicabile e associabile ai modelli di impatto/adesione delle particelle sulle pareti solide, ma a causa di limiti computazionali è indicato solo in applicazioni con un numero relativamente piccolo di particelle, cioè a flussi bifase molto diluiti. Al contra-

rio, l'approccio PCT consente di considerare un numero molto elevato di particelle, ed è quindi adatto a simulazioni (U)RANS di flussi industriali complessi. Tuttavia, l'approccio PCT risolvendo in via mediata l'equazione BBO e assumendo una data distribuzione di particelle all'interno di ogni nuvola, approssima notevolmente la fisica del fenomeno, perdendo inoltre le informazioni relative alle singole particelle. Una volta che una nuvola colpisce una superficie è necessario dunque un processo di estrazione delle proprietà (velocità, temperatura) delle singole (o di una famiglia di) particelle. A questo scopo, si è proposta una versione modificata del modello PCT che tenga conto della velocità locale delle particelle. Naturalmente il metodo PCT può avvicinarsi a quello STP riducendo la dimensione delle nuvole e aumentandone il numero; così facendo però il modello perde il suo principale vantaggio di poter trattare un elevato numero di particelle. Entrambi gli approcci sono discussi e analizzati in combinazione con diversi modelli di impatto e deposizione.

Al fine di farsi un'idea della complessità del problema e per la progettazione di un codice informatico in grado di gestire flussi industriali complessi e con un numero elevato di particelle solide che si depositano, è stato effettuato uno studio preliminare in cui l'approccio PCT è stato combinato con un modello di formazione del deposito dipendente dalla temperatura delle particelle: le particelle incidenti si attaccano alle pareti se hanno la temperatura adatta. Si è scelto dunque di simulare la formazione di deposito all'interno di un bruciatore industriale alimentato a biomassa, per il quale nello stesso gruppo di ricerca erano già state effettuate simulazioni CFD, comprendenti la combustione. Al fine di gestire l'impatto delle particelle, il codice CFD (in-house) è stato modificato creando e implementando una subroutine separata contenente un algoritmo per il tracciamento delle traiettorie delle varie particelle all'interno della mesh di calcolo, e la meccanica dell'impatto sulle pareti. Questo algoritmo è descritto nel capitolo 2, mentre i risultati delle simulazioni del bruciatore a biomasse sono riportati Capitolo 3. I risultati ottenuti sembrano verosimili, ma a causa della mancanza di dati sperimentali al riguardo, non è stato possibile validare il metodo utilizzato.

Successivamente l'attenzione è stata concentrata sull'obiettivo principale della tesi, cioè sulla modellazione dei meccanismi e delle dinamiche dell'accumulo di particelle su una parete solida. Questo processo comprende una serie di fenomeni, dall'urto delle particelle sulla parete, l'adesione o rimbalzo delle stesse, fino alla risospensione delle particelle già depositate per azione delle fluttuazioni del flusso. Il processo coinvolge le proprietà di adesione delle varie particelle, i meccanismi di adesione, gli effetti dell'angolo d'impatto, la temperatura, le condizioni della parete su cui impattano le particelle (in particolare se la parete è pulita - prima serie di impatti) o dello strato di deposito eventualmente già formato. Anche le caratteristiche materiali delle particelle sono naturalmente importanti, così come la loro forma, ma il presente lavoro è limitato a uno o due materiali e a particelle sferiche.

Poiché per lo stesso fenomeno in letteratura sono disponibili diversi modelli, sono stati effettuati un'analisi preliminare e un confronto diretto di alcuni di essi, potendo così selezionare quelli da implementare nel codice CFD. Queste analisi sono presentate nei tre capitoli successivi (4. Particle impact and adhesion, 5. Re-suspension e 6. Deposit growth).

Per comprendere meglio i meccanismi di impatto, nei capitoli ad essi relativi e in quelli di validazione, è stato utilizzato l'approccio SPT per calcolare i movimenti delle

particelle, supponendo che i risultati e i modelli selezionati possono poi essere utilizzati in combinazione anche con il PCT o con altri approcci per la dispersione turbolenta delle particelle. Diversi modelli di impatto/adesione sono stati analizzati e confrontati. L'effetto dell'angolo d'impatto, della temperatura delle particelle, e la risospensione sono stati analizzati e poi implementati nel codice.

Sono state poi condotte una serie di simulazioni su altri due casi, utilizzando diverse combinazioni di modelli per il particle tracking e per la deposizione. Una sintesi grafica dei casi considerati e delle varie combinazioni di modelli utilizzate sono descritte nel capitolo 7.

Il capitolo 8 riporta la validazione dei modelli di formazione del deposito considerati, utilizzando come riferimento lo studio (sperimentale e numerico) di Zhou et al (2007), riguardante la formazione di deposito su un tubo cilindrico disposto all'interno di un combustore per paglia. Il flusso è stato risolto utilizzando un modello (U)RANS. I risultati ottenuti con i vari modelli di impatto/adesione utilizzati, sono in accordo sia con quanto si può osservare visivamente nell'articolo di riferimento, sia con i risultati numerici riportati nello stesso studio (ottenuti con un diverso approccio). Questo dimostra che il codice con i modelli implementati, è in grado di prevedere forme di deposito molto simili al caso reale; tuttavia alcuni fattori non considerati nelle simulazioni presenti (per esempio la forma delle particelle, la loro distribuzione dimensionale, il tasso di deposito) sono probabilmente necessari per migliorare ulteriormente la capacità di previsione.

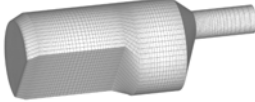
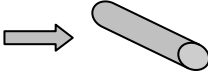
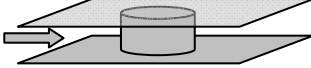
È stato inoltre condotto un altro set indipendente di calcoli e test, riportato nel capitolo 9, considerando un caso relativamente semplice, ma comunque di interesse industriale: sono stati simulati il flusso e la formazione di depositi su un cilindro corto compreso tra due pareti, geometria che si riscontra in alcuni tipi di scambiatori di calore. Pur non essendo disponibile alcuna prova sulle caratteristiche del deposito in casi simili, questo caso è stato scelto perché uno studio LES dettagliato del flusso (senza particelle) era stato effettuato in precedenza nello stesso gruppo di ricerca, rendendo così possibile utilizzare le realizzazioni LES come input per il codice di previsione del deposito. In questo modo è stato possibile concentrarsi sullo studio degli effetti dei vari modelli di impatto/adesione e risospensione. Nel capitolo vengono presentati e discussi una serie di risultati ottenuti con combinazioni di diversi modelli. Anche se non è stato possibile validare i risultati delle simulazioni con prove sperimentali, un confronto dei risultati ottenuti con diversi modelli permette di trarre conclusioni valide su diversi modelli e sulla loro applicabilità alla previsione dei depositi in flussi reali.

I principali risultati ottenuti e gli obiettivi raggiunti con questa tesi possono essere riassunti nei seguenti punti:

- Indagine estesa e sistematica della letteratura e *analisi critica e comparata* di vari approcci possibili per la modellazione della dispersione delle particelle e formazione dei depositi su superficie solide oblique, con attenzione specifica ai flussi bifase (gas-solido) diluiti di particelle relativamente grandi che si incontrano nelle allocazioni industriali di combustione;
- Selezione, test e modifica di vari segmenti (fotomodelli) del modello complessivo, e loro implementazione in un codice CFD (in-house), utilizzato per simulare diversi casi di flussi con deposito di particelle;

- Algoritmo originale per il particle tracking da utilizzare in connessione con un codice CFD specifico;
- *Simulazione di tre diversi flussi di importanza pratica* utili sia dal punto di vista illustrativo del fenomeno, che educativo;
- *Individuazione dei punti deboli e questioni critiche* nella modellazione del processo di deposito delle particelle e suggerimenti utili per il miglioramento dei modelli;
- *Conclusioni e raccomandazioni sugli indirizzi futuri della ricerca* riguardante il deposito delle particelle e l'applicazione industriale dei modelli.

Riassunto dei casi e modelli considerati

| <i>Flow configuration</i> | <i>Fluid velocity</i> | <i>Particle dispersion</i> | <i>Deposition model</i> |
|---|-----------------------|------------------------------|---|
| Industrial application: <i>Biomass combustor</i>  | RANS (k-ε) | PCT (standard) | Temperature controlled |
| Model Validation case: <i>Long cylinder in a cross flow</i>  | RANS (ζ-f) | SPT | - Temperature controlled - Thornton & Ning - impact angle Deposit Growth: Engineering approach |
| Application 1: <i>Short wall-bounded cylinder</i>  | LES | PCT (modified) SPT | - RM (Zhang) - RM (Zhang) - Van Beek - Thornton & Ning - Feng - Impact angle - Re-suspension |

Aknowledgements

First of all I would like to express my thanks and gratitude to Prof. Kemal Hanjalić and Prof. Franco Rispoli for giving me the opportunities to work with them, as well as for their continuous inspiration, invaluable supervision and guidance during my PhD study. Then I wish to thank also Dr. Domenico Borello for continuous interaction, indispensable assistance and consulting both on scientific and personal matters, which have partly been facilitated by our same cultural background. My thanks are also due to Dr. Alessandro Corsini for his interest in my work, his advice and assistance, for his wireless connection, and for his inspiring alert on the needs for and the ways of innovation.

And last but not least I wish to convey my thanks to all the people who work, worked or/and study in room 21 of DMA, for their help, companionship, or simply for sharing their days, problems and joy with me.

List of publications

- P. Venturini, D. Borello, C.V. Iossa, D. Lentini, F. Rispoli. *Modelling of multiphase combustion and deposit formation and deposit formation in a biomass-fed boiler* submitted to Energy Int. Journal (under revision).
- P. Venturini, D. Borello, K. Hanjalić and F. Rispoli. *A study of wall-deposit formation using LES-generated velocity field*. Turbulence Heat and Mass Transfer 6, K. Hanjalić, Y. Nagano, S. Jakirlić (eds). Begell House, Inc., 2009. 14th-18th September 2009, Rome, Italy.
- C.V. Iossa, D. Lentini, F. Rispoli, P. Venturini. *Combustion modelling in a biomass-fed furnace*. International Symp. on Convective Heat and Mass Transfer in Sustainable Energy (CONV-09). April 26th-May 01st, 2009, Hammamet, Tunisia.
- P. Venturini, D. Borello, F. Rispoli, K. Hanjalić. *LES-Based prediction of deposit on a wall-bounded short cylinder*. International Symp. on Convective Heat and Mass Transfer in Sustainable Energy (CONV-09). April 26th- May 01st, 2009, Hammamet, Tunisia. (submitted by invitation to the Special Issue of the Int. J. on Computational Thermal Sciences).

About the author

| | |
|-------------------------|---|
| 8 January 1972 | Born in Rome (Italy) |
| 31 May 2004 | M.Sc. degree in Mechanical Engineering at Sapienza Università di Roma (Italy). Thesis: <i>Analysis of fouling and slagging problems within boilers fed with dried vegetation waters.</i> |
| July -December 2004 | Contract with CIRPS (Interuniversity Research Centre for Sustainable Development), Sapienza Università di Roma (Italy). Project PIBE (Integrated Platform Bio-refuses and Energy). |
| October 2005-March 2006 | Contract with CIRPS (Interuniversity Research Centre for Sustainable Development), Sapienza Università di Roma (Italy). Project PIBE (Integrated Platform Bio-refuses and Energy). |
| March- May 2006 | Consulting engineer at Agriconsulting s.p.a. (Roma, Italy). National project: ProBio (Promotion of the use of Biomass). |
| September 2006 | 2 nd level Master in Energy Efficiency and Renewable Energy at Sapienza Università di Roma (Italy). Thesis: <i>Co-combustion of coal and biomass. Technical problems and application to Italian situation.</i> |
| November-December 2007 | Consulting engineer at Agriconsulting s.p.a. (Roma, Italy). National project: ProBio (Promotion of the use of Biomass). |

